Title

Synaptic Cell Adhesion Molecule Latrophilin-2 and its Role in Patterning of Medial Entorhinal Cortex Circuitry

Author

Donohue, Jordan Dale

Publication Date

2022

UNIVERSITY OF CALIFORNIA
RIVERSIDE

Synaptic Cell Adhesion Molecule Latrophilin-2 and its Role in Patterning of Medial Entorhinal Cortex Circuitry

A Dissertation submitted in partial satisfaction
of the requirements for the degree of

Doctor of Philosophy

in

Neuroscience

by

Jordan D. Donohue

December 2022

Dissertation Committee:
Dr. Garret Anderson, Chairperson.
Dr. Vijayalakshmi Santhakumar
Dr. Iryna Ethell

The Dissertation of Jordan D. Donohue is approved:

Committee Chairperson

University of California, Riverside

Acknowledgements

A single chapter of this dissertation is a reprint of materials previously published and publicly available. Chapter 2 of this dissertation is a reprint of materials it appears in Donohue et al., 2021. Chapter 3 of this dissertation is currently in preparation to be submitted.

To all the people who have supported me along this journey, I want to offer my sincere gratitude. I want to thank my parents and grandparents for raising me and teaching me the importance of hard work alongside the importance of doing things right. I want to thank my sister for always being an inspiration. I want to thank my previous research advisor Dr. Murphy for giving me the opportunity to first work in a lab and all she has done for me across the years. To all the friends I have made across this journey that have supported me and been there to reconcile the ups and downs of pursing a PhD, thank you. To all the talented researchers and staff at UCR who in one way or the other helped me with my research, thank you. To all the research animals involved in this work, I pay respect to them and say thank you. To my partner Celia who has supported me in all my endeavors, thank you. Lastly, to the person most responsible for my scientific career my advisor Dr. Anderson. You have been the advisor that I need, and I appreciate the way in which you have always focused on improving me as a scientist and not just my experiments. Thank you for helping me make meaningful connections with people in science and supporting me as a human being and not just a worker, I am forever in your gratitude.

ABSTRACT OF THE DISSERTATION

Synaptic Cell Adhesion Molecule Latrophilin-2 and its Role in Patterning of Medial Entorhinal Cortex Circuitry

by

Jordan D. Donohue

Doctor of Philosophy, Graduate Program in Neuroscience
University of California, Riverside, December 2022
Dr. Garret Anderson, Chairperson

Across this dissertation we investigate how a synaptic cell adhesion molecule, latrophilin-2 is involved with circuit development in the medial entorhinal cortex, a region implicated in spatial learning. We do a thorough analysis of brain wide protein localization alongside cell-type specific expression analysis to determine which neurons express latrophilin-2 and where that expression is most enriched. We find latrophilin-2 controls spine development for local pyramidal neurons and neurons retrogradely labelled from the ipsilateral pre-subiculum are reduced when latrophilin-2 is deleted, but other inputs remain similar. Following this study, we created a mouse line in which latrophilin-2 expression was removed specifically from the medial entorhinal cortex layer 3 neurons. Using these mice we found distinct differences for localization of input axons, and deficits in acquisition of sequential spatial learning. Together this suggests latrophilin-2 is crucial in assembly of entorhinal circuitry and distinct functions of these cells.

Contents.

List of Figures.

Chapter 1: Introduction

Basics of the brain

The human brain is a highly complex organ which a variety of debilitating diseases can affect. Across development roughly 100 billion cells known as neurons make roughly 100 trillion specific connections. The specificity of these connections comprises proper brain function, and it may seem surprising that the brain is able to complete this task at all. From neurodevelopmental diseases such as autism spectrum disorder, to neurodegenerative diseases such as Alzheimer's disease, to affective disorders such as depression which ail people throughout their life; the brain can function incorrectly in a myriad of ways. Neurons which make up the brain are organized into functional regions where groups of cells work to do a similar function and make connections with other neurons to further process this information. These connections known as synapses occur where a pre-synaptic neuron connects through an axon with a post-synaptic target neuron. These connections can occur between neighboring cells or between distant brain regions. The order in which these neurons connect is crucial and is the basis of functional "circuits" in the brain that process specific types of information such as vision or smell. We know many of the specific functions for distinct brain regions from early studies looking at humans with brain damage confined to a specific area and comparing the effects on cognition. With modern advances in science, we have correlated enough information across mammals that we generally study mice, rats, apes, or even single cells grown in-vitro to gain insight into how the human brain works and how these neurons function.

For example, vision in the central nervous system is processed in a sequential fashion. First, the retina receives light and converts that information into either red, green,

or blue with different color detecting cone cells and simultaneously measures intensity of light with non-color discriminate rod cells. This information is passed through distinct pathways to the visual cortex where information is processed in a linear sense from simple to complex (Kravitz, Saleem, Baker, & Mishkin, 2011; Steffenach, Witter, Moser, & Moser, 2005; Wang, Gao, & Burkhalter, 2011). As this information is passed through the cortex in this fashion, it is processed by brain regions known essential for visual processing and spatial navigation (Fukawa, Aizawa, Yamakawa, & Yairi, 2020). This information eventually is sent to a region known as the entorhinal cortex, which combines information from the multiple senses (Save & Sargolini, 2017; Wang et al., 2011). From there neurons project to the hippocampus, the memory center of the brain. Together, this illustrates the point that the brain processes information in a sequential manner and specific brain regions are involved with different aspects of cognition. Although we understand many aspects involved with visual perception, there are many factors we are just starting to discover.

How these concepts relate to my work

How is this synaptic specificity achieved by the brain, and why is it useful to study this topic? The first question is still highly debated, but we do have a basic understanding of the factors involved. Neural development starts out in with a small handful of cells that divide and differentiate into many different types of cells that eventually constitute the fully formed brain (Hu, Chahrour, & Walsh, 2014). These neurons divide from pre-existing cells in a temporally distinct fashion due to transcription of specific genes that determine their cell identify (Telley et al., 2016). The neurons migrate to their destination and then must make functional connections with the right cells (Yang & Shcheglovitov, 2020). These

neurons project their axons to local and distant cells using various cues to ensure these projections arrive in the correct area and make connections with specific cells to form synapses through cell-cell recognition processes.

In the hippocampal circuit, this process occurs in a linear fashion where development of pre-synaptic neurons precedes post-synaptic neurons in that circuit. When pre-synaptic neurons are rendered unfunctional, then post-synaptic neurons do not develop properly (Donato, Jacobsen, Moser, & Moser, 2017). This indicates that within a given circuit, functional connectivity occurs in a linear fashion and is dependent on proper function of pre-synaptic neurons. There are a variety of proteins presented in either pre- or post-synaptic compartments that are crucial for the formation of functional neural circuits (Burbach & Meijer, 2019; Südhof, 2018). Several proteins implicated in this synaptic specificity are known to be mutated in people with neurodevelopmental diseases (Burbach & Meijer, 2019; Oguro-Ando, Zuko, Kleijer, & Burbach, 2017; Regan et al., 2019; Regan, Williams, Sugimoto, Vorhees, & Dawson, 2022). Many neurological diseases stem from specific regions in the brain misfunctioning and the fact we do not have a complete understanding of how these brain regions connect makes studying how this occurs crucial for the advancement of neuroscience research. Without a complete understanding regarding brain connectivity, we are barely scratching the surface of how this connection specificity is achieved.

History of Latrophilins

Latrophilins were discovered and named due to the fact they bind α-Latrotoxin, a toxin secreted in black widow spider venom. Black widow bites cause a condition known as latrodectism, a syndrome characterized by symptoms including generalized pain,

cramps, perfuse sweating and tachycardia (Zukowski, 1993). α-Latrotoxin was studied for many years in neuroscience because when applied to neurons, it stimulates vesicular exocytosis by inserting itself into the pre-synaptic plasma membrane (Südhof, 2001). One thing that particularly intrigued scientists during early studies on α-Latrotoxin is that there were several types of molecules which bound to α-Latrotoxin and they had different effects on the synapse. One prominent class of molecules were shown to bind α-Latrotoxin and stimulate exocytosis in a calcium dependent manner, which were later named Neurexins (Petrenko et al., 1990; Ushkaryov, Petrenko, Geppert, & Südhof, 1992). Another class of molecules were shown to stimulate exocytosis in a calcium independent manner (Davletov, Shamotienko, Lelianova, Grishin, & Ushkaryov, 1996; Krasnoperov et al., 1996, 1997; Südhof, 2001), which we now know as Latrophilins (Lphn1, Lphn2 & Lphn3, [gene symbol ADGRL]).

The idea that endogenous latrophilin binding may stimulate neuronal communication without calcium was quite intriguing to scientists, but the technology did not yet exist to easily test these hypotheses. Although it was known α-Latrotoxin binds to latrophilin protein, it was not known which other endogenous proteins in the human body bind with latrophilins or if endogenous function of latrophilins resemble what is observed in α-Latrotoxin binding. Nearly 20 years later, the topic became revisited due to technology advances. A mouse model was created which lacked the latrophilin-2 gene. Using this mouse it was found that they are not viable and therefore established latrophilin-2 is crucial for development (Anderson et al., 2017). Following these experiments, scientists created a conditional gene knockout model where latrophilin-2 expression was specifically removed from neurons in the brain. This model allows us to study the function of this protein in the brain by observing differences between mice which have a functional copy

of latrophilin-2 and mice which do not in neurons specifically. It was found that these mice were viable but had some distinct differences from their wild-type control mice (Anderson et al., 2017). It was also shown that hippocampal principal neurons had distinct synaptic loss in their distal dendrites arising from entorhinal inputs, but other synapses were intact. Additionally, spatial learning was altered in these mice for tasks known to be dependent on entorhinal inputs, but other hippocampal learning assays were not altered. These findings spurred a renewed interest in the function of latrophilins. To follow this work, scientists wanted to better understand how latrophilins functioned at the synapse to achieve connection specificity. Although it had been established for some time that latrophilins have g-protein coupled receptor (GPCR) function, and does it relate to their synaptic function? To answer these questions scientists needed to understand what the molecular binding partners of latrophilin are and if binding between these molecules might alter function of latrophilins in a manner reminiscent of early α-Latrotoxin binding studies.

Synaptic Cell Adhesion Molecules

We now know that latrophilins bind with other synaptic cell-adhesion molecules (sCAMs). This class of molecules are known to form complexes between pre- and post-synaptic neurons and modulate the strength of their connectivity (Burbach & Meijer, 2019; Südhof, 2018). Although many of these molecules have been studied for decades, in the past several years there have been many large breakthroughs regarding the function of sCAMs in synaptic development. Recently the crystal structure of latrophilins were resolved and it was shown latrophilins form stable trans-synaptic interactions with both teneurins and fibronectin leucine rich repeat transmembrane proteins (FLRTs) simultaneously (del Toro et al., 2020). When latrophilin is bound by teneurin and FLRT,

excitatory synapse development occurs, but when FLRT binding is abolished, inhibitory synapse development proceeds (Li et al., 2020). Furthermore, latrophilin mediated synapse development is dependent on its GPCR signaling (Sando & Südhof, 2021).

To determine how these molecules work, scientists do a variety of experiments on different scales to better understand their function. For example, in humans we can do genetic screenings of large numbers of people and see how people with specific mutations in these genes are more or less likely to develop specific diseases. We then use this information to make genetic models in related animals that possess the same or extremely similar genes. In this way, we can modify the expression of specific genes implicated in disease and determine their function. For example, latrophilin-3 was discovered to be mutated in humans who have ADHD (Arcos-Burgos et al., 2010). This protein was also shown to control synapse development (O'Sullivan, Martini, von Daake, Comoletti, & Ghosh, 2014) providing insight into how dysfunction of a specific protein may result in disease. Scientists then genetically removed Lphn3 from rats which exhibit ADHD like traits (Regan et al., 2019), allowing us to study how this gene may be involved in the symptoms patients exhibit from this disease. Information obtained by these studies can also be used to investigate how different types of medication may be more efficacious or not work as well for people with known genetic differences. For Lphn3 mutations in humans, that information can be used to help treat ADHD pathology by predicting which medications will work (Arcos-Burgos et al., 2010; Sorokina et al., 2018).

Moving Forward

Although latrophilin function is not well understood, we do know their synaptogenic properties rely on intracellular GPCR signaling which may be mediated by extracellular

binding of trans-synaptic partners as previously discussed. Since it is known complete removal of latrophilin-2 in mice is embryonically lethal (Anderson et al., 2017), we had to design experiments carefully to investigate it's function in the brain. When I joined the lab, I first wanted to identify a brain area to focus on for my initial studies. We had to identify where in the brain Lphn2 was enriched, and if it had a role in synaptic development for this brain region as well. We identified the medial entorhinal cortex as a hotspot of expression in pyramidal neurons, and that there is a spatial gradient of Lphn2 expression for these neurons. We identified that Lphn2 is important in synaptic spine development of these neurons and that Lphn2 expression gradients coincide with connectivity gradients of synaptic inputs. To conclude the first study, we combined genetic deletion of Lphn2 with retrograde connectivity analysis and found that pre-subiculum inputs were affected by Lphn2 deletion, but other inputs were not. To expand upon this work, we made a new mouse model that specifically removed Lphn2 expression from medial entorhinal cortex layer 3 pyramidal neurons previously identified as high Lphn2 expression neurons. We then used this mouse to measure specificity of axonal targeting for these mice and find that there is a similar gradient of axonal targeting overlapping Lphn2 expression gradients. We find that removal of Lphn2 expression in MEC neurons causes mistargeting of input axons in Lphn2 enriched distal MEC for layer 1 and 3 of cortex. We also find that post-synaptic spines in these neurons are lost for layer 3 pyramidal neurons in both layers 1 and 3. Lastly, we find that Lphn2 deletion in MEC layer 3 neurons causes deficiencies in learning of spatial sequential tasks associated with normal MEC layer 3 pyramidal neuron function in mice. Together the goal of this work is to better understand how latrophilin-2 is involved in neural circuit assembly, and how those synaptic deficiencies in circuit formation contribute to deficiencies observed in behavior.

Chapter 1 References

Anderson, G. R., Maxeiner, S., Sando, R., Tsetsenis, T., Malenka, R. C., & Südhof, T. C. (2017). Postsynaptic adhesion GPCR latrophilin-2 mediates target recognition in entorhinal-hippocampal synapse assembly. *Journal of Cell Biology*, *216*(11), 3831–3846. https://doi.org/10.1083/jcb.201703042

Arcos-Burgos, M., Jain, M., Acosta, M. T., Shively, S., Stanescu, H., Wallis, D., … Muenke, M. (2010). A common variant of the latrophilin 3 gene, LPHN3, confers susceptibility to ADHD and predicts effectiveness of stimulant medication. *Molecular Psychiatry*, *15*(11), 1053–1066. https://doi.org/10.1038/mp.2010.6

Burbach, P. P. H., & Meijer, D. H. (2019). Latrophilin's social protein network. *Frontiers in Neuroscience*, *13*(JUN), 1–13. https://doi.org/10.3389/fnins.2019.00643

Davletov, B. A., Shamotienko, O. G., Lelianova, V. G., Grishin, E. V., & Ushkaryov, Y. A. (1996). Isolation and biochemical characterization of a Ca2+-independent α-latrotoxin-binding protein. *Journal of Biological Chemistry*, *271*(38), 23239–23245. https://doi.org/10.1074/jbc.271.38.23239

del Toro, D., Carrasquero-Ordaz, M. A., Chu, A., Ruff, T., Shahin, M., Jackson, V. A., … Seiradake, E. (2020). Structural Basis of Teneurin-Latrophilin Interaction in Repulsive Guidance of Migrating Neurons. *Cell*, *180*(2), 323-339.e19. https://doi.org/10.1016/j.cell.2019.12.014

Donato, F., Jacobsen, R. I., Moser, M. B., & Moser, E. I. (2017). Stellate cells drive maturation of the entorhinal-hippocampal circuit. *Science*, *355*(6330). https://doi.org/10.1126/science.aai8178

Fukawa, A., Aizawa, T., Yamakawa, H., & Yairi, I. E. (2020). Identifying core regions for path integration on medial entorhinal cortex of hippocampal formation. *Brain Sciences*, *10*(1). https://doi.org/10.3390/brainsci10010028

Hu, W. F., Chahrour, M. H., & Walsh, C. A. (2014). The diverse genetic landscape of neurodevelopmental disorders. *Annual Review of Genomics and Human Genetics*, *15*, 195–213. https://doi.org/10.1146/annurev-genom-090413-025600

Krasnoperov, V. G., Beavis, R., Chepurny, O. G., Little, A. R., Plotnikov, A. N., & Petrenko, A. G. (1996). The calcium-independent receptor of α-latrotoxin is not a neurexin. *Biochemical and Biophysical Research Communications*, *227*(3), 868–875. https://doi.org/10.1006/bbrc.1996.1598

Krasnoperov, V. G., Bittner, M. A., Beavis, R., Kuang, Y., Salnikow, K. V., Chepurny, O. G., … Petrenko, A. G. (1997). α-Latrotoxin stimulates exocytosis by the interaction with a neuronal G-protein-coupled receptor. *Neuron*, *18*(6), 925–937. https://doi.org/10.1016/S0896-6273(00)80332-3

Kravitz, D. J., Saleem, K. S., Baker, C. I., & Mishkin, M. (2011). A new neural framework for visuospatial processing. *Nature Reviews Neuroscience*, *12*(4), 217–230. https://doi.org/10.1038/nrn3008

Li, J., Xie, Y., Cornelius, S., Jiang, X., Sando, R., Kordon, S. P., … Araç, D. (2020). Alternative splicing controls teneurin-latrophilin interaction and synapse specificity by a shape-shifting mechanism. *Nature Communications*, *11*(2140). https://doi.org/10.1038/s41467-020-16029-7

O'Sullivan, M. L., Martini, F., von Daake, S., Comoletti, D., & Ghosh, A. (2014). LPHN3, a presynaptic adhesion-GPCR implicated in ADHD, regulates the strength of neocortical layer 2/3 synaptic input to layer 5. *Neural Development*, *9*(1), 1–11. https://doi.org/10.1186/1749-8104-9-7

Oguro-Ando, A., Zuko, A., Kleijer, K. T. E., & Burbach, J. P. H. (2017). A current view on contactin-4, -5, and -6: Implications in neurodevelopmental disorders. *Molecular and Cellular Neuroscience*, *81*, 72–83. https://doi.org/10.1016/j.mcn.2016.12.004

Petrenko, A. G., Kovalenko, V. A., Shamotienko, O. G., Surkova, I. N., Tarasyuk, T. A., Ushkaryov, Y. A., & Grishin, E. V. (1990). Isolation and properties of the a-latrotoxin receptor The receptor protein of a-latrotoxin (caLTx, a neurotoxin. *The EMBO Journal*, *9*(6), 2023–2027.

Regan, S. L., Hufgard, J. R., Pitzer, E. M., Sugimoto, C., Hu, Y. C., Williams, M. T., & Vorhees, C. V. (2019). Knockout of latrophilin-3 in Sprague-Dawley rats causes hyperactivity, hyper-reactivity, under-response to amphetamine, and disrupted dopamine markers. *Neurobiology of Disease*, *130*(June), 104494. https://doi.org/10.1016/j.nbd.2019.104494

Regan, S. L., Williams, M. T., Sugimoto, C., Vorhees, C. V, & Dawson, H. E. (2022). Latrophilin-3 heterozygous versus homozygous mutations in Sprague Dawley rats : Effects on egocentric and allocentric memory and locomotor activity. *Genes, Brain and Behavior*, *21*(May), 1–15. https://doi.org/10.1111/gbb.12817

Sando, R., & Südhof, T. C. (2021). Latrophilin gpcr signaling mediates synapse formation. *ELife*, *10*, 1–22. https://doi.org/10.7554/eLife.65717

Save, E., & Sargolini, F. (2017). Disentangling the role of the MEC and LEC in the processing of spatial and non-spatial information: Contribution of lesion studies. *Frontiers in Systems Neuroscience*, *11*(October), 1–9. https://doi.org/10.3389/fnsys.2017.00081

Sorokina, A. M., Saul, M., Goncalves, T. M., Gogola, J. V., Majdak, P., Rodriguez-Zas, S. L., & Rhodes, J. S. (2018). Striatal transcriptome of a mouse model of ADHD reveals a pattern of synaptic remodeling. *PLoS ONE*, *13*(8), 1–20. https://doi.org/10.1371/journal.pone.0201553

Steffenach, H. A., Witter, M., Moser, M. B., & Moser, E. I. (2005). Spatial memory in the rat requires the dorsolateral band of the entorhinal cortex. *Neuron*, *45*(2), 301–313. https://doi.org/10.1016/j.neuron.2004.12.044

Südhof, T. C. (2001). α -LATROTOXIN AND ITS RECEPTORS: Neurexins and CIRL / Latrophilins. *Annu. Rev. Neurosci.*, *24*(Simmons 1991), 933–962.

Südhof, T. C. (2018). Towards an Understanding of Synapse Formation. *Neuron*, *100*(2), 276–293. https://doi.org/10.1016/j.neuron.2018.09.040

Telley, L., Govindan, S., Prados, J., Stevant, I., Nef, S., Dermitzakis, E., … Jabaudon, D. (2016). Sequential transcriptional waves direct the differentiation of newborn neurons in the mouse neocortex. *Science*, *351*(6280), 1443–1446. https://doi.org/10.1126/science.aad8361

Ushkaryov, Y. A., Petrenko, A. G., Geppert, M., & Südhof, T. C. (1992). Neurexins: Synaptic cell surface proteins related to the α-latrotoxin receptor and laminin. *Science*, *257*(5066), 50–56. https://doi.org/10.1126/science.1621094

Wang, Q., Gao, E., & Burkhalter, A. (2011). Gateways of ventral and dorsal streams in mouse visual cortex. *Journal of Neuroscience*, *31*(5), 1905–1918. https://doi.org/10.1523/JNEUROSCI.3488-10.2011

Yang, G., & Shcheglovitov, A. (2020). Probing disrupted neurodevelopment in autism using human stem cell-derived neurons and organoids: An outlook into future diagnostics and drug development. *Developmental Dynamics*, *249*(1), 6–33. https://doi.org/10.1002/dvdy.100

Zukowski, C. W. (1993). Black widow spider bite. *Journal of American Board Family Practice*, *6*(3), 279–281.

Chapter 2: Parahippocampal expression of adhesion-GPCR Latrophilin-2 (*ADGRL2*) controls topographical presubiculum to entorhinal cortex circuit connectivity

Jordan D. Donohue[1,2], Ryan F. Amidon[1,3], Thomas R. Murphy[1], Anthony J. Wong[1], Elizabeth D. Liu[1], Lisette Saab[1], Alexander King[1,2], Haneal Pae[1,2], Moyinoluwa T. Ajayi[1], Garret R. Anderson[1]*

[1]Department of Molecular, Cell, and Systems Biology; University of California - Riverside; Riverside, CA 92521, USA

[2]Neuroscience Graduate Program; University of California - Riverside; Riverside, CA 92521, USA

[3]Current Address: Medical College of Wisconsin - Milwaukee; Milwaukee, WI 53226, USA

*Correspondence: garret.anderson@ucr.edu

Summary.

Brain circuits are comprised of distinct interconnected neurons that are assembled by synaptic recognition molecules presented by defined pre- and post-synaptic neurons. This cell-cell recognition process is mediated by varying cellular adhesion molecules, including the latrophilin family of adhesion G-protein coupled receptors. Focusing on parahippocampal circuitry, we find that latrophilin-2 (Lphn2; gene symbol *ADGRL2*) is specifically enriched in interconnected subregions of the medial entorhinal cortex (MEC), presubiculum (PrS) and parasubiculum (PaS). Retrograde viral tracing from the Lphn2 enriched region of the MEC reveals unique topographical patterning of inputs arising from

the PrS and PaS that mirrors Lphn2 expression. Using a Lphn2 conditional knock-out mouse model, we find that deletion of MEC Lphn2 expression selectively impairs retrograde viral labeling of inputs arising from the ipsilateral PrS. Combined with analysis of Lphn2 expression within the MEC, reveals Lphn2 to be selectively expressed by defined cell types, and essential for MEC-PrS circuit connectivity.

Introduction.

Episodic learning and memory encoding in the brain involves interplay between the hippocampus and entorhinal cortex to provide detailed spatial and temporal information. Anatomically, there are classically defined cellular and pathway specific circuits that exist between the parahippocampal entorhinal cortex (EC) and hippocampal formation that allow for bi-directional communication between the two structures (Basu and Siegelbaum, 2015; Nilssen et al., 2019). Superficial layers of the EC (layers II/III) send their projections to the hippocampus, with layer II stellate cells projecting to the dentate gyrus and layer III pyramidal cells projecting to the stratum-lacunosum-moleculare region of the CA1. Reciprocally, hippocampal cells from the CA1 and subiculum project back to the EC to form synapses onto deep layer V cells. Layer II/III neurons receive synaptic input prominently from adjacent parahippocampal structures, the presubiculum (PrS) and parasubiculum (PaS), as well as long-range connections from contralateral PrS, PaS, and EC (Canto et al., 2012; Kononenko and Witter, 2012; Oh et al., 2014). In addition to cellular layer-specific synaptic communication, spatial-topographical circuit patterning is also widely observed throughout the hippocampal – entorhinal circuit. For example, spatially defined medial (MEC) and lateral (LEC) subregions of the EC have been linked to distinct circuitry and behavioral functions (Nilssen et al., 2019; Witter et al., 2017). The MEC

receives input from the PrS, PaS, retrosplenial and postrhinal cortex, all regions implicated for spatial and episodic memory processing (Boccara et al., 2010; Witter and Moser, 2006; Witter et al., 2017). The LEC in contrast, receives inputs from the perirhinal cortex and sensory areas, and is believed to be involved in attention and multi-sensory association processing (Basu and Siegelbaum, 2015; Witter et al., 2017).

The patterning of hippocampal – EC circuity is made possible by synaptic recognition molecules presented between defined pre- and postsynaptic cell types that permit for synaptic assembly amidst competing neural circuits. Recently, synaptic recognition molecules known as latrophilins (Lphn1, Lphn2, Lphn3; gene symbols *ADGRL1, ADGRL2, ADGRL3*) and their extracellular binding partners (e.g. Teneurins and FLRTs) have been implicated as critical players in guiding the specificity of neural circuit connectivity. Latrophilins belong to the adhesion family of G-protein coupled receptors (aGPCRs), consisting of relatively large extracellular domains along with classical 7-transmembrane GPCR domain structures that possess the ability to activate intracellular G-protein signaling cascades. Extracellular regions include lectin and olfactomedin domains that bind to Teneurins and FLRTs, which are synergistically required for excitatory synapse formation (Boucard et al., 2014; Li et al., 2018; Lu et al., 2015; O'Sullivan et al., 2012; Sando et al., 2019; Silva et al., 2011; Toro et al., 2020). Latrophilin binding to Teneurins and FLRTs is critically dependent on transcriptional alternative splicing, further serving to increase the molecular complexity required for synaptogenesis (Boucard et al., 2014; Li et al., 2018, 2020; Lu et al., 2015; Sando et al., 2019; Toro et al., 2020). Additionally, latrophilin dependent G-protein signaling has also been found to be required for synaptogenesis, suggesting both extracellular and intracellular domains of the molecule play essential roles in synapse formation (Sando and Südhof, 2021).

Lphn2 is unique among the latrophilin family, in that it is widely expressed outside the nervous system (Sugita et al., 1998), and its constitutive deletion results in embryonic lethality (Anderson et al., 2017). In the nervous system, Lphn2 is not ubiquitously expressed and subject to cell type specific expression regulation. In the hippocampus for example, Lphn2 and Lphn3 appear to have distinct expression patterning. Lphn3 is expressed by dentate gyrus, CA3 and CA1 neurons, while Lphn2 is expressed selectively by hippocampal CA1 neurons (Anderson et al., 2017; Sando et al., 2019). Although Lphn2 and Lphn3 are both expressed by CA1 pyramidal neurons, they are differentially localized to distinct synaptic connections. Lphn3 localizes to and controls the assembly of CA3 inputs onto CA1 pyramidal neurons in proximal regions within the stratum radiatum and stratum oriens, while Lphn2 regulates the entorhinal cortex synaptic connection onto distal tuft dendrites within the stratum lacunosum-moleculare (Anderson et al., 2017; Sando et al., 2019).

Given the marked cell-type specific expression and synapse specific function of Lphn2 observed in the hippocampus, in this study we investigate the role of Lphn2 in the greater hippocampal–entorhinal circuit. Surveying the expression of Lphn2 throughout the dorsal to ventral axis of the hippocampal formation and parahippocampal regions, we find remarkable region specific and cell type specific patterning of Lphn2 mRNA expression and protein localization. Using spatial mRNA analysis, we show that Lphn2 is selectively expressed by neurons in the CA1 and subiculum in the hippocampus, while parahippocampal expression is restricted to subregions of the Prs, PaS, and MEC with distinct topographical and layer specific expression patterning. Subdividing these regions into compartments along the proximal-distal axis (relative to the hippocampus), we observe enrichment in proximal PrS, distal PaS, and distal MEC. In the MEC, we find that

Lphn2 enrichment is confined to specific layers of the distal portion of this region. MEC Lphn2 is selectively expressed in superficial layers (II-III), with the highest levels of expression in *Oxr-1* expressing layer III and *Wfs-1* expressing layer II neurons. In distal MEC layer III neurons, we find that Lphn2 serves a functional role in controlling neuronal morphology, regulating spine numbers in select dendritic compartments. Further, we find that Lphn2 topographical expression patterns in PrS, PaS and MEC expression patterning are subregions interconnected with one another. To determine whether Lphn2 is necessary for development of this circuit, we performed retrograde labeling of MEC inputs in conjunction with MEC-targeted Lphn2 genetic deletion. In doing so, we find that deletion of Lphn2 within the MEC selectively impairs the retrograde labeling of MEC inputs arising from the ipsilateral PrS, revealing an essential role for Lphn2 in controlling topographic PrS-MEC connectivity.

Results.

Lphn2 protein localization is enriched in select hippocampal/parahippocampal regions

To understand the role of Lphn2 within the hippocampal–entorhinal circuit, we first began by constructing a three-dimensional atlas of Lphn2 protein expression throughout these interconnected brain regions. Serial horizontal sections (1.4-4.8 mm ventral to bregma) were collected from Lphn2-mVenus$^{fl/fl}$ transgenic mice (Anderson et al., 2017), and immunostained for GFP/mVenus to visualize Lphn2 expression/localization (Figure 1A). By aligning sections to regional maps, we subsequently quantified protein localization within regions of interest in the hippocampus and parahippocampal regions (Figure 1, Figure S1). As previously reported, we observed pronounced Lphn2 enrichment in the CA1 stratum lacunosum-moleculare region (SLM) while dentate gyrus (DG) and CA3

regions of the hippocampus were relatively devoid of Lphn2 expression (Anderson et al., 2017). Additionally, we found comparably high Lphn2 expression levels in the subiculum. Interestingly, while Lphn2 enrichment was observed in SLM and subiculum throughout the dorsal-ventral axis, there was a noticeable reduction in signal intensity toward more ventral sections (Figure 1C-D). Likewise, we examined Lphn2-mVenus localization in the parahippocampal cortical regions across the dorsal-ventral axis. To account for the different specific brain regions that are visible at different depths, for this first pass analysis we separated parahippocampal cortical regions into two generalized compartments: posterior-medial (encompassing regions including the visual cortex, MEC, PrS, PaS), and posterior-lateral cortical regions (encompassing LEC as well as auditory, perirhinal, and somatosensory cortices) (Figure 1A). Analyzing protein signals systematically in this fashion, a remarkably specific localization pattern became apparent. While dorsal posterior-medial sections (where visual cortex was visible) were largely devoid of Lphn2, a significant enrichment of Lphn2 was observed in more ventral sections, peaking where MEC was most visible and gradually decreasing at deeper positions. Conversely, posterior-lateral parahippocampal regions exhibited a relatively low abundance of Lphn2 signal throughout the dorsal-ventral axis (Figure 1E,F). Taken together, these data show that Lphn2 protein localization is most pronounced in the dorsal regions of the hippocampus and MEC, with a gradual decrease in expression along the dorsal-ventral axis in both of these regions.

Latrophilin-2 is topographically expressed and localized in medial parahippocampal regions

With closer examination of Lphn2 enrichment observed in the posterior-medial parahippocampal regions containing dorsal MEC, it becomes clear that Lphn2 is not ubiquitously expressed. Rather, a distinct topographical and layer-specific expression pattern is observed within the parahippocampal region. In horizontal sections with peak entorhinal Lphn2 expression (2.6 mm ventral from bregma), we observed noteworthy topographical patterning of Lphn2 protein localization in the MEC as well as the nearby PrS and PaS. Dividing each region into proximal and distal subregions (relative to hippocampal DG), we found Lphn2 to be consistently enriched in proximal PrS, distal PaS, and distal MEC (Figure 2A,C). To investigate this patterning at the transcription level, we then turned to an mRNA spatial analysis method. Using single-molecule RNA fluorescent in-situ hybridization (smFISH), we performed spatial mRNA quantification in horizontal tissue sections at the same depth. In doing so, we observed an expression pattern strikingly similar to that of the Lphn2 protein. Lphn2 mRNA was found enriched in hippocampal CA1 and subiculum, as well as proximal PrS, distal PaS, and distal MEC compartments (Figure 2D-F). These data strongly suggest that Lphn2 mRNA is both synthesized and localized within cells of these specific regions.

Lphn2 is expressed by layer specific MEC neurons

In addition to unique topographical patterning observed within the parahippocampal regions, the distal MEC region also exhibited layer-specific expression patterning of Lphn2 mRNA and protein. To examine this further, we first used spatial

smFISH to investigate cell type specific Lphn2 mRNA expression in the region. Using intermediate horizontal brain slices containing hippocampal and EC regions, we surveyed brains from both juvenile (P10; Figure 3) and mature mice (P30; Figure S2) to examine Lphn2 expression before and after the circuit is established (Donato et al., 2017; Ray and Brecht, 2016). Combining probes for Lphn2 and the neuron-specific nuclear marker NeuN, we observed similar cell type specific expression patterning at both P10 and P30. P10 animals, like P30, exhibited abundant Lphn2 expression in the CA1 pyramidal neuron layer and were largely devoid of Lphn2 expression in DG granule neurons (Figure 3B, S2B). Analyzing Lphn2 transcripts co-located with neuronal nuclei (NeuN+/DAPI+) or non-neuronal nuclei (NeuN-/DAPI+), we classified cells in each subregion into one of four categories based on the presence or absence of Lphn2 and NeuN (Figure 3C; S2C). We found that in distal regions of the CA1, nearly all pyramidal neurons (~90%) expressed detectable Lphn2 signal, while only a small fraction (<5%) of DG granule neurons were Lphn2+. (Figure 3C-D, S2C-D). Additionally, even among Lphn2+ DG neurons, the expression level per cell was ~5 fold less than that of Lphn2+ CA1 pyramidal neurons (Figure 3D, S2D). Along with our protein data (Figure 1-2), these findings are in line with previous work showing Lphn2 is expressed specifically within CA1 pyramidal neurons, (but not DG or CA3), where it functions in distal dendritic tufts in the SLM to regulate the assembly of EC-CA1 synaptic inputs (Anderson et al., 2017; Sando et al., 2019).

In the distal MEC region where Lphn2 mRNA and protein enrichment was also observed, we found a distinct layer-specific expression pattern. Lphn2 signal intensity increased continuously along the superficial-deep axis, reaching a peak at the end of layer III, before dropping precipitously at the transition zone (layer IV) and remaining low in the deep layers (V/VI) (Figure 3E). As before, we classified cell type specific expression in each layer

based on the presence or absence of Lphn2 and NeuN (Figure 3F, S2F). In layer I, which is largely devoid of neurons, Lphn2 was almost exclusively found in non-neuronal cells. In the remaining layers, we found that superficial layers (II/III) and deep layers (V/VI) exhibited similar cell type distributions, with the majority of cells (60-70%) being neurons with detectable Lphn2 expression (Figure 3F, S2F). Striking differences arose, however, when analyzing the Lphn2 expression levels between these cells. For non-neuronal cells with detectable Lphn2 transcripts, expression levels were low across all layers (Figure 3G, S2G). In neurons, however, we observed a gradient of low Lphn2 transcript density in layer I to a peak in layer III and subsequent drop in layers V/VI, mirroring the overall layer-specific intensity measurements (Figure 3G, S2G). Thus, Lphn2 in the hippocampus and EC is expressed in a cell type and region-specific manner, with Lphn2 in the distal MEC being expressed by superficial layers with an enrichment gradient towards deeper layer III neurons.

To confirm the observed regional proximal-distal Lphn2 expression gradients, we examined Lphn2 mRNA expression in relation to parahippocampal region-specific markers: wolframin syndrome-1 (*Wfs1*) and oxidation resistance protein-1 (*Oxr1*). *Wfs1* is expressed by MEC layer II pyramidal neurons and throughout PaS (Kawano et al., 2009), while *Oxr1* is expressed selectively in MEC layer III pyramidal neurons (Suh et al., 2011). Using these two markers, we were able to clearly identify regional boundaries between PrS, PaS, MEC and perirhinal cortex (PRh) (Figure 4A-B). Using *Wfs1* as a marker to differentiate PrS and PaS regions, we quantified Lphn2 expression at the cellular level at the proximal and distal ends of each region. Consistently, we found that Lphn2 is significantly enriched in proximal PrS and distal PaS cells, and nearly absent in the opposing compartments (Figure 4C-F), matching our earlier observations.

We then focused on dissecting out cell type specific Lphn2 expression in the proximal versus distal compartments of the MEC. *Oxr1* was chosen as a selective marker for layer III pyramidal neurons and to specifically delineate the MEC borders (Figure 4G). For layer II excitatory neurons, we selected two probes: W*fs-1* (to label pyramidal neurons) and *Reelin* (to label stellate neurons). These specific probes allowed us to not only differentiate between layer II/III neurons, but also to classify layer II neurons possessing distinct projection patterning in the EC-hippocampal circuit. *Reelin* expressing layer II MEC cells are stellate neurons that send their axonal projections to the hippocampal DG as part of the tri-synaptic pathway (Kitamura et al., 2015). Conversely, *Wfs-1* expressing layer II MEC neurons are pyramidal neurons with axons projecting selectively to the hippocampal stratum lacunosum (Kitamura et al., 2014). Finally, *Oxr-1* expressing layer III MEC neurons are pyramidal neurons that project to the hippocampal stratum moleculare (Suh et al., 2011). Based on expression patterning spanning layers II/III, we chose to separate *Oxr1*+ cells into two categories for analysis: (1) Superficial layer III cells, located along the layer II/III border (Figure 4I) and (2) Deep layer III cells, close to the layer III/IV border (Figure 4J). Using these panels of expression markers, we proceeded to quantify cell type specific Lphn2 expression in the superficial layers of proximal/distal subregions of the MEC. Compared to distal MEC, Lphn2 expression in proximal MEC was drastically lower for all excitatory neuron types (Figure 4L). Among layer II excitatory neurons, *Wfs1*+ neurons showed significantly higher Lphn2 expression compared to *Reelin*+ neurons at both proximal and distal ends of MEC, with the greatest overall expression observed in the distal MEC (Figure 4L). For layer III *Oxr1* expressing cells, we likewise found significant Lphn2 enrichment in deeper layer III neurons as compared to those at the layer II/III boundary in both proximal and distal compartments, with highest expression levels once

again observed in the distal MEC (Figure 4L). Thus, excitatory layer II/III neurons exhibits both topographical patterning as well as cell type specific expression. To confirm cell type specific expression that we observed between *Wfs1/Reelin/Oxr1* cell types, we performed Lphn2 gene expression analysis on the Allen Brain Institute's publicly available single cell RNA sequencing (scRNAseq) database (Tasic et al., 2018). Analyzing EC cells expressing *Wfs1/Reelin/Oxr1* markers from this scRNAseq database, we found abundant Lphn2 detection in *Wfs1 and Oxr1* expressing cells, and sparse Lphn2 detection in *Reelin* expressing cells (Figure S3A-B). Pooled smFISH data collected across the entirety of the MEC regardless of topographical position, showed similar Lphn2 expression patterning (Figure S3C). To compare our excitatory projection neuron analysis results with local inhibitory interneuron cell types, we performed smFISH using probes for parvalbumin (PV) and somatostatin (SST) (Figure 4K), the two most abundant subtypes of GABAergic interneurons in the MEC (Miao et al., 2017; Witter et al., 2017). In both of these GABAergic cell types, we found detectable levels of Lphn2 expression (Figure 4L). Unlike in excitatory neurons however, Lphn2 did not show any distinct enrichment in one GABAergic cell type over another, nor was there any discernible difference in expression between topographical positions (Figure 4L). Taken together, these data show that Lphn2 expression enrichment observed in the distal MEC is due to transcription in *Wfs1*+ and *Oxr1*+ excitatory cell types, both of which are projection neurons that send their axons to the SLM.

Lphn2 protein localization in the medial entorhinal cortex is confined to superficial layers and dependent on MEC cell expression

Having confirmed layer and cell type specific Lphn2 mRNA expression in the distal MEC, we next chose to further investigate its protein localization in the region using Lphn2-mVenus$^{fl/fl}$ mice. Based on our earlier experiments, we used dorsal horizontal sections (2.6 mm ventral from bregma), where Lphn2 expression peaks in distal MEC and delineates a sharp, clear border from the adjacent PRh (Figure 5A-B). To compare layer specificity of Lphn2 protein expression in each region, we measured Lphn2-mVenus fluorescence intensity across the layers on each side of the MEC/PRh border. While the Lphn2 signal in PRh was negligible with no discernible enrichment in any layer, MEC exhibited a remarkable layer-specific expression profile (Figure 5B). Lphn2 protein expression was largely confined to the superficial layers (I-III) of MEC with abundant signal in layer I, a slight reduction in layer II, and a steady increase in protein signal up to a peak deep in layer III. Similar to Lphn2 mRNA expression, Lphn2 protein expression decreased dramatically in the thin transition zone of layer IV, ending with negligible expression in the deep MEC layers (V/VI) (Figure 5B). We proceeded to quantify this layer-specific protein localization across the dorsal-ventral axis (Figure 5C). In doing so, we detected low Lphn2 protein signal across all dorsal V1 visual cortical layers, followed by Lphn2 enrichment in dorsal MEC superficial layers, with a gradual dampening of signal intensity towards ventral MEC (Figure 5C-D). Despite a gradual dampening of the overall Lphn2 signal in more ventral sections, Lphn2 retained its layer-specific patterning in MEC-containing slices throughout the dorsal-ventral axis (Figure 5C-D). Having shown that MEC Lphn2 protein localization is layer specific in mature animals, we next examined how this protein signal arises during postnatal development (Figure S4). Sampling weekly postnatal time points

(P0, P7, P14, P21, P30), we found that MEC layer-specific Lphn2 patterning was already set at birth and remained intact through maturation. Conversely, Lphn2 was equally distributed across CA1 layers (oriens, radiatum, SLM) at birth, with only a slight enrichment in SLM by P7 and finally a dramatic increase in SLM-specific Lphn2 starting at P14. Thus, MEC Lphn2 protein localization patterning precedes that of CA1, suggesting differences in Lphn2 developmental trafficking between these cell types that coincides with the developmental timespan for this circuit (Donato et al., 2017; Muessig et al., 2015; Witter et al., 2017).

In the hippocampal SLM, Lphn2 protein signal is visible under confocal microscopy as discrete puncta associated with synapses (Anderson et al., 2017). To examine layer-specific Lphn2 expression in greater detail, we captured high-resolution confocal image stacks of Lphn2-mVenus puncta in each MEC layer. Quantifying the density of Lphn2 puncta in each volume, we found that Lphn2 density patterning was nearly identical to the layer-specific intensity patterning (Figure 5B), with enrichment of Lphn2 puncta in superficial layers and peak puncta density within layer III (Figure 5E-G). To determine what proportion of Lphn2 is specifically expressed within the MEC, we genetically deleted local Lphn2 expression with viral stereotaxic targeting. Into the MEC of P30 Lphn2-mVenus$^{fl/fl}$ mice, we stereotactically co-injected AAVs expressing Cre-recombinase (hSyn-Cre-AAV5; to delete the floxed Lphn2-mVenus) and Cre-dependent tdTomato (CAG-FLEX-tdTomato-AAV5; to verify correct targeting). Control animals were injected with a single AAV expressing tdTomato for target visualization (CAG-tdTomato-AAV5). Injected mice were then analyzed at P45 using confocal imaging and Lphn2 puncta density measurements (Figure 5H-J). MEC-targeted Lphn2 deletion caused a robust loss of Lphn2 protein signal in superficial layers (Figure 5J), thus corroborating our transcriptional data

that Lphn2 protein is being locally expressed within the MEC region. Taken together with our mRNA analysis, these findings suggest that Lphn2 is transcriptionally produced by select layer II and III pyramidal cells, resulting in Lphn2 protein enrichment within these layers. Further, these pyramidal neurons also appear to traffic Lphn2 out to their distal tuft dendrites present in layer I, similarly as described for CA1 pyramidal neurons (Anderson et al., 2017)

Latrophilin-2 KO in distal MEC pyramidal neurons causes compartment specific spine alterations

We next proceeded to test the functional role of Lphn2 in distal MEC neurons by assessing morphological alterations that may result from genetic deletion. In hippocampal CA1 pyramidal neurons, Lphn2 deletion significantly reduces dendritic spine numbers specifically on distal dendritic tufts in the SLM (Anderson et al., 2017), indicating a crucial role in spine development in this region. To test whether Lphn2 is similarly necessary for spine development in distal MEC neurons, we performed AAV stereotaxic injection experiments to sparsely label neurons early in development (P3) and visualize spine morphology after maturation (P30). Using Lphn2-mVenus$^{fl/fl}$ mice to remove Lphn2 expression before circuit development, control neurons were labeled with tdTomato expressing AAVs (CAG-tdTomato-AAV5), while Lphn2 MEC knock-out neurons (Lphn2-MEC-KO) were labeled via a cocktail AAV injection of Cre-recombinase (hSyn-Cre-AAV5) and Cre-dependent tdTomato expressing AAV (CAG-FLEX-tdTomato-AAV5). After confirming sparse neuron labelling in the MEC, we used confocal imaging to capture neurons and their local dendrites from distinct MEC layers (Figure 6A). Distal dendrites that were outside of the field of view from the soma, such as those projecting out to layer

I, were not included in this analysis to maintain accurate attribution of dendrites that are connected to the spatially defined neuron. Given that Lphn2 mRNA and protein were both largely concentrated in deep layer III, we reasoned that the effects of Lphn2 deletion on spine morphology would likely be most evident in proximal dendrites of the resident neurons in this layer. With this in mind, we used Imaris 3D analysis software to reconstruct and analyze proximal dendrites and spines in 3-dimensions, with a focus on layer III neurons. Resulting control and Lphn2-KO animals spine densities were compared for two positions in layer III: pyramidal neurons positioned superficially in close proximity to layer II (Figure 6D-F), and deep layer III pyramidal neurons in close proximity to layer IV (Figure 6G-I). Spine densities were broken down into basal and apical dendrite categories, with apical further subdivided into primary and secondary to reflect the functional differences between these levels.

Within the basal and secondary apical dendrites of superficial layer III neurons, we found no significant differences in spine density between control and Lphn2-KO (Figure 6D-F). However, Lphn2-deficient superficial layer III neurons displayed a significant increase in spine density in their primary apical dendrites compared to controls (Figure 6D-F). In deep layer III neurons, Lphn2 deletion produced even more robust dendrite-specific spine density changes. While we found no difference in basal dendrite spine densities, we observed bi-directional changes between primary (increase) and secondary (decrease) apical dendrite spine densities following Lphn2 deletion (Figure 6G-I). Layer V pyramidal neurons, analyzed as a control, showed no significant changes in local spine densities for any dendritic compartments (Figure 6J-L). Altogether, MEC neurons that express Lphn2 at the highest levels (deep layer III) showed the most robust spine morphological alterations after Lphn2 deletion. Further, Lphn2 deletion does not result in

a simple loss of spine numbers. Alongside the loss of spines within Lphn2 enriched zones, there seems to be a compensatory increase in spines along the primary apical shaft of these neurons indicating altered compartmentalization of normal spine development.

Latrophilin-2 controls input specific distal MEC connectivity

Having established that Lphn2 controls cell type specific morphological patterning in MEC, we next asked how Lphn2 might influence connectivity from inputs that project onto these MEC cells. The MEC receives numerous layer-targeted inputs including hippocampal projections to deep layer V (Sürmeli et al., 2015), and parahippocampal projections from PrS and PaS that target superficial layers I-III (Kononenko and Witter, 2012). To determine the role of Lphn2 in controlling input connectivity into the MEC, we first asked the question: What differing inputs are connected to the proximal versus distal MEC positions? Using retrograde viral injections to label input regions for proximal and distal MEC, we performed an initial experiment to assess proximal MEC versus distal MEC connectivity patterning in the interconnected hippocampal and parahippocampal regions. Retrograde AAVs expressing tdTomato or GFP (Tervo et al., 2016), were stereotactically injected on one hemisphere targeting the proximal or distal compartments of dorsal MEC respectively at P35 and input labeling was examined 10 days later (Figure 7A). At the site of injection, in addition to local infectivity (Figure 7A-B), we observed prominent topographical labeling of known MEC inputs on the ipsilateral side including hippocampal CA1 and subiculum, as well as parahippocampal regions on both hemispheres (Figure 7B). For both proximal and distal dorsal MEC retrograde AAV injections, we observe the highest level of CA1 and subiculum infected cells in the dorsal hippocampus, and similar attenuating infectivity with further ventral progression. Differences between the two

injection sites exist however, when comparing the topographical labeling of cells within the highly infected dorsal hippocampal horizontal sections. Distal MEC injections resulted in proximal CA1 and distal subiculum labeling, while proximal MEC injections labeled adjacent regions of the distal CA1 and proximal subiculum (Figure 7B). Topographical gradients of hippocampal projections to the entorhinal cortex have previously been described for the medial and lateral EC (Nilssen et al., 2019), and here we find topographical patterning also occurs within subregions of the MEC, suggesting that additional complexity exists within the hippocampal to EC circuit. Interestingly, inputs from PrS and PaS also displayed striking differential proximal-distal patterning between the two injection sites, consistent with previous reports (Caballero-Bleda and Witter, 1993). Distal MEC injections revealed projections specifically from proximal PrS and distal PaS compartments on the ipsilateral side, which is mirrored on the contralateral hemisphere (Figure 7B). We also observed pronounced labeling in distal MEC layer II/III cells on the contralateral side (Figure 7B) as previously reported (Fuchs et al., 2016; Nilssen et al., 2019). Proximal MEC inputs conversely, arose from bilateral distal PrS and proximal PaS, as well as contralateral proximal MEC (Figure 7B). In summary, proximal and distal MEC neurons receive inputs from topographically distinct hippocampal and parahippocampal subregions (summarized in Figure 7C). Remarkably, distal MEC parahippocampal connectivity patterning mirrored the topographical expression patterning of Lphn2 (Figure 2).

Given this finding, we hypothesized that Lphn2 expression in the distal MEC controls the connectivity patterning between these parahippocampal regions. To test this, we first injected neonatal Lphn2$^{fl/fl}$ mice with Cre-recombinase expressing AAV targeting the MEC on one hemisphere to knock-out Lphn2 expression (Lphn2-MEC-KO; Figure 7D).

After maturation (P35), Lphn2-MEC-KO animals and littermate controls (no neonatal cre) were then injected with a distal MEC-targeted retrograde tdTomato expressing AAV on the same previously injected hemisphere, to label distal MEC inputs (Figure 7E). Focusing our analysis on the parahippocampal regions, we imaged and counted the number of labelled neurons in the PrS, PaS, and MEC on both hemispheres. In doing so, we found an unexpectedly selective change in the labeling of distal MEC inputs. In Lphn2-MEC-KO animals we observed no change in ipsilateral PaS labeling, but a significant reduction (~50%) in ipsilateral PrS labeling (Figure 7F). On the contralateral hemisphere, retrograde AAV labeling patterning appeared fully intact in the PrS, PaS, and MEC (Figure 7G-H). These findings suggest that Lphn2 plays an input-selective role in circuit establishment for the distal MEC, being selectively essential for ipsilateral proximal PrS inputs.

Discussion.

Cell adhesion molecules such as latrophilins are emerging as critical players during neural circuit development. Governing processes such as cell migration, axonal pathfinding, specification and assembly of synaptic sites, latrophilins play multiple roles during brain development in concert with their proteomic binding partners. At the cellular level, gene expression and alternative splicing control unique elements of these developmental processes, which leads to shifting roles for latrophilin containing complexes during the brain maturation process. Cell adhesion molecule presentation can control cell migration during embryonic development, axonal/dendritic pathfinding attraction/aversion during early postnatal development, synapse specific assembly, and maintenance/functional roles in mature circuits. While essential for both embryonic and postnatal development, it is becoming clear that latrophilin-2 (Lphn2) is not ubiquitously

expressed by all cell types. Rather, there appears to be cell type specific control of transcription, making its role in circuit development context-dependent. In hippocampal CA1 pyramidal neurons for instance, Lphn2 appears to have unique functionality in controlling synaptogenesis with EC inputs which cannot be replicated by other latrophilin molecules (Anderson et al., 2017; Sando et al., 2019). Likewise, in these same CA1 pyramidal neurons, latrophilin-3 (Lphn3) has unique functionality in controlling synaptogenesis with CA3 inputs which are also non-overlapping with other latrophilins (Sando et al., 2019). However, in other contexts latrophilins can be overlapping and function redundantly with each other. For example, in cerebellum Purkinje cells Lphn2 appears to have redundant functionality with Lphn3 in controlling synaptogenesis from parallel fiber inputs (Zhang et al., 2020). Thus, the degree to which individual latrophilin genes function independently, appears to be entirely context dependent.

Here, we examined Lphn2 cell type expression specificity in the hippocampal and parahippocampal regions throughout the dorsal-ventral axis. In doing so, we found hippocampal Lphn2 to be selectively expressed by CA1 and subiculum neurons with a dorsal to ventral protein enrichment gradient. In parahippocampal regions**,** we found that Lphn2 is selectively expressed in a topographical manner in the dorsal MEC, with expression tapering towards ventral MEC but retaining topographical patterning. Anatomically, EC to hippocampal connectivity is topographical in nature with dorsal to dorsal, intermediate to intermediate, and ventral to ventral connectivity (Fanselow and Dong, 2010; Groen et al., 2003). We found a distinct expression gradient in both the hippocampus and entorhinal cortex with dorsal enrichment in both of these regions, suggesting that Lphn2 has a preferential functional role for dorsal regions. Dorsal and ventral hippocampal input and output circuitry are not only anatomically unique, but their

physiological roles are likewise distinct. The dorsal hippocampus is critical for spatial learning and memory (Moser et al., 1995), whereas the ventral hippocampus is linked to emotion and motivation driven behaviors (Henke, 1990). Additionally, the entorhinal cortex can be further divided into its layer defined cell types which contribute to pathway specific circuitry and behavior. Layer II stellate cells are the primary output to the hippocampal DG, whereas layer II/III pyramidal cells project to the CA1 and subiculum. These distinct pathways have been proposed to have differential roles in behavioral processing, with EC layer II to DG pathway being important for spatial representation encoding and the EC layer II/III to CA1/subiculululum pathway controlling time related aspects of episodic memory (Kitamura et al., 2014, 2015; Suh et al., 2011). Consistent with this, Lphn2 brain-specific deletion has been found to affect specific elements of spatial-temporal sequence pattern learning, in line with its role in controlling cell type specific information flow through the dorsal hippocampal-entorhinal circuit (Anderson et al., 2017).

With our finding that Lphn2 is enriched primarily in the dorsal MEC, we focused on characterizing cell type specific expression responsible for this enrichment. In doing so we found Lphn2 transcriptional enrichment in selective superficial layer neurons, the *Oxr1*+ layer III and *Wfs1*+ layer II MEC pyramidal neurons. These cell types send their projections to the SLM of the hippocampus (Kitamura et al., 2014; Suh et al., 2011), where Lphn2 protein is also found to be enriched (summarized in Figure S5A). This Lphn2+ MEC to Lphn2+ SLM connectivity is consistent with what has been previously proposed for Lphn2 function in a different circuit, hippocampal CA1 to subiculum connections (Pederick et al., 2021). In this circuit, Lphn2 and the latrophilin ligand teneurin-3 (Ten3) are expressed in a non-overlapping manner in adjacent subregions of both the CA1 and subiculum (Berns et al., 2018; Pederick et al., 2021). This patterning is functionally important, as it serves to

direct correct CA1 to subiculum axonal targeting via attraction and repulsion mechanisms. Subiculum Lphn2+ neurons attract axons from Lphn2+ CA1 neurons, while simultaneously repelling axons from Ten3+ CA1 neurons (Pederick et al., 2021). Likewise, Ten3+ CA1 neurons connect selectively to Ten3+ neurons in the subiculum (Berns et al., 2018). Consistent with these observations, here we also observe similar Lphn2+ expression and connectivity patterning in the topographical parahippocampal network. Using retrograde labeling of the Lphn2 enriched region of the distal MEC, we find that its inputs arise from the likewise Lphn2 rich regions of the proximal PrS and distal PaS (summarized in Figure S5B). This expression patterning strongly suggests that Lphn2+ to Lphn2+ circuitry guidance mechanisms are at work to properly establish the connectivity between these regions. Perhaps surprisingly however, deletion of Lphn2 from the MEC appears to have a very discerning impact on connectivity as measured in our study here. By performing genetic deletion in tandem with retrograde labeling of inputs into the distal MEC, labeling of the major inputs appears largely intact with exception of the ipsilateral PrS.

To understand why this PrS-MEC connectivity would be preferentially impacted by Lphn2 deletion, there are several possible explanations. For example, previous anatomical analyses surveying PrS/PaS to EC connectivity have revealed differences in connectivity depending on EC cell type. PrS forms 2-3 times more connections to layer III cells than layer II, and conversely PaS form preferential connections with layer II cells over layer III (Caballero-Bleda and Witter, 1994). Given the enrichment in Lphn2 transcripts we observed in layer III cells (Figure 4), Lphn2 deletion in the MEC might disproportionately impact PrS to MEC connections. Additionally, Lphn2 may have redundant functionality with other latrophilins (or other circuit guiding molecules) for the other MEC inputs and are

successfully able to offset Lphn2 loss, similarly to that observed in cerebellum Purkinje cells (Zhang et al., 2020). While other inputs appear to be unaffected by retrograde labeling, Lphn2 controlling MEC circuit functionality might still be impacted in a more subtle circuit rewiring. For example, Lphn2 control of dendritic spine numbers in MEC neurons paints a picture of compartmentalization alterations in dendritic morphological patterning (Figure 6). In deep layer III MEC neurons, we found deficits in local secondary dendritic spine numbers. In these same neurons however, we also observed an increase in spine-like protrusions coming off the primary apical dendrite. This structural alteration might be a compensatory change resulting from the loss of secondary apical dendritic spines, or potentially a shift in positioning of neural circuit connections. Spine densities shifting from secondary apical dendrites towards primary apical dendritic branches could likewise suggest changes in the placement of synapses.

While the full implications of these types of compartmentalization changes and how they can influence circuitry are unknown, potential alterations in synaptic positioning necessitate further investigation of these possibilities. Nonetheless, the specificity with which Lphn2 is expressed within interconnected parahippocampal regions suggests an intriguing role in shaping MEC circuitry. Between its topographical patterning, cell type specific transcriptional specificity, and functional control of PrS to MEC connectivity, Lphn2 appears to play a key role during parahippocampal circuitry development.

Limitations of the study.

The viral and stereotaxic delivery approaches used in this study result in incomplete genetic deletion, due to incomplete infectivity and targeting limitations. While the circuitry deficits we observe appear confined to ipsilateral PrS to MEC connections,

more subtle synaptic alterations (e.g. synapse numbers, location, strength, and plasticity) as a result of Lphn2 genetic elimination was not surveyed and might still be impacted. Additionally, the structural effects on neurons reported here only survey dendritic elements in close proximity to the cell body, and analysis of the additional neuronal compartments is incomplete. The patterning of parahippocampal inputs in forming synapses onto specific MEC neuron dendritic positions is not assessed in this study, nor is the effect of Lphn2 deletion on this patterning.

Acknowledgements.

This paper was supported by a grant from the Whitehall Foundation (2018-08-01) and Initial Complement Funds from the University of California, Riverside to G.R.A.

Author Contributions. J.D.D. designed, performed, and analyzed most experiments; T.R.M. and G.R.A. helped design experiments and quantification methods; T.R.M. designed custom MATLAB scripts for Imaris data analysis; A.K. performed scRNAseq analysis; R.F.A., A.J.W., E.D.L. performed neuron reconstructions; L.S. quantified retrograde connectivity data; H.P. performed smFISH data analysis; M.T.A. contributed to Imaris data analysis; J.D.D., T.R.M. and G.R.A. wrote the paper with input from all of the authors.

Declarations of interests. The authors declare no competing interests.

Main Figures and Title Legends.

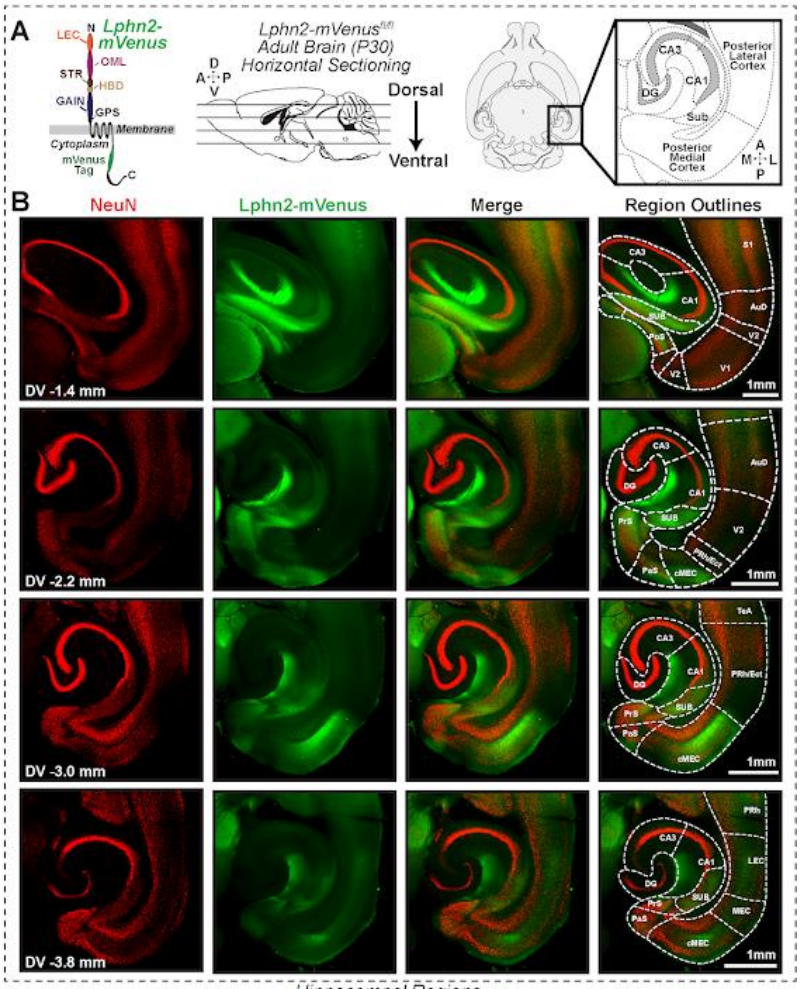

Figure 1. Dorsal to ventral Lphn2-mVenus protein distribution across hippocampal and interconnected cortical regions. (A) *Left,* The domain architecture of Lphn2-mVenus protein (Lectin Domain (LD); Olfactomedin like domain (OML); Serine/threonine rich region (STR); hormone binding domain (HBD); G-protein coupled receptor (GPCR) autoproteolysis inducing domain (GAIN); GPCR proteolysis site (GPS) found in Lphn2-mVenus$^{fl/fl}$ transgenic mice used for this study, containing mVenus label placed in the intracellular tail region. *Middle,* Horizontal sections were acquired along the dorsal to ventral axis in P30 mice. *Right,* Major regions in the hippocampal formation dentate gyrus (DG), CA1-3, Subiculum (Sub), and generalized medial/lateral regions of the posterior cortex. **(B)** Representative images of select sections spanning the dorsal to ventral regions (slices -1.4, -2.2, -3.0, -3.8mm ventral from bregma) stained for neuronal marker NeuN (to label neuronal cell bodies) and GFP (to label Lphn2-mVenus). For full panel of serial section images and mapping abbreviations, see supplemental figure 1. **(C-D)** Quantification of fluorescence intensity arbitrary units (A.U.) for hippocampal subregions across dorsal to ventral horizontal sections (-1.4mm to -3.8mm) **(C)** and **(D)** Summary graphs of dorsal and ventral slices (3 section mean); (n=5 mice). **(E-F)** Similar to C-D, except for quantification of fluorescence intensity across medial/lateral regions of the posterior cortex. Intermediate region shown include 2-section mean of peak posterior-medial cortical sections (-2.6mm). Data shown are means ± SEM; Statistical analysis was performed by one-way ANOVA with Tukey's post-hoc test for multiple comparisons (**=P<.01).

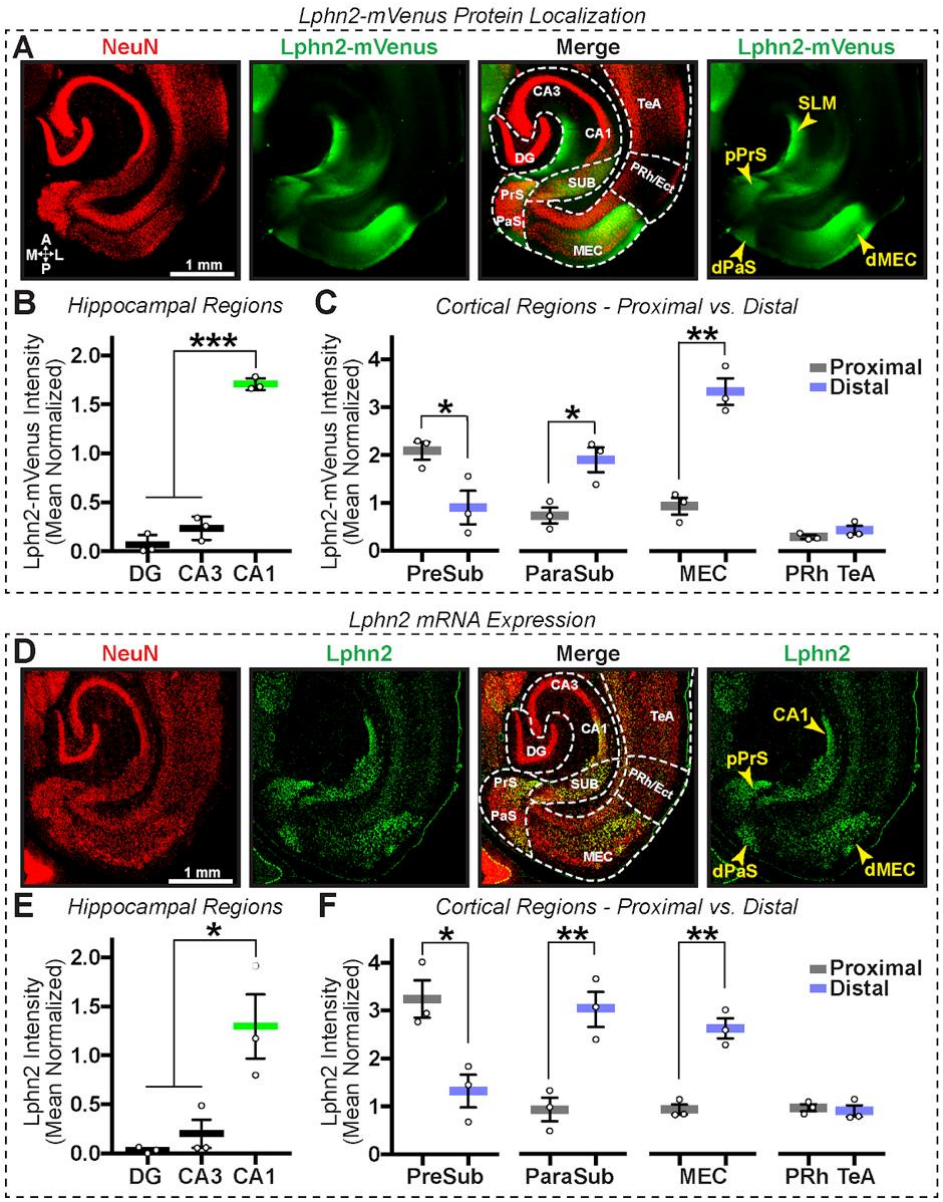

Figure 2. Latrophilin-2 is expressed and localized to distinct proximal or distal compartments of parahippocampal regions. (A) Representative horizontal section (-2.6mm from bregma) from Lphn2-mVenus P30 mouse IHC stained for neuronal nuclei (NeuN), GFP (Lphn2-mVenus), merged image with map overlay (Paxinos and Franklin, 2004), Lphn2 image with yellow arrows indicating the proximal and distal parahippocampal subregions with Lphn2 enrichment. SLM = stratum lacunosum-moleculare; pPrS = proximal presubiculum; dPaS = distal parasubiculum; dMEC = distal medial entorhinal cortex **(B-C)** Summary graphs of normalized fluorescence intensity between **(B)** Hippocampal subregions of dentate gyrus (DG), CA3 and CA1 subregions, and **(C)** Proximal/distal subregions of PrS, PaS, MEC, and further distal-lateral perirhinal (PRh) and temporal-association (TeA) cortical regions. **(D-F)** Similar to A-B, except for single molecule RNA in-situ fluorescence hybridization (smFISH) detection of NeuN and Lphn2 transcripts. Data shown are means ± SEM; (n=3 mice); Statistical analysis was performed by Student's t-test (C/F) or one-way ANOVA with Tukey's post-hoc test for multiple comparisons (B/E) (*=P<0.05, **=P<.01).

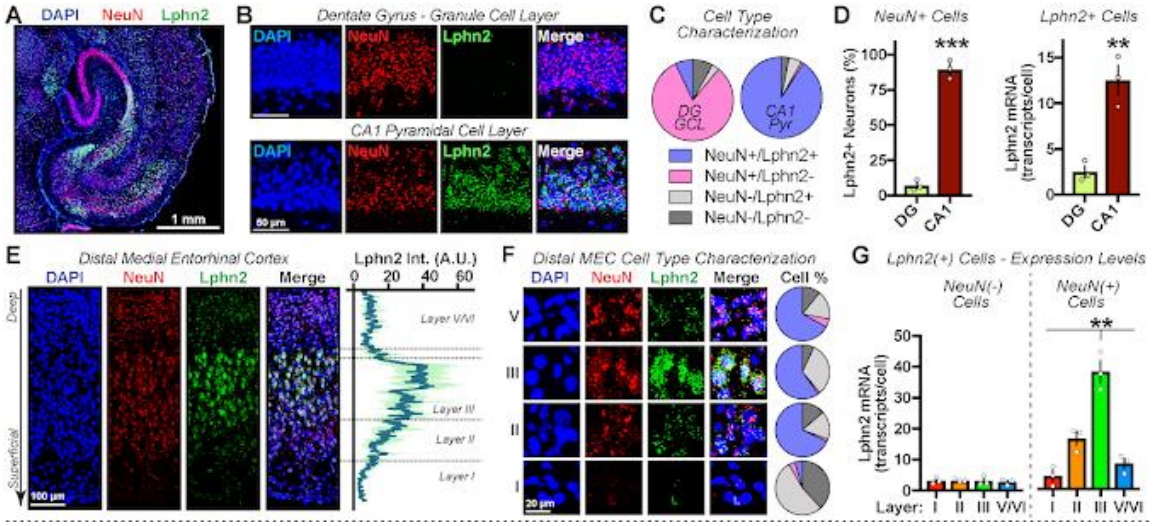

Figure 3. Latrophilin-2 mRNA expression is enriched in layer 3 MEC neurons. (A) Representative confocal image of P10 horizontal brain section using single molecule RNA *in situ* hybridization for Lphn2 (green) and NeuN (red) mRNA. DAPI (blue) fluorescence shown for visualization of all nuclei. **(B-D)** Hippocampal Lphn2 expression is cell type specific. **(B)** Zoomed in images of DG granule layer and CA1 pyramidal layer, **(C)** Cell type classification percentage breakdown based on neuronal (NeuN+) and non-neuronal (NeuN-) cells, with (Lphn2+) or without (Lphn2-) detectable Lphn2 expression, and **(D)** *Left,* Total percentage summary graph of Lphn2 expressing neurons in the DG and CA1; *Right,* Lphn2 transcripts per NeuN+/Lphn2+ cell in each region. **(E-G)** Distal MEC Lphn2 expression is layer specific. **(E)** *Left,* zoomed in confocal image for the distal MEC comparing Lphn2 expression across the layers; *Right,* fluorescence intensity line measurements across the indicated layers of distal MEC. **(F)** Representative confocal images in distal MEC for each indicated layer, alongside quantification of cell type as in **C. (G)** Summary graphs of cells with detectable Lphn2 expression (Lphn2+) for non-neuronal (Left, NeuN-) and neuronal (right, NeuN+) cells across distal MEC layers. Data shown are means ± SEM (n=3 mice); Statistical analysis was performed by Student's t-test (D) or one-way ANOVA with Tukey's post-hoc test for multiple comparisons (G) (**=P<.01, ***=P<.001).

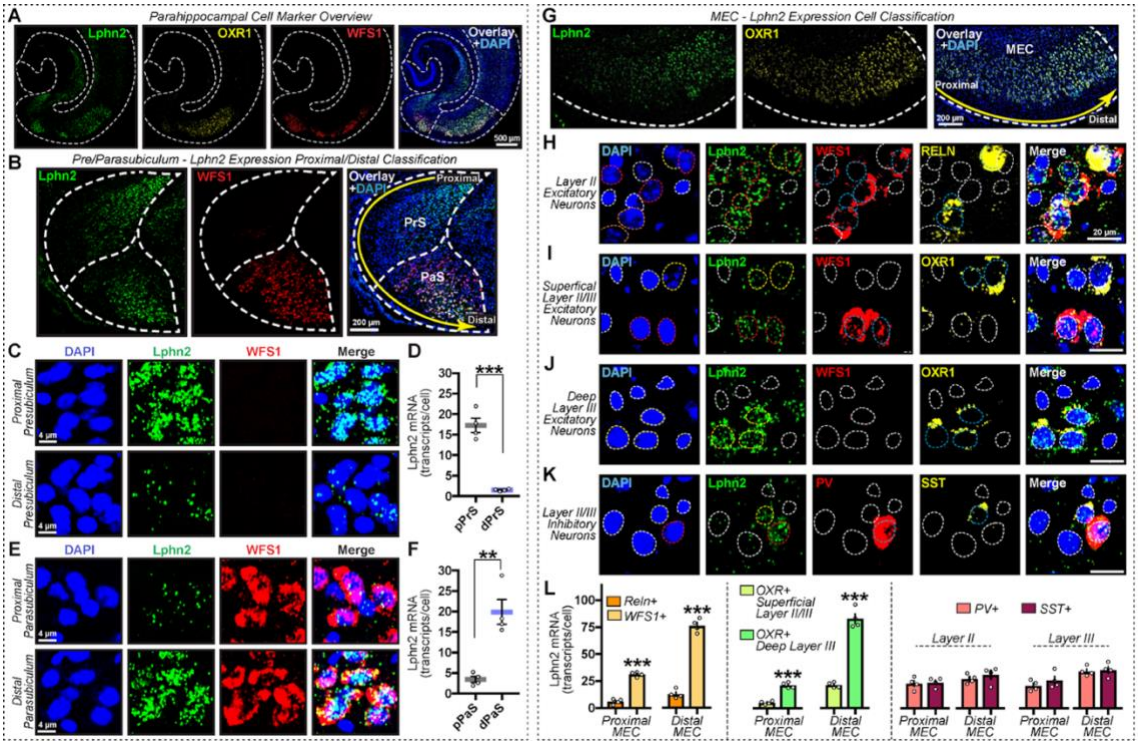

Figure 4. Parahippocampal Latrophilin-2 expression is topographical and cell type specific. **(A)** Representative confocal image of a hippocampal-parahippocampal P30 mouse horizontal section (-2.6mm ventral) after single molecule RNA *in situ* hybridization for Lphn2 (green), Oxr1 (yellow), and Wfs1 (red), along with DAPI (blue) to label nuclei. **(B)** Magnified confocal image of presubiculum (PrS) and parasubiculum (PaS) labelled for Lphn2 and Wfs1, with region boundaries outlined by Wfs1 expression present in the PaS but not PrS. **(C)** Representative magnified cellular images of proximal and distal PrS (pPrS and dPrS) subregions and **(D)** summary graphs (n=4 mice). **(E-F)** Similar as described for C-D, except for proximal and distal PaS (pPaS and dPaS) subregions. **(G)** Representative magnified MEC confocal image, marked by Oxr1 specific expression. **(H-K)** Representative magnified cellular images of distinct neuronal classes from distal MEC region including **(H)** Layer II pyramidal (Wfs1) and stellate (RELN) excitatory neurons, **(I)** Layer III superficial pyramidal excitatory neurons (Oxr1) excitatory neurons, **(J)** Deep layer III pyramidal excitatory neurons (Oxr1), **(K)** Inhibitory parvalbumin expressing (PV) and somatostatin expressing (SST) interneurons. **(L)** Lphn2 expression level summary graphs of proximal/distal MEC regions for: Reln+ or Wfs1+ layer II MEC neurons *(left)*, superficial versus deep Oxr1+ MEC neurons *(middle)*, and PV+ versus SST+ cells within superficial layers II and III *(right)*. (n=4 mice). Data shown are means ± SEM; Statistical analysis was performed by Student's t-test (**=P<.01, ***=P<.001).

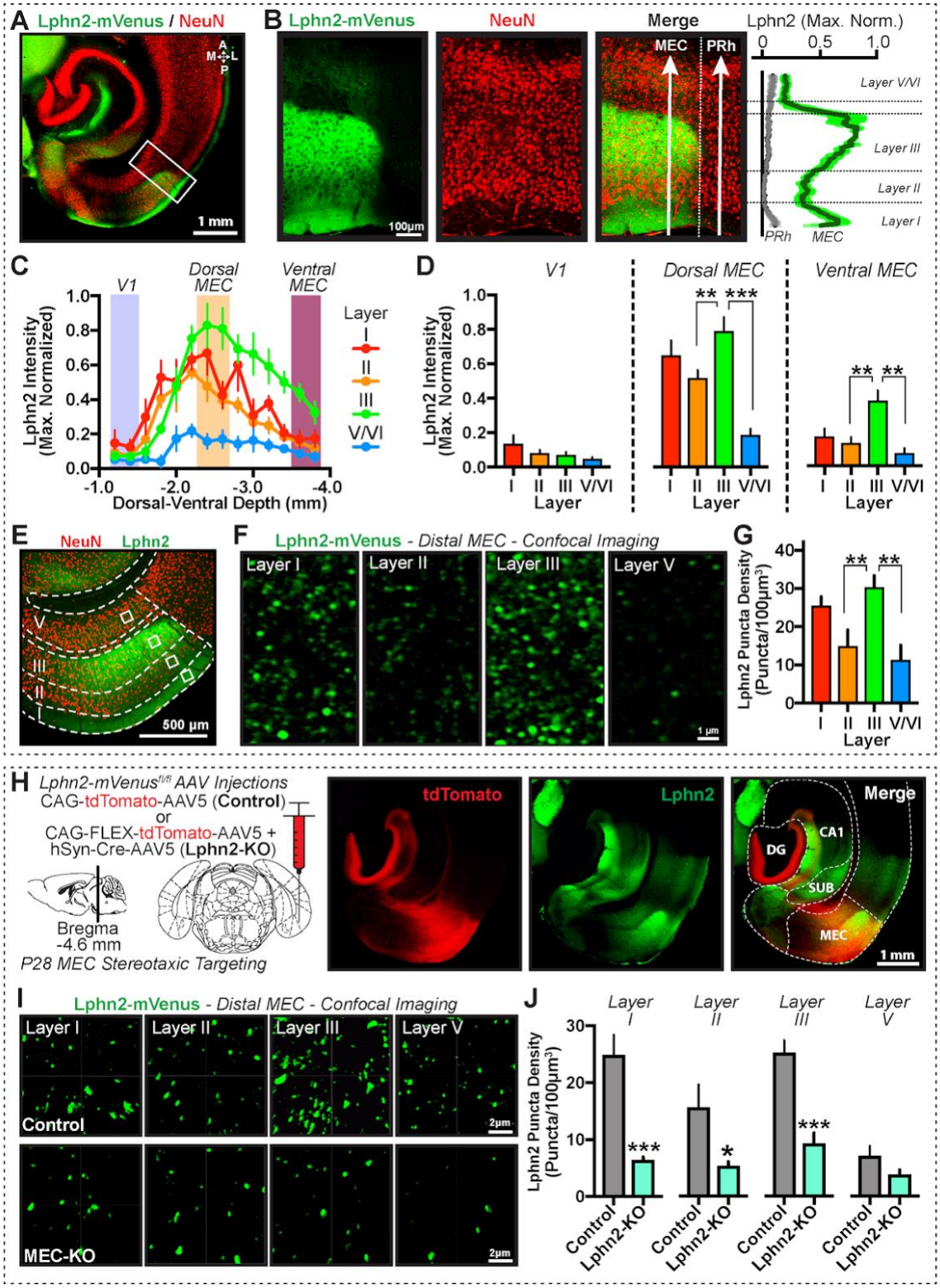
A Lphn2-mVenus / NeuN
1 mm
B Lphn2-mVenus
NeuN
Merge
MEC
PRh
100µm
Lphn2 (Max. Norm.)
0
0.5
1.0
Layer V/VI
Layer III
Layer II
Layer I
PRh
MEC
C
V1
Dorsal MEC
Ventral MEC
Lphn2 Intensity (Max. Normalized)
Dorsal-Ventral Depth (mm)
Layer
I
II
III
V/VI
D
V1
Dorsal MEC
Ventral MEC
Lphn2 Intensity (Max. Normalized)
Layer
E
NeuN Lphn2
500 µm
F
Lphn2-mVenus - Distal MEC - Confocal Imaging
Layer I
Layer II
Layer III
Layer V
1 µm
G
Lphn2 Puncta Density (Puncta/100µm³)
Layer
H
Lphn2-mVenusfl/fl AAV Injections
CAG-tdTomato-AAV5 (Control)
or
CAG-FLEX-tdTomato-AAV5 +
hSyn-Cre-AAV5 (Lphn2-KO)
Bregma
-4.6 mm
P28 MEC Stereotaxic Targeting
tdTomato
Lphn2
Merge
DG
CA1
SUB
MEC
1 mm
I
Lphn2-mVenus - Distal MEC - Confocal Imaging
Layer I
Layer II
Layer III
Layer V
Control
MEC-KO
2µm
J
Layer I
Layer II
Layer III
Layer V
Lphn2 Puncta Density (Puncta/100µm³)
Control
Lphn2-KO

Figure 5. Lphn2 protein is enriched in superficial layers of the medial entorhinal cortex (MEC) and dependent on local genetic expression. (A) Representative image of horizontal section (~2.6 mm ventral) with peak Lphn2 signal in the dorsal MEC immunostained for NeuN and Lphn2-mVenus. **(B)** *Left,* Magnified image of MEC and perirhinal cortex (PRh) border with Lphn2 layer specific localization in the MEC but not in the adjacent PRh. *Right*, line scan intensity measurements across MEC and PRh layers. **(C-D)** Normalized Lphn2 fluorescence intensity across the ventral axis for each cortical layer **(C)**, and summary graphs of average Lphn2 intensity **(D)** of dorsal, intermediate and ventral sections (V1, dorsal MEC, and ventral MEC positions, respectively) (n=5 mice; 2 sections/region). **(E-G)** Confocal overview image of MEC with white boxes indicating regions used for imaging Lphn2 puncta in each layer **(E)**, representative high-power Lphn2 puncta images for each cortical layer across the distal MEC **(F)**, and summary graphs of Lphn2 puncta density by layer **(G)**; n=5 mice. **(H-J) MEC targeted conditional Lphn2 deletion leads to loss of distal MEC Lphn2 protein**. **(H)** *Left,* AAV experimental schematic targeting the MEC (P30) with AAVs expressing either tdTomato (Control) or AAV cocktail of hSyn-CRE and FLEX-tdTomato to achieve MEC localized Lphn2 genetic knock-out animals (MEC-KO). *Middle,* representative images of control and Lphn2 MEC-KO animals, analyzed at P45. *Right,* line scan intensity measurements across distal MEC for control and Lphn2 MEC-KO animals **(I)** Representative high-power Lphn2 puncta confocal images for each cortical layer across the distal MEC for control and Lphn2 MEC-KO and **(J)** puncta density summary graphs (n=5 mice) Data shown are means ± SEM; Statistical analysis was performed by Student's t-test (J) or one-way ANOVA with Tukey's post-hoc test for multiple comparisons (D/G) (*=P<0.05, **=P<.01, ***=P<.001).

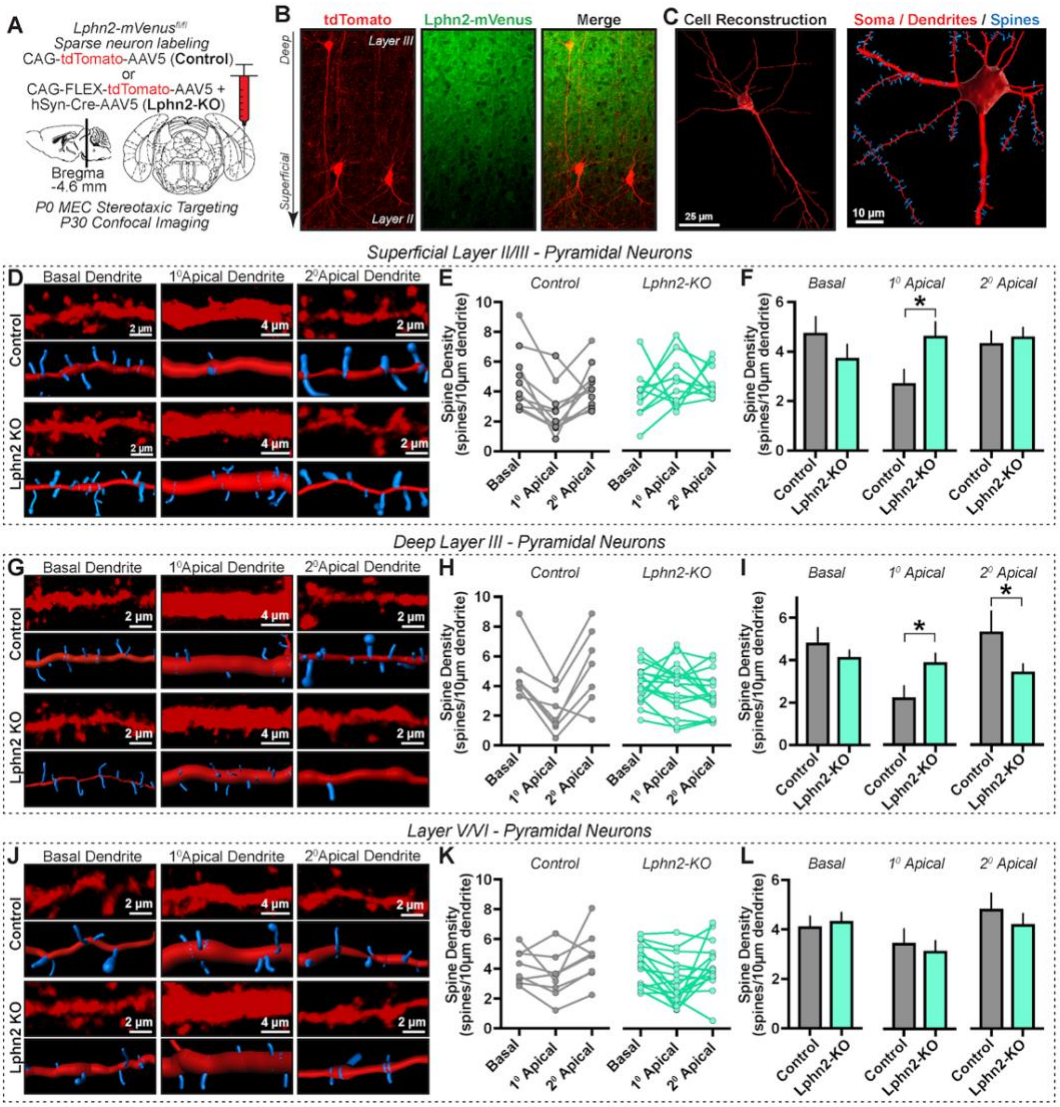

Figure 6. Latrophilin-2 deletion in MEC pyramidal neurons leads to cell-specific and dendrite-specific spine density alterations. (A) AAV viral experimental schematic. MEC was stereotactically targeted in P0 mice with AAVs expressing tdTomato (control) versus a cocktail of Cre + FLEX-tdTomato expressing AAVs (Lphn2-KO) to achieve sparsely tdTomato labelled neurons for visualization. Neurons in the distal MEC were confocal imaged after maturation (P30). **(B)** Representative confocal image of sparsely labelled superficial MEC neurons in deep layer III and superficial layer II regions. **(C)** Representative reconstructions of pyramidal neurons with dendrites (red) analyzed for spine (blue) protrusions. **(D)** Representative confocal images and digital reconstructions of dendrites (red) and spines (blue) on superficial layer III MEC pyramidal neurons from control (*top*) and Lphn2-KO neurons (*bottom*). Shown are basal dendrites (left), primary apical dendrites (middle), and secondary apical dendrites (right). **(E)** Single cell spine densities in defined dendritic compartments of individual pyramidal neurons and **(F)** summary graphs; (control= 10 neurons, Lphn2-KO= 10 neurons; 3 littermate paired animals). **(G-I)** Similar as described in D-F, except for deep layer III MEC neurons. (control= 7 neurons, Lphn2-KO= 18 neurons; 3 littermate paired animals) **(J-L)** Similar as described in D-F, except for layer V/VI MEC neurons. (control= 8 neurons, Lphn2-KO= 16 neurons; 3 littermate paired animals). Data shown are means ± SEM; Statistical analysis was performed by Student's t-test (*=P<.05).

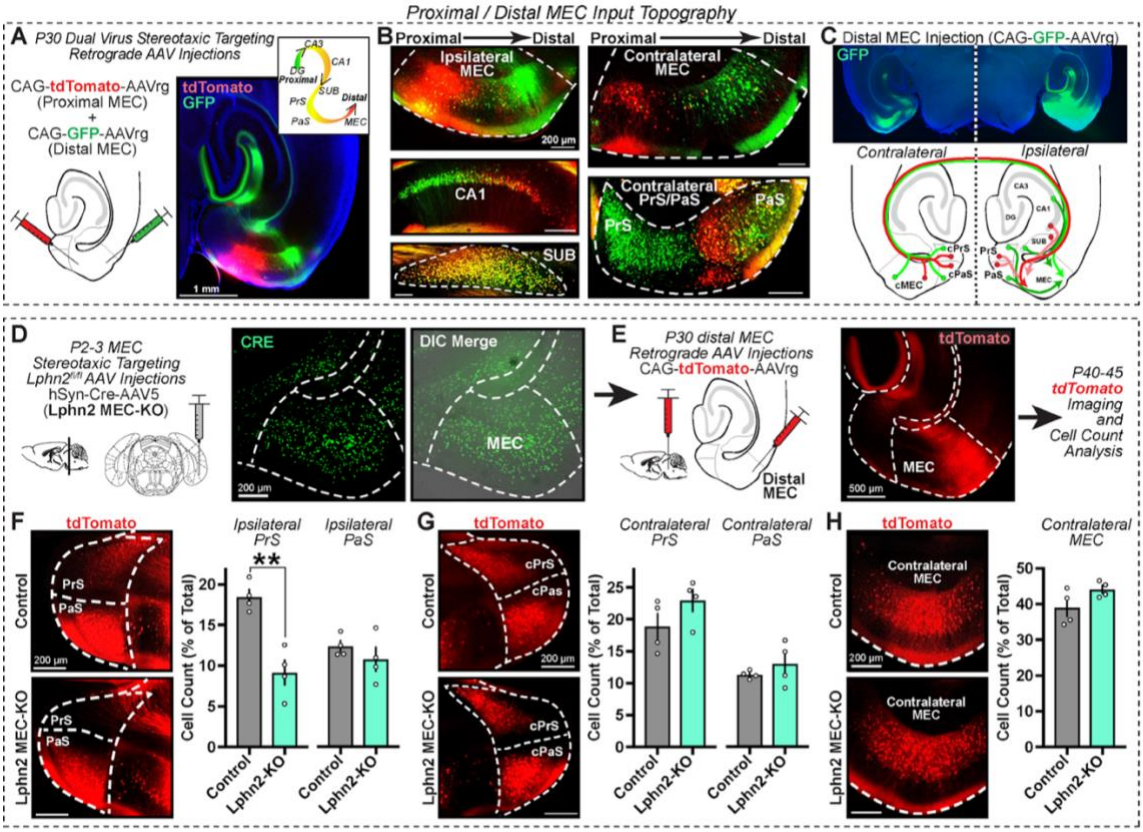

Figure 7. Latrophilin-2 controls input specific MEC connectivity. (A-C) Proximal versus distal MEC exhibits differential input connectivity patterning. **(A)** Left, Experimental design of dual stereotactic delivery of retrograde AAVs targeting proximal MEC (CAG-tdTomato-AAVrg) and distal MEC (CAG-GFP-AAVrg). Right, representative confocal image showing MEC injection localization, with inset schematic illustrating the proximal to distal axis (relative to DG) **(B)** Representative confocal images of infected neurons in the ipsilateral MEC (injection site), alongside examples of retrogradely labeled neurons that project to the MEC: ipsilateral hippocampal CA1 and subiculum (SUB), contralateral MEC and PrS/PaS. **(C)** Top, representative image of retrograde GFP-AAVrg labeling of ipsilateral and contralateral regions. Bottom, topographical circuit diagram of proximal (red) versus distal (green) MEC inputs. **(D-H)** Lphn2 MEC deletion leads to selective impairment of ipsilateral PrS to distal MEC connectivity. **(D)** *Left,* experimental design. MEC was stereotactically targeted on one hemisphere with hSyn-CRE-AAV5 viral injections in P3 mice; *Right,* representative image of Cre immunolabeling in the MEC to confirm targeted infectivity. **(E)** *Left,* At P35 distal MEC was targeted with retrograde AAV expressing tdTomato (CAG-tdTomato-AAVrg) on the same hemisphere as P3 Cre injections. *Right,* After confirming MEC targeting, imaging and cell-counting was performed at P45 for major input regions. **(F-H)** *Left,* Representative images of retrogradely labelled neurons and *Right,* Summary graphs - percentage of total retrograde neuron population that resides in the indicated regions of **(F)** ipsilateral presubiculum (PrS) and parasubiculum (PaS), **(G)** contralateral PrS/PaS, and **(H)** contralateral MEC. (n=4 mice; 4 sections/mouse). Data shown are means ± SEM. Statistical analysis was performed by Student's t-test (**=P<.01).

Supplementary Figures and Title Legends.

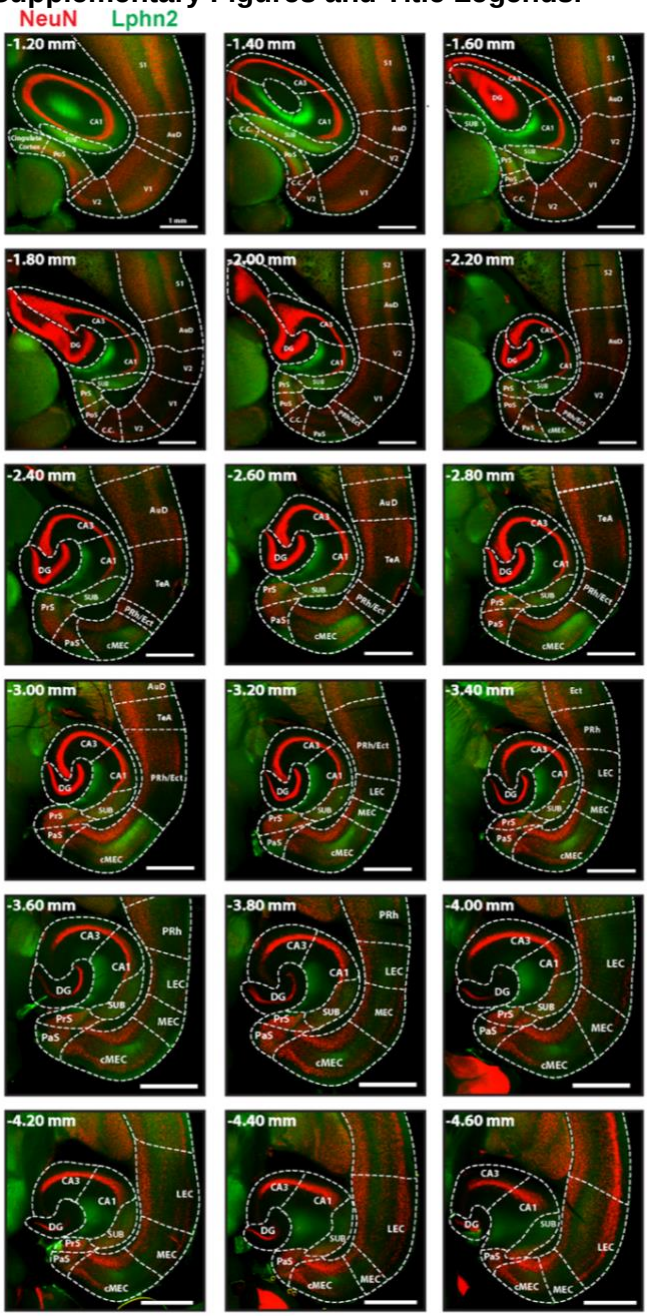

Figure S1 (supplemental to Figure 1). Lphn2 protein localization in hippocampal-parahippocampal regions. Representative images of serial horizontal sections spanning the dorsal to ventral axis, (-1.2mm to -4.6mm from bregma in 0.2mm increments) stained for neuronal marker NeuN (to label neuronal nuclei) and GFP (to label Lphn2-mVenus). Mapping abbreviations: dentate gyrus (DG); subiculum (SUB); Prosubiculum (PoS); Presubiculum (PrS); Parasubiculum (PaS); Caudomedial entorhinal cortex (cMEC); Medial Entorhinal Cortex (MEC); Perirhinal cortex (PRh); Ectorhinal cortex (Ect); Temporal association cortex (TeA); lateral entorhinal cortex (LEC); Auditory cortex (AuD); primary visual cortex (V1); secondary visual cortex (V2); primary somatosensory cortex (S1); cingulate cortex (CC).

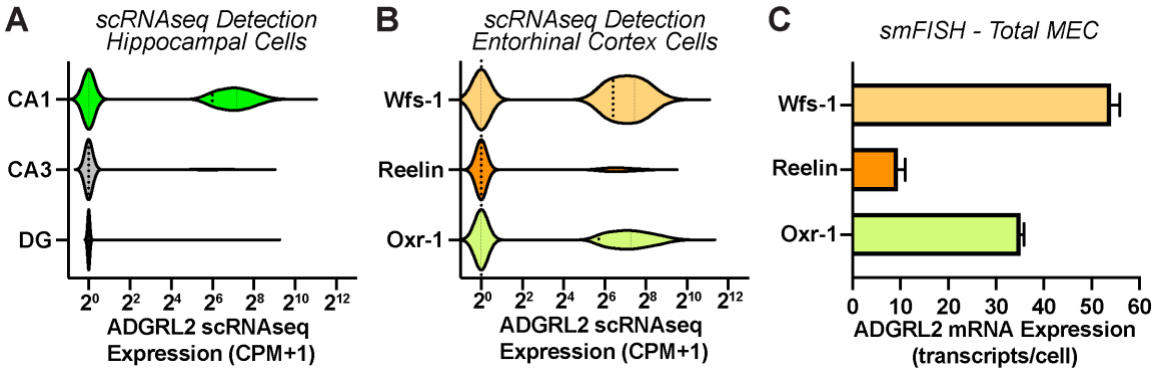

Figure S3 (supplemental to Figure 4). scRNAseq *ADGRL2* gene counts validate cell-type specific expression levels. (A-B) *ADGRL2* gene expression level comparisons of scRNAseq databases for hippocampal and EC cells. Using scRNAseq data generated by the Allen Institute, we compared *ADGRL2* gene counts between different cell types in both the hippocampus **(A)** and the EC **(B)**. Hippocampal cells were defined by the Allen Institute categorizations provided for each individual cell (n = 58566 DG cells, 1899 CA3 cells, 13221 CA1 cells). EC cells were classified to specific cell-types based on the expression of *Wfs-1* (layer II pyramidal), *Reelin* (layer II stellate) and *Oxr-1* (layer III pyramidal) (n = 1314 *Wfs-1* cells, 7592 *Oxr-1* cells, 3471 *Reelin* cells) **(C)** Whole MEC *ADGRL2* transcript counts detected by single molecule RNA fluorescent *in situ* hybridization (n = 4 animals). Cells were classified based on detection with *Wfs1, Reelin,* and *Oxr1* probes, as described in Figure 4. Statistical analysis was performed using one-way ANOVA with post-hoc Tukey's test for multiple comparisons (P<.001 for comparisons: (A) CA1 vs. DG, CA1 vs. CA3 (B-C) *Wfs-1* vs. *Reelin*, *Oxr-1* vs. *Reelin*).

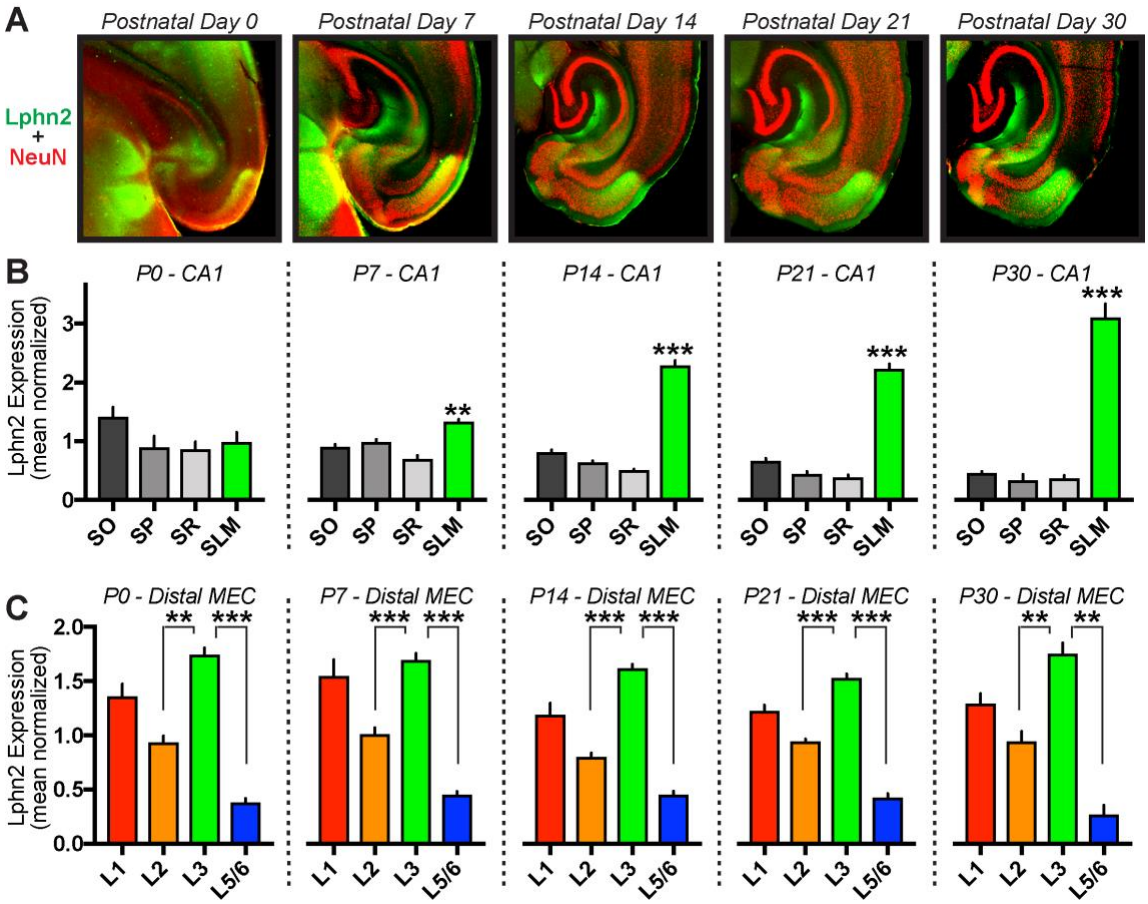

Figure S4 (supplemental to Figure 5). Latrophilin-2 hippocampal and MEC localization during circuit development. (A) Representative horizontal section (with peak MEC expression present) from Lphn2-mVenus mice at postnatal days 0, 7, 14, 21, and 30, immunolabeled for neuronal nuclei (NeuN) and GFP (Lphn2-mVenus). **(B)** Summary graphs of Lphn2-mVenus fluorescent intensities within stratum oriens (SO), stratum pyramidal (SP), stratum radiatum (SR), and stratum lacunosum-moleculare (SLM) of hippocampal CA1 across development. **(C)** Summary graphs of Lphn2-mVenus fluorescent intensities across development within each layers (I, II, III, V/VI) of the distal MEC. Data shown are means ± SEM; (n = P0 (4 mice), P7 (2 mice), P14 (4 mice), P21 (4 mice), P30 (4mice); 2 sections / mouse brain). Statistical analysis was performed using one-way ANOVA with post-hoc Tukey's test for multiple comparisons (**=P<0.01; ***=P<.001).

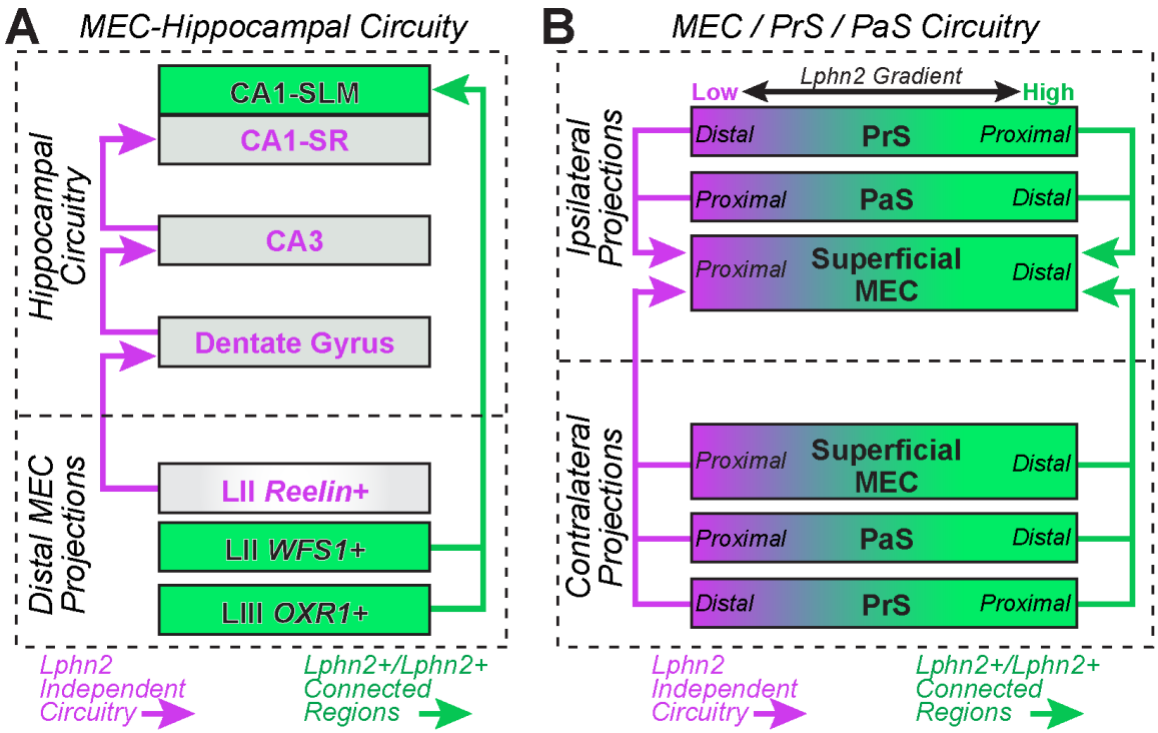

Figure S5. Circuit model of interconnected Lphn2 expressing regions in hippocampal & parahippocampal networks. (A) Circuit model between the medial entorhinal cortex (MEC) and hippocampal regions of the dentate gyrus (DG), CA3, and CA1 subregions of the stratum radiatum (CA1-SR) and stratum lacunosum-moleculare (CA1-SLM). Cell types indicated in purple are Lphn2 deficient connected pathways, including Reelin+ layer II MEC neurons that connect with DG hippocampal neurons. Cell types indicated in green are Lphn2 enriched connected pathways, including Wfs-1 expressing layer II and Oxr-1 expressing layer III pyramidal neurons that project to the CA1-SLM. (B) Circuit diagrams for interconnected parahippocampal regions. Lphn2 deficient connected pathways shown in purple include proximal MEC subregions that receive local inputs from the ipsilateral distal PrS and proximal PaS; Long-range contralateral inputs originate from distal PrS, proximal PaS, and proximal MEC. Conversely, Lphn2 enriched regions indicated in green include distal MEC and its inputs arising from ipsilateral proximal PrS and distal PaS; Long-range contralateral inputs originating from proximal PrS, distal PaS, and distal MEC.

STAR Methods.

Key Resource Table

REAGENT or RESOURCE	SOURCE	IDENTIFIER
Antibodies		
Mouse monoclonal anti-NeuN	Millipore	MAB377
Rabbit polyclonal anti-GFP	Invitrogen	A-11122
Rabbit polyclonal anti-Cre	Cell-Signaling Technology	15036S
Goat anti-rabbit Alexa 405	Thermo Fisher Scientific	A31556
Goat anti-rabbit Alexa 488+	Thermo Fisher Scientific	A32731
Goat anti-mouse Alexa 555+	Thermo Fisher Scientific	A32427
Virus strains		
CAG-tdTomato-AAV5	University of North Carolina Vector Core	AAV-CAG-tdTomoato (Dr. Edward Boyden)
CAG-FLEX-tdTomato-AAV5	University of North Carolina Vector Core	AAV-CAG-FLEX-tdTomato (Dr. Edward Boyden)
CAG-GFP-AAVrg	Addgene	37825-AAVrg (Dr. Edward Boyden)
CAG-tdTomato-AAVrg	Addgene	59462-AAVrg (Dr. Edward Boyden)
hSyn-CRE-AAV5	Addgene	105553-AAV5 (Dr. James Wilson)
smFISH probes		
Mm-Lphn2-C1	ACDBio	319341
Mm-Rbfox3-C2	ACDBio	313311
Mm-Wfs1-C2	ACDBio	500871
Mm-Reln-C3	ACDBio	405981
Mm-Oxr1-C3	ACDBio	509211
Mm-Pvalb-C2	ACDBio	421931
Mm-Sst-C3	ACDBio	404631
RNAscope (+) Control Probe	ACDBio	320881
RNAscope (-) Control Probe	ACDBio	320871
smFISH fluorophores		
Opal 540	Akoya Biosciences	FP1494001KT
Opal 620	Akoya Biosciences	FP1495001KT
Opal 690	Akoya Biosciences	FP1497001KT
Transgenic mice lines		
Lphn2-mVenus$^{fl/fl}$	Anderson et al. 2017	JAX: 023401
Lphn2$^{fl/fl}$	Anderson et al. 2017	JAX: 023401
Analyzed Datasets		
scRNAseq data	Tasic et al., 2018	GEO: GSE115746
Software and algorithms		
ImageJ	NIH	https://imagej.nih.gov/ij/

Imaris	Oxford Instruments	https://imaris.oxinst.com/
Zen Black	Zeiss	https://www.zeiss.com/microscopy/us/products/microscope-software/zen.html
Prism 7	Graphpad	https://www.graphpad.com/
R	The R Foundation	https://www.r-project.org/
Python 3.7	Python.org	https://www.python.org/downloads/
Dplyr	Tidyverse.org	https://dplyr.tidyverse.org/
Other		
High Precision Microscopy slides	Thorlabs	MS10UW
HistoBond+M slides	VWR	16004-406
Precision slide covers	Thorlabs	CG15KH1

RESOURCE AVAILABILITY.

Lead Contact. Further information and requests for resources and reagents should be directed to and will be fulfilled by the lead contact, Garret R. Anderson (garret.anderson@ucr.edu).

Materials availability. This study did not generate new unique reagents.

Data and code availability. All relevant data presented in this study are available from the lead contact upon request. Scripts used to reanalyze RNAseq data (Tasic et al., 2018) are available from the lead contact upon request.

Experimental Model Details.

Animals. Lphn2-mVenus$^{fl/fl}$ and Lphn2$^{fl/fl}$ mice used in this study were described previously (Anderson et al., 2017). The original mouse line for generation of these lines is available

through Jackson Laboratory Mouse Repository for distribution (B6;129S6-Adgrl2tm/sud/J, JAX Stock number: 023401). Mice were weaned at 21 days of age and housed in groups of 2 to 5 on a 12-hour light/dark cycle with food and water ad libidum in the University of California, Riverside Animal Housing Facility. All procedures conformed to National Institutes of Health Guidelines for the Care and Use of Laboratory Mice and were approved by the University of California, Riverside Administrative Panel on Laboratory Animal Care, and Administrative Panel of Biosafety. Male and female mice were used for all experiments in approximately equal proportions, in gender-matched littermate pairs. No obvious differences were noted due to gender.

Method Details.

Stereotaxic Viral Targeting.

For adult mice (P30-35), surgeries were performed with isoflurane anesthesia. Neonatal mice (P0-3) surgeries were performed with 5-minute ice anesthesia. Using a dual manipulator stereotaxic frame (Kopf), stereotaxic coordinates used were: Anterior/Posterior (AP) in relation to Lambda; Medial/Lateral (ML) in relation to midline; and Dorsal-Ventral (DV) in relation to dorsal brain surface. Coordinates used include: Adult Medial Entorhinal Cortex targeting (fig. 5H): AP +0.9 mm, ML +3.2 mm, DV −3.0 mm. Adult Proximal MEC targeting (Fig. 7A). Proximal MEC: AP +0.8 mm, ML: +2.6 mm, DV −2.4 mm. Adult Distal MEC targeting (Fig. 7A): AP +0.9 mm, ML +3.5 mm, DV −2.4 mm. Neonatal P0-3 MEC targeting (Figure 6A: AP +0.2 mm; ML +2.1 mm; and DV −2.0

mm. Concentrated adeno-associated viruses (AAVs) were injected (0.5 µl) with a glass pipet tip with controlled rate (0.15 µl/min) using an infusion pump (Harvard Apparatus).

Viruses.

Adeno-associated viruses (AAVs) were produced from plasmids courtesy of Edward Boyden (pAAV-CAG-GFP; pAAV-CAG-tdTomato; pAAV-CAG-FLEX-tdTomato) and James M. Wilson (pENN.AAV.hSyn.Cre.WPRE.hGH). Viral preps were produced and titered (viral genome copies per milliliter – vg/ml) by University of North Carolina Vector Core (CAG-tdTomato-AAV5, 4.3x10^9 vg/ml; CAG-FLEX-tdTomato-AAV5, 3.9 x10^9 vg/ml) or Addgene (CAG-GFP-AAVrg, # 37825-AAVrg, 7x10^12 vg/ml; CAG-tdTomato-AAVrg, Addgene viral prep # 59462-AAVrg, 7x10^12 vg/ml; hSyn-CRE-AAV5, Addgene viral prep # 105553-AAV5, 1x10^13 vg/ml).

Immunohistochemistry (IHC).

Mice were anesthetized and perfused transcardially with 20 mL phosphate buffered saline (PBS; 137mM NaCl, 2.7mM KCl, 10mM Na_2HPO_4, 1.8mM KH_2PO_4, pH 7.4) and 10 mL freshly prepared 4% paraformaldehyde (PFA) in PBS. Brains were dissected and postfixed in 4% PFA in PBS overnight at 4°C. Brains were briefly rinsed in PBS, mounted in agarose and 100 µm horizontal serial sections were collected using a Vibratome VT100S (Leica Biosystems). For immunofluorescence staining, sections were then washed in PBS for 5 min under gentle agitation followed by incubation for 1 hour in a blocking solution containing 10% goat serum (ab7481; Abcam) and 0.5% Triton X-100 in PBS. Subsequently, sections were transferred into PBS containing 1% goat serum, 0.01% Triton X-100, primary antibody, and incubated overnight at 4°C on a nutating mixer.

Sections were washed three times with PBS for 5 min each, then incubated in a solution of 1% goat serum, 0.01% Triton X-100, and secondary antibodies for 4 hours at room temperature. Sections were washed again three times in PBS for 5 min each, and mounted on microscope slides (MS10UW; Thorlabs) using Vectashield Plus Antifade mounting media (Vector Laboratories; H-1000-10).

Antibodies.

For immunohistochemistry experiments, the following primary antibodies were used: NeuN (1:1000; mouse monoclonal; MAB377; Millipore), GFP (1:1000; rabbit polyclonal; A-11122; Invitrogen), Cre Recombinase (1:400; rabbit polyclonal; 15036S; Cell Signaling Technology). The following secondary polyclonal antibodies with fluorophores were used: goat anti-rabbit Alexa 405 (1:500 A31556; Thermo Fisher Scientific), goat anti-rabbit Alexa-Plus 488 (1:1000 A32731; Thermo Fisher Scientific), goat anti-mouse Alexa-Plus 555 (A32427; Thermo Fisher Scientific).

IHC serial section imaging.

For each brain, horizontal sections 100 µm thick were prepared as above, and sixteen sections (every other section, spanning 1.4 mm to 4.6 mm ventral to bregma) were stained for GFP (Lphn2-mVenus) and NeuN. Sections were then imaged using a Zeiss Axio Imager M2 fluorescence microscope and 2.5x air lens. Acquisition settings were optimized and held constant for each imaged brain. Images from P30 animals were aligned and overlaid with a horizontal map to determine region boundaries (Paxinos and Franklin, 2012). Fluorescence intensity was subsequently analyzed in ImageJ software (https://imagej.nih.gov). For proximal-distal parahippocampal region fluorescence

intensity measurements, a given parahippocampal region would be divided into three equal segments, with the segment closest to hippocampus defined as proximal and the furthest defined as distal. Fluorescence intensity in these regions was then measured using the square region of interest (ROI) tool in ImageJ. For layer-specific fluorescence intensity measurements,100-pixel wide line ROIs were drawn across cortical layers for each region, perpendicular to the cortical surface. MEC layers were defined as follows: Layer I: Absent of consistent NeuN labelled cells. Layer II/III: Neuron rich layers with prominent NeuN signal; First one-third defined as layer II, remaining two-thirds defined as layer III. Layer IV: NeuN-negative region separating LII/III from deeper NeuN-positive layers. Layer V/VI - Remaining NeuN-positive area before the hippocampal commissure. Background fluorescence intensity was measured for each slice and subtracted from raw intensity measurements and resulting fluorescence measurements were normalized either to slice max or mean fluorescence intensity as indicated.

IHC synapse confocal imaging and analysis.

Confocal imaging was performed using a Zeiss 880 Confocal microscope with Airyscan detection array. For Lphn2 puncta analysis, imaging was performed by acquiring Z-stacks in each layer of distal MEC. Stacks were captured using a Plan Apochromat 40x/1.4 DIC M27 oil objective and 488 nm laser with a BP 420-480 + BP 495-550 emission filter, scanned at 3.36 µs/pixel at 2x digital zoom. All images were acquired in airy fast “optimal” mode (Nyquist sampling) and post-processed in Zen Black software, for a final X-Y resolution of 0.146 µm/px. Laser power and digital gain were optimized each experimental day and held constant throughout the imaging session for each matched pair. Each stack was 5 µm thick (0.185 µm/slice), beginning 5 µm beneath the tissue

surface, and centered on the region of peak Lphn2 expression within the layer. Acquired image stacks were subsequently imported into Imaris 9.6 software (Oxford Instruments) for 3D reconstruction and analysis. Each stack was pre-processed using the “Subtract background” (default radius) and “Normalize Layers” operations to enhance signal-to-noise ratio (SNR) and compensate for laser attenuation deeper in the stack. Lphn2 puncta were reconstructed semi-automatically by using the “Spots” creation wizard to detect puncta of variable size with a typical diameter of 0.3 µm in X/Y and 0.6 µm in Z (as determined by preliminary measurements of Lphn2 puncta size). Detected spots were filtered using the auto-calculated “quality” filter threshold. Spot diameters were determined by automatic threshold calculation from absolute intensity histograms, and reconstructed based on minimum distance to puncta borders.

Single molecule RNA fluorescent in-situ hybridization (smFISH).

P10 or P30 wild type mice were anesthetized with isoflurane and transcardially perfused with 20 mL ice-cold 1% diethyl pyrocarbonate (DEPC) treated and autoclaved PBS, followed by 10 mL 1% DEPC treated and autoclaved PBS with 4% PFA. Brains were placed into a sterile solution of 4% PFA in PBS for 24 hours, followed by 10% sucrose in PBS overnight at 4º C. Brains were subsequently cryoprotected by immersion in sterile 20% sucrose in PBS (until no longer floating), then into sterile 30% sucrose in PBS for 2-3 days. Brains were then stored at -80º C until cryosectioning. Brains were cryo-sectioned at 15 µm thickness and adhered to HistoBond+M adhesive microscope slides (VWR 16004-406). After sectioning, tissue *in situ* hybridization was performed using RNAscope Multiplex Fluorescent RNA probes (Advanced Cell Diagnostics). Tissue was mounted using Vectashield Plus Antifade mounting media with DAPI (Vector Laboratories; H-2000-

10) and Precision Cover Glass Slips (Thorlabs; CG15KH1). For single molecule *in-situ* hybridization, probes used include: Latrophilin-2 (Mm-Lphn2, 319341; ACDBio), NeuN (Mm-Rbfox3-C2; 313311; ACDBio), Wolfram syndrome 1 (Mm-Wfs1-C2, 500871; ACDBio), Reelin (Mm-Reln-C3, 405981; ACDBio), Oxidation resistance 1 (Mm-Oxr1-C3, 509211; ACDBio), Parvalbumin (Mm-Pvalb-C2, 421931; ACDBion) and Somatostatin (Mm-Sst-C3, 404631; ACDBio). RNAscope® 3-plex Positive Control Probe (Polr2a-C1, PPIB-C2, 320881; ACDBio) was compared with RNAscope® 3-plex Negative Control Probe (DapB-C1/C2, 320871; ACDBio) to assess probe specificity. Akoya fluorophores used for hybridization include Opal 540 (C1 channel [Lphn2], FP1494001KT; Akoya Biosciences), Opal 620 (C2 channel [NeuN, WFS1, PV], FP1495001KT; Akoya Biosciences) and Opal 690 (C3 channel [RELN, OXR1, SST], P1497001KT; Akoya Biosciences). Imaging was performed on a Zeiss 880 confocal microscope with airyscan using a Plan Apochromat 10x/0.45 M27 air objective scanning in airy fast “Flex” mode (0.7x Nyquist) at 2.17 µs/pixel. DAPI was captured using a 405 nm laser and BP 420-480 + BP 495-550 emission filter with BP 420-460 + LP 500 secondary beam splitter. Lphn2 probes were hybridized to Opal 540 and captured using a 488 nm laser with BP 420-480 + BP 495-550 emission filter and LP 525 secondary beam splitter. NeuN, WFS1 and parvalbumin probes were hybridized to Opal 620 and captured using a 561 nm laser with BP 420-480 + BP 495-620 emission filter and LP 570 secondary beam splitter. OXR1, Reelin and SST probes were hybridized to Opal 690 and captured using a 633 nm laser with BP 570-620 + LP 645 emission filter and LP 660 secondary beam splitter. Cell nuclei were stained with DAPI and imaged using a 405 nm laser with BP 420-480 + BP 495-550 emission filter and BP 420-460 + LP 500 secondary beam splitter. Images were analyzed using ImageJ (https://imagej.nih.gov). Neuron subtypes were identified as DAPI+ nuclei

unambiguously collocated with a single cell-type specific marker, and Lphn2 puncta within each cell group were quantified manually using the multipoint tool.

Sparse fluorescent labeled neuron confocal imaging, reconstruction, and analysis.

Three pairs of mice were injected neonatally with MEC-targeted viruses, each pair consisting of one Lphn2 knockout (hSyn-CRE-AAV5 + CAG-FLEX-tdTomato-AAV5) and one control (CAG-tdTomato-AAV5), and perfused/sectioned at P30 as described above. AAVs were diluted 1:100 from stock concentrations. Prior to staining, to confirm accurate MEC targeting and adequate tdTomato infectivity, sections were briefly examined under a fluorescent microscope. Six sections (2.4 to 3.1 mm ventral to bregma) from each animal were selected, immunostained for Lphn2 and viewed under fluorescence. From these sections, 3 per animal were chosen for high-power imaging, with littermate sections matched based on similar peak MEC Lphn2 enrichment. Confocal imaging was performed on these sections with a Zeiss 880 microscope with airyscan in airy fast “optimal” mode, using a 561 nm laser with BP 570-620 + LP 645 emission filter and SP 615 secondary beam splitter. To determine which neurons might be suitable for imaging, an initial reference image of the MEC was captured using a Plan Apochromat 10x/0.45 M27 air objective at 0.5x digital zoom. Neurons along the distal edge of the MEC (where Lphn2 signal is strongest) were subsequently chosen for high-power imaging, using a Plan Apochromat 40x oil objective at 1-1.5x digital zoom and 2.35 µs/pixel scan speed, with laser intensity/gain optimized and held constant within each matched pair of mice. Z-stacks starting >5 µm into the tissue and extending 30-40 µm deep (0.185 µm slice interval) were acquired to capture neurons and their local processes, with each stack focused around 1-2 neuronal cell bodies to ensure a high likelihood of imaging many

complex dendrites. Layer II/III boundary neurons were defined as any neurons whose somata were within one imaging frame (approx. 300 μm, or 5-6 cell bodies) of layer I. Layer III neurons were defined as being deep in the highly enriched Lphn2 zone, whereas layer V neurons were directly adjacent to the peak Lphn2 enrichment zone at the layer III/IV transition.

Similar to Lphn2 puncta analysis, neuronal image stacks were imported into Imaris and pre-processed using the "Subtract background" and "Normalize layers" tools. After processing, one or more neurons per image were selected for reconstruction. The soma was reconstructed using the Surface creation wizard. Surface creation was limited to a 3-D region of interest around the soma, and any neurites included in the reconstruction manually cut and deleted. "Surface detail" was optimized per image to account for variations in signal intensity and image quality. Axons, dendrites, and spines were then reconstructed semi-automatically using the filament creation wizard and "autopath" tool. Layer II/III neurons were classified into two subgroups, Pyramidal and Stellate. Stellate Neurons were defined as having a star-like appearance with a multitude of processes emanating in all directions, whereas Pyramidal neurons had smaller somata with one large apical dendrite extending towards superficial layers. Notably, layer II pyramidal neurons are the most superficial cells and have highly branched structure distinct from layer III superficial pyramidal neurons. Layer III/V neurons were defined as pyramidal if they contained a large apical shaft extending through more superficial MEC layers. Pyramidal neuron spine density was compared for the whole cell in addition to individual comparisons for the primary apical shaft, secondary apical shaft and basal dendrites. Spine density comparisons between control and KO groups for each MEC layer for each dendritic region were calculated by dividing the number of spines by length of dendritic shaft.

Retrograde AAV cell labeling and confocal imaging.

Mice were stereotactically injected with retrograde AAVs (AAVrg) targeting distal or proximal MEC at P35 and perfused at P45. Horizontal sections (100 µm thick) were prepared as above, and imaged on a Zeiss 880 microscope with airyscan, using a Plan Apochromat 10x/0.45 M27 air objective in airy fast mode. GFP and tdTomato viruses were visualized using 488 and 561 nm lasers and associated emission filters respectively (as described above), and laser intensity/gain for each channel were optimized and held constant between animals. Z-stack images totaling 70µm thickness were captured for each region and collapsed into maximum-intensity projections. Four sections (every other section) that contained the highest infectivity in the input regions (ipsilateral and contralateral PrS/PaS and contralateral MEC) were imaged. After identifying information was removed from the resulting files, blinded independent researchers counted the number of fluorescently labeled cells within regions. For each region of interest, regional cell counts were divided by the total number of cells counted (across all regions), to determine relative input strength.

scRNAseq Analysis.

ADGRL2 scRNAseq gene counts were analyzed from the Allen Brain Institute 10x RNAseq database from hippocampal and EC tissues (Tasic et al., 2018). Downloaded RNAseq data was pre-processed to obtain normalized gene counts with Python 3.7. All subsequent analysis was performed using Dplyr package in R. Hippocampal cell type

classifications (DG granule cells, CA1 and CA3 pyramidal) were taken from predefined database assignments. EC database defined cells were further defined into cell type classifications (*Oxr-1, Wfs-1, Reelin*) based on surpassing marker gene expression thresholds, defined as CPM (counts per million) greater than the 25% truncated CPM mean for database defined cell types that align to their respective layers.

Quantification and Statistical Analysis.

All data analysis was performed using Prism 7 software (GraphPad). Data are shown as mean ± SEM. Significance testing was performed using either one-way ANOVA with post-hoc Tukey's test for multiple comparisons, or via two-tailed Student's t-test, as appropriate. Statistically significant differences are indicated by asterisks (*$p<0.05$; **$p<0.01$; ***$p<0.001$).

Chapter 2 References

Anderson, G.R., Maxeiner, S., Sando, R., Tsetsenis, T., Malenka, R.C., and Südhof, T.C. (2017). Postsynaptic adhesion GPCR latrophilin-2 mediates target recognition in entorhinal-hippocampal synapse assembly. J Cell Biol *216*, jcb.201703042.

Basu, J., and Siegelbaum, S.A. (2015). The Corticohippocampal Circuit, Synaptic Plasticity, and Memory. Csh Perspect Biol *7*, a021733.

Berns, D.S., DeNardo, L.A., Pederick, D.T., and Luo, L. (2018). Teneurin-3 controls topographic circuit assembly in the hippocampus. Nature *554*, 328.

Boccara, C.N., Sargolini, F., Thoresen, V.H., Solstad, T., Witter, M.P., Moser, E.I., and Moser, M.-B. (2010). Grid cells in pre- and parasubiculum. Nat Neurosci *13*, 987–994.

Boucard, A.A., Maxeiner, S., and Südhof, T.C. (2014). Latrophilins function as heterophilic cell-adhesion molecules by binding to teneurins: regulation by alternative splicing. The Journal of Biological Chemistry *289*, 387–402.

Caballero-Bleda, M., and Witter, M.P. (1993). Regional and laminar organization of projections from the presubiculum and parasubiculum to the entorhinal cortex: An anterograde tracing study in the rat. J Comp Neurol *328*, 115–129.

Caballero-Bleda, M., and Witter, M.P. (1994). Projections from the presubiculum and the parasubiculum to morphologically characterized entorhinal-hippocampal projection neurons in the rat. Exp Brain Res *101*, 93–108.

Canto, C.B., Koganezawa, N., Beed, P., Moser, E.I., and Witter, M.P. (2012). All Layers of Medial Entorhinal Cortex Receive Presubicular and Parasubicular Inputs. J Neurosci *32*, 17620–17631.

Donato, F., Jacobsen, R.I., Moser, M.-B., and Moser, E.I. (2017). Stellate cells drive maturation of the entorhinal-hippocampal circuit. Science *355*, eaai8178.

Fanselow, M.S., and Dong, H.-W. (2010). Are the Dorsal and Ventral Hippocampus Functionally Distinct Structures? Neuron *65*, 7–19.

Fuchs, E.C., Neitz, A., Pinna, R., Melzer, S., Caputi, A., and Monyer, H. (2016). Local and Distant Input Controlling Excitation in Layer II of the Medial Entorhinal Cortex. Neuron *89*, 194–208.

Groen, T. van, Miettinen, P., and Kadish, I. (2003). The entorhinal cortex of the mouse: Organization of the projection to the hippocampal formation. Hippocampus *13*, 133–149.

Henke, P.G. (1990). Hippocampal pathway to the amygdala and stress ulcer development. Brain Res Bull *25*, 691–695.

Kawano, J., Fujinaga, R., Yamamoto-Hanada, K., Oka, Y., Tanizawa, Y., and Shinoda, K. (2009). Wolfram syndrome 1 (Wfs1) mRNA expression in the normal mouse brain during postnatal development. Neurosci Res *64*, 213–230.

Kitamura, T., Pignatelli, M., Suh, J., Kohara, K., Yoshiki, A., Abe, K., and Tonegawa, S. (2014). Island Cells Control Temporal Association Memory. Science *343*, 896–901.

Kitamura, T., Sun, C., Martin, J., Kitch, L.J., Schnitzer, M.J., and Tonegawa, S. (2015). Entorhinal Cortical Ocean Cells Encode Specific Contexts and Drive Context-Specific Fear Memory. Neuron *87*, 1317–1331.

Kononenko, N.L., and Witter, M.P. (2012). Presubiculum layer III conveys retrosplenial input to the medial entorhinal cortex. Hippocampus *22*, 881–895.

Li, J., Shalev-Benami, M., Sando, R., Jiang, X., Kibrom, A., Wang, J., Leon, K., Katanski, C., Nazarko, O., Lu, Y.C., et al. (2018). Structural Basis for Teneurin Function in Circuit-Wiring: A Toxin Motif at the Synapse. Cell *173*, 735-748.e15.

Li, J., Xie, Y., Cornelius, S., Jiang, X., Sando, R., Kordon, S.P., Pan, M., Leon, K., Südhof, T.C., Zhao, M., et al. (2020). Alternative splicing controls teneurin-latrophilin interaction and synapse specificity by a shape-shifting mechanism. Nat Commun *11*, 2140.

Lu, Y.C., Nazarko, O.V., Sando, R., Salzman, G.S., Li, N.-S.S., Südhof, T.C., and Araç, D. (2015). Structural Basis of Latrophilin-FLRT-UNC5 Interaction in Cell Adhesion. Structure (London, England : 1993) *23*, 1678–1691.

Miao, C., Cao, Q., Moser, M.-B., and Moser, E.I. (2017). Parvalbumin and Somatostatin Interneurons Control Different Space-Coding Networks in the Medial Entorhinal Cortex. Cell *171*, 507-521.e17.

Moser, M.B., Moser, E.I., Forrest, E., Andersen, P., and Morris, R.G. (1995). Spatial learning with a minislab in the dorsal hippocampus. Proc National Acad Sci *92*, 9697–9701.

Muessig, L., Hauser, J., Wills, T.J., and Cacucci, F. (2015). A Developmental Switch in Place Cell Accuracy Coincides with Grid Cell Maturation. Neuron *86*, 1167–1173.

Nilssen, E.S., Doan, T.P., Nigro, M.J., Ohara, S., and Witter, M.P. (2019). Neurons and networks in the entorhinal cortex: A reappraisal of the lateral and medial entorhinal subdivisions mediating parallel cortical pathways. Hippocampus *29*, 1238–1254.

Oh, S., Harris, J.A., Ng, L., Winslow, B., Cain, N., Mihalas, S., Wang, Q., Lau, C., Kuan, L., Henry, A.M., et al. (2014). A mesoscale connectome of the mouse brain. Nature *508*, 207.

O'Sullivan, M.L., Wit, J. de, Savas, J.N., Comoletti, D., Otto-Hitt, S., Yates, J.R., and Ghosh, A. (2012). FLRT proteins are endogenous latrophilin ligands and regulate excitatory synapse development. Neuron *73*, 903–910.

Paxinos, G., and Franklin, K.B. (2004). The mouse brain in stereotaxic coordinates, 4th edition.

Pederick, D.T., Lui, J.H., Gingrich, E.C., Xu, C., Wagner, M.J., Liu, Y., He, Z., Quake, S.R., and Luo, L. (2021). Reciprocal repulsions instruct the precise assembly of parallel hippocampal networks. Science *372*, 1068–1073.

Ray, S., and Brecht, M. (2016). Structural development and dorsoventral maturation of the medial entorhinal cortex. Elife *5*, e13343.

Sando, R., and Südhof, T.C. (2021). Latrophilin GPCR signaling mediates synapse formation. Elife *10*, e65717.

Sando, R., Jiang, X., and Südhof, T.C. (2019). Latrophilin GPCRs direct synapse specificity by coincident binding of FLRTs and teneurins. Science (New York, N.Y.) *363*.

Silva, J.-P.P., Lelianova, V.G., Ermolyuk, Y.S., Vysokov, N., Hitchen, P.G., Berninghausen, O., Rahman, M.A., Zangrandi, A., Fidalgo, S., Tonevitsky, A.G., et al. (2011). Latrophilin 1 and its endogenous ligand Lasso/teneurin-2 form a high-affinity transsynaptic receptor pair with signaling capabilities. Proceedings of the National Academy of Sciences of the United States of America *108*, 12113–12118.

Sugita, S., Ichtchenko, K., Khvotchev, M., and Südhof, T.C. (1998). α-Latrotoxin Receptor CIRL/Latrophilin 1 (CL1) Defines an Unusual Family of Ubiquitous G-protein-linked Receptors G-PROTEIN COUPLING NOT REQUIRED FOR TRIGGERING EXOCYTOSIS*. J Biol Chem *273*, 32715–32724.

Suh, J., Rivest, A.J., Nakashiba, T., Tominaga, T., and Tonegawa, S. (2011). Entorhinal Cortex Layer III Input to the Hippocampus Is Crucial for Temporal Association Memory. Science *334*, 1415–1420.

Sürmeli, G., Marcu, D.C., McClure, C., Garden, D.L.F., Pastoll, H., and Nolan, M.F. (2015). Molecularly Defined Circuitry Reveals Input-Output Segregation in Deep Layers of the Medial Entorhinal Cortex. Neuron *88*, 1040–1053.

Tasic, B., Yao, Z., Graybuck, L.T., Smith, K.A., Nguyen, T.N., Bertagnolli, D., Goldy, J., Garren, E., Economo, M.N., Viswanathan, S., et al. (2018). Shared and distinct transcriptomic cell types across neocortical areas. Nature *563*, 72–78.

Tervo, D.G.R., Hwang, B.-Y., Viswanathan, S., Gaj, T., Lavzin, M., Ritola, K.D., Lindo, S., Michael, S., Kuleshova, E., Ojala, D., et al. (2016). A Designer AAV Variant Permits Efficient Retrograde Access to Projection Neurons. Neuron *92*, 372–382.

Toro, D.D., Carrasquero-Ordaz, M.A., Chu, A., Ruff, T., Shahin, M., Jackson, V.A., Chavent, M., Berbeira-Santana, M., Seyit-Bremer, G., Brignani, S., et al. (2020). Structural Basis of Teneurin-Latrophilin Interaction in Repulsive Guidance of Migrating Neurons. Cell *180*, 323-339.e19.

Witter, M.P., and Moser, E.I. (2006). Spatial representation and the architecture of the entorhinal cortex. Trends Neurosci *29*, 671–678.

Witter, M.P., Doan, T.P., Jacobsen, B., Nilssen, E.S., and Ohara, S. (2017). Architecture of the Entorhinal Cortex A Review of Entorhinal Anatomy in Rodents with Some Comparative Notes. Frontiers Syst Neurosci *11*, 46.

Zhang, R.S., Liakath-Ali, K., and Südhof, T.C. (2020). Latrophilin-2 and latrophilin-3 are redundantly essential for parallel-fiber synapse function in cerebellum. ELife *9*.

Chapter 3: Synaptic cell adhesion molecule Latrophilin-2 expression in medial entorhinal layer III neurons controls precise axonal topology and spatial learning

Jordan D. Donohue[1,2], Elizabeth D. Liu[1,3], Lisette Saab[1], Rajbir Kaur[1], Woojin Yang[1], Garret R. Anderson[1]*

[1]Department of Molecular, Cell, and Systems Biology; University of California - Riverside; Riverside, CA 92521, USA

[2]Neuroscience Graduate Program; University of California - Riverside; Riverside, CA 92521, USA

[3]School of Medicine; University of California - Riverside; Riverside, CA 92521, USA

*Correspondence: garret.anderson@ucr.edu

Summary.

Distinct functions of the brain arise from specific connectivity between populations of neurons which form functional circuits. Synaptic cell adhesion molecules are a class of proteins known to be involved with synapse development and axonal guidance through interactions with other synaptic proteins. Trans-synaptic interactions between these molecules are shown to control specificity of connections between distinct proximal and distal hippocampal regions. Among these molecules, Latrophilin-2 and Teneurin-3 are expressed in a topographically distinct fashion which we find coincides with axonal patterning of these distinct neuronal populations. We created a transgenic mouse which

allows for deletion of Latrophilin-2 expression in medial entorhinal cortex (MEC) neurons. Using these mice, we find several distinct differences due to Lphn2 deletion in MEC layer III neurons. We find alterations in precise topology of MEC layer III axons into contralateral MEC layer I, but not other axonal outputs. We also find that inputs from Pre-subiculum exhibit deficits in precise targeting of axons shifted away from Latrophilin-2 enriched zones. Using spine density analysis for MEC layer III neurons across their dendritic trees, we find that their distal secondary apical shafts in deep layer III and superficial layer I exhibit fewer post synaptic spines where input axons fail to reach. We then use our transgenic mouse to test the behavioral consequences of Latrophilin-2 deletion in these neurons. We find most tasks are unaffected except learning of alternating spatial tasks which previously have been shown to be modulated by MEC layer III neurons. Together this shows MEC specific deletion of Lphn2 causes defects in precise targeting of distinct inputs and that these mice exhibit subtle but distinct differences in sequential spatial learning.

Introduction.

Proper function of the brain is dependent on highly specific patterning of connections which arise between pre- and post-synaptic neurons. Throughout the visual processing system there are topographically distinct connections between pre- and post-synaptic neurons that are necessary for proper function. This is shown across the visual processing system from the retina (Leamey et al. 2007), to visual cortices, (Wang, Gao, and Burkhalter 2011) and pre-subiculum inputs to the entorhinal cortex (Caballero-Bleda and Witter 1993; Kononenko and Witter 2012). Throughout the visual processing network these highly organized synaptic contacts are crucial for different aspects of visual

processing. The specificity of these connections can be thought of in several ways including region-specific, layer-specific, and subregion-specific. Development of these topographical patterns in the brain have been shown to be controlled by molecular gradients (Leamey et al. 2007; Sur 2005).

Synaptic cell adhesion molecules (sCAMs) are a class of proteins which have been known for their roles in synaptic development and axon guidance. Some of these molecules include Latrophilins (Lphn1-3), Teneurins (Tenm1-4) and Fibronectin leucine rich transmembrane proteins (FLRT1-3). These molecules are known to function through trans-synaptic binding, physically anchoring pre- and post-synaptic neurons together in functional connected populations (Li et al. 2020). Several of these molecules have been shown crucial for normal topographical patterning development of synapses in several brain regions. Among these, Teneurin-3 (Tenm3) and Latrophilin-2 (Lphn2) have been shown to be critical for normal synaptic development in the hippocampus and are expressed in opposing interconnected compartments (Berns et al. 2018; Pederick et al. 2021). These compartments are referred to by their distance to the Dentate Gyrus, either proximal or distal (Lee, GoodSmith, and Knierim 2020; Donohue et al. 2021). We have shown that there is specific connectivity between discrete proximal and distal hippocampal regions for hippocampal regions studied. We previously found that Lphn2 is important for development of inputs to distal MEC neurons arising from the ipsilateral Pre-subiculum (Donohue et al. 2021). In CA1 pyramidal neurons, Lphn2 is crucial for synapse development arising from MEC neurons (Anderson et al. 2017; Sando, Jiang, and Südhof 2019). It has also been shown that Tenm3 and Lphn2 expression are important for specific axon topography between CA1 and SUB neurons (Pederick et al. 2021). Although the field

has made great strides in understanding how these molecules work, there is much debate regarding pre- or post-synaptic specific function among these molecules.

Recently, it was discovered that Tenm3 controls connectivity from proximal MEC to proximal CA1 through a pre-synaptic role, and not a post-synaptic role (Zhang et al. 2022). In our previous work we found that Lphn2 controls development of post-synaptic dendritic spines and fewer pre-synaptic neurons were labelled with retrograde tracer from the Presubiculum. We found evidence when local neuronal expression of Lphn2 was removed that post-synaptic protein residing in dendrites was decreased, but we did not test possible pre-synaptic roles. Although sCAMs have roles in assembly of neural circuits, how is this relevant to brain function? We know mutations in Lphns (Arcos-Burgos et al. 2010) and their binding partners (Burbach and Meijer 2019; Miraoui et al. 2013; Yuen et al. 2015; Mercati et al. 2017) are associated with neurodevelopmental diseases. Lphn2 targeted deletion in CA1 pyramidal neurons of the hippocampus causes specific behavioral deficits which are similar to deficits in behavior due to brain wide deletion of Lphn2 (Anderson et al. 2017) involving alternating spatial memory but not other related similar tasks. Although we know the function of Lphn2 in hippocampal neurons in relation to their precise axonal projections and behavioral modulation, we want to know if Lphn2 functions similarly for hippocampal inputs.

To better understand the function of Lphn2 in parahippocampal circuit development, we wanted to test the role of Lphn2 in both pre- and post-synaptic axonal targeting of MEC neurons and previously identified Lphn2 dependent inputs. To accomplish this, we created a transgenic mouse containing flanking LoxP sites to delete Lphn2 expression bred with the C57BL/6N-Tg(Oxr1-cre)C14Stl/J **(**OXR1^{CRE}) mouse to elicit robust Lphn2 deletion in MEC neurons without affecting nearby interconnected

neurons. Using this mouse, we were able to co-label proximal and distal MEC layer III neurons and found that these two populations of neurons have discrete axon projection topography for either proximal or distal compartments in multiple hippocampal regions. We found that distal MEC axon projections to contralateral distal MEC layer I were shifted in the proximal direction, where proximal projections to contralateral MEC layer I shifted in the distal direction. We did not observe alterations in either layer specific or proximal/distal specific axon topography in MEC outputs to other hippocampal regions. We also labelled Pre-subiculum neurons and their axons, finding that the specificity of their projections to ipsilateral distal MEC layer III was disrupted, but not their contralateral axon topography. Accompanied by neuron morphology and spine density experiments our data supports Lphn2 having a primarily post-synaptic role in circuit assembly and maintenance. To test the role of Lphn2 in behavioral function of these MEC neurons we designed a set of similar behavioral experiments as done in CA1 specific Lphn2 deletion, where we saw differences in learning and recall of spatial memory tasks (Anderson et al. 2017). In this study, we observed deficits in learning, but not recall in cognitive flexibility spatial tasks and not other spatial learning tasks. Together this suggests that Lphn2 plays a fundamental role in synapse assembly between multiple topographically connected regions and loss of Lphn2 expression in these leads to deficits in sequential spatial learning.

Results.

Proximal & Distal MEC neurons have topographically distinct projection patterns that coincide with expression gradients of Lphn2/Tenm3

To better understand differences in connectivity between proximal and distal compartments of hippocampal regions we first wanted to confirm previous reports that Latrophilin-2 (Lphn2) expression is opposed by Teneurin-3 (Tenm3) expression for either proximal or distal compartments of hippocampal regions. We performed single molecule fluorescent in-situ hybridization (smFISH) for Tenm3 and Lphn2 in previously identified horizontal hippocampal sections (figure 1A) containing high Lphn2 expression in the MEC (Donohue et al. 2021). With the knowledge of these parallel curicuits with opposing expression gradients of Lphn2 and Tenm3, we wanted to investigate the role of Latrophilin-2 in precise axon topology of layer III MEC neurons. To accomplish this, we made a transgenic mouse that expresses CRE-recombinase using the OXR1 promoter to drive expression of CRE in MEC layer III pyramidal neurons as in several previous studies which have shown layer III MEC specific expression (Suh et al. 2011). We crossed this mouse with Lphn2-mVenusF$^{L/FL}$ reporter mice to determine if there was loss of Lphn2 protein in superficial MEC layers (figure 1C). Using Immunostaining to boost Lphn2 resolution we compared protein levels in the MEC (figure 1D) and CA1 (figure 1E) using line scans normalized to 100% and background subtracted by fluorescence levels measured in the Dentate Gyrus as a previously established negative control.

We then crossed the OXR1^{CRE} mice with our Lphn2$^{FL/FL}$ mouse and Lphn2$^{WT/WT}$ mice to compare projection patterns between Lphn2 enriched neurons in the distal MEC (dMEC) and Teneurin-3 (Tenm3) enriched neurons in the proximal MEC (pMEC) (figure 1F). To compare axon precise projection topology, we used a regional IHC marker for

Wolframin Syndrome 1 (Wfs1). Wfs1 staining is observed in the Parasubiculum (PaS) but not PrS, and in layer II of the MEC (figure 1G) to precisely label regional boundaries surrounding the MEC. IHC in conjunction with landmarks such as the rhinal fissure were used to delineate the borders of regions investigated for both viral localization and precise axonal topology. Using OXR1^{CRE} mice, mice were co-labelled proximal and distal discrete MEC populations using dual injections of GFP and tdTomato viruses (figure 1H) observing cre-dependent MEC specific labelling of neurons. Combined with Wfs1 immunofluorescence (Figure 1H & I) we can clearly delineate cortical layers and observe labelling of layer III neurons, where surround layers do not exhibit labelled cells.

Lphn2 deletion in MEC layer III neurons does not affect hippocampal projection topology

To compare axonal patterning of MEC neurons we first needed to confirm similar that there was viral localization of MEC neurons between samples. We compared injection localization between control mice and MEC-KO mice and compared six pairs of injections with similar localization and infectivity of tdTomato virus for pMEC (figure 2B) and GFP for dMEC (figure 2D). We then quantified localization by measuring relatove fluorescence levels using a line scan across layer III from pMEC to dMEC to confirm similar virus localization (figure 2B). Using these injected brains, ipsilateral and contralateral hippocampal CA1 were compared (figure 2C). A similar line scan as in B was used, but line is drawn traversing the SLM layer from pCA1 to dSUB. These measurements were used to compare fluorescence levels between control and MEC-KO mice for axon localization in the SLM, in which no differences were observed (figure 2D). This was repeated in a layer-specific fashion traversing the layers of hippocampus from the alveus to SLM comparing layer specificity of axons across groups, showing no significant changes (figure 2E). This was repeated for dMEC injections finding similar results for

localization (figure 2F & G), and CA1 projection topology (figure 2H & I) and layer specificity (figure 2J).

Lphn2 deletion from MEC layer III neurons alters contralateral MEC projection topology

We then wanted to determine if deletion of Lphn2 in MEC layer III neurons affects contralateral MEC projection topology in which there is pre- and post-synaptic deletion between neurons. We first compare projection patterns from contralateral pMEC tdTomato axons into MEC layer I (figure 3A). Using a similar line scan traversing the proximal to distal axis across MEC layer I, we not observe any differences when comparing each of the 100 normalized percentages accounting for multiple comparisons (figure 2B). We then looked at average signal intensity between the proximal and distal halves of the projection data and found an increase of signal for pMEC tdTomato axons in contralateral dMEC layer I, indicating a shift in axon topology. In figure 2E, we then used these images to compare layer specificity of these axons and found no difference. We then repeated this experiment for distal MEC neurons and their projections to contralateral MEC (figure 3D-H). When comparing axon topology, we found dramatically altered axon topology where axons did not extend into the distal MEC (figure 3E & F), but still had similar layer specific targeting (figure 3H). All together we find that Lphn2 deletion in MEC cause a robust deficit in axon targeting for contralateral dMEC neurons shifted away from high Lphn2 expression zones, and a smaller yet significant effect for pMEC neurons in which their topology shifted towards Lphn2 enrichment zones.

Lphn2 deletion from MEC layer III neurons alters pre-subiculum input topology

Previous work has shown the proximal pre-subiculum neurons preferentially project to distal MEC layer III, and distal PrS neurons project to proximal MEC layer III (Caballero-Bleda and Witter 1993; Donohue et al. 2021). To test if Lphn2 expression in distal MEC neurons may play a role in this specificity of axonal targeting we used similar OXR1^{CRE}; Lphn2$^{FL/FL}$ mice as in figures 2 and 3, combined with proximal PrS targeted injection of CamK2-YFP to compare axonal projections from pyramidal neurons into the MEC (figure 4A). We first compared injection localization and using a line intensity analysis (figure 4B). Selecting animals with similar viral targeting, we compared the projection patterning of their outputs into both ipsilateral and contralateral MEC layer III. Using a ine intensity analysis on their axons in MEC layer III, we compared Lphn2^{WT} mice with Lphn2$^{FL/FL}$ mice we found that in WT mice ipsilateral projections from proximal PrS targetted dMEC (figure 4C) as expected. In Lphn2$^{FL/FL}$ mice however, ipsilateral projections were localized more proximally (figure 4D,E). The same brains were then used to compare contralateral proximal-distal localization of axons, but no differences were found between groups. Using the same images, we then compared layer specificity of axon signal finding that both ipsilateral and contralateral projections had similar layer III targeting specificity (figure 4I,J). Overall, these experiments suggest that Lphn2 deletion in MEC causes deficits in proximal-distal targeting of ipsilateral but not contralateral PrS inputs.

Lphn2 KO in MEC layer III neurons decreases spine density in distal secondary apical shafts

Our previous work examined pyramidal neurons in the MEC and spine density for their local processes, finding deep layer III pyramidal neurons had fewer spines on their secondary apical shafts. To get a more complete understanding, we wanted to compare neuron morphology and spine density across the entire dendritic tree of these distal MEC layer III pyramidal cells enriched in Lphn2 expression. To accomplish this, we injected Lphn2$^{FL/FL}$ littermate paired neonatal mice with either a control tdTomato virus for neuronal labelling, or a cocktail of hSyn-CRE and FLEX- tdTomato virus to elicit Lphn2 deletion in sparse neurons of distal MEC (figure 5A, B). We reconstructed and compared superficial alongside deep MEC layer III pyramidal neurons for their secondary basal and apical shafts in deep MEC layer III or I (figure 5C) where Lphn2 protein is most enriched. We found that basal shafts were unaffected for spine density (figure 5D), but secondary apical shafts in both deep layer III and superficial layer I exhibited a decrease of spine density (figure 5E). Together this shows that Latrophilin-2 expression in layer III MEC pyramidal neurons is important for post-synaptic spine development in deep layer III and superficial layer I for terminal dendritic branches on the apical shaft.

Lphn2 KO in MEC layer III neurons causes deficits in alternating spatial learning

Having shown that Lphn2 deletion in MEC neurons causes deficits in specificity of axonal inputs and spine density in post synaptic neurons, we wanted to test these mice to determine if there were differences in their behavior and learning. Previous work has shown that hippocampal Lphn2 deletion causes deficits in acquisition of alternating spatial tasks in the water T-maze, alongside enhanced recall of spatial learning in the Barnes

Maze. Other spatial memory tasks were tested in these mice with no changes found. We wanted to repeat these tasks in these new mice to determine if MEC specific Lphn2 deletion would have similar or different effects as CA1 specific deletion.

Using sex matched littermate pairs of mice (figure 6A), we started behavioral testing at 2 months of age with the Open Field Test. Mice were allowed to navigate the open field for 5 minutes while being recorded. We divided the arena into central and peripheral zones using an automated behavior tracking software. We then analyzed movement speed, distance, and periphery distance to determine if there were differences in locomotor activity in these mice, or anxiety like behavior indicated by an increase of time spent in the periphery of the arena. We did not observe any significant differences in distance traversed, distanced traversed in the periphery, or movement speed of the mice due to genotype (figure 6B). We then subjected mice to the novel object recognition task, which is oftentimes thought of as dependent on the Lateral Entorhinal Cortex and its connections to CA1 (Wilson et al. 2013). Using a discrimination ratio to compare time spent with novel and familiar objects 1 hour after exposure to familiar objects, we did not find significant differences between groups due to genotype (figure 6C).

To further test spatial memory, we subjected these same mice to the Barnes Maze where they are placed in a brightly lit platform with 20 evenly spaced holes around the perimeter. There are visual cues outside of the maze to help orient the mice, and one of the holes leads to an area under the arena away from the bright light which mice naturally prefer. For 4 days, mice are tested 5 times each day how fast they can find the target hole which does not change location. On day 5 they perform a single trial deemed test 1 to examine short term memory where latency to investigate test hole is measured. Mice are

then tested 2 weeks later to compare long term memory of the hole (figure 6D). We found no changes in acquisition of the task or recall for either test trial (figure 6E, F).

We then used the Water T-maze cognitive flexibility task to compare learning of alternating spatial tasks in which the mice must learn the escape platform on the second trial is always on the opposite side of the first randomized trial (figure 6G). We found no differences in learning the randomized one arm swim, but CRE+ mice exhibited a longer latency to find the hole during the first day of training. We found differences across individual trials (figure 6H) and by day on average (figure 6I) for the first day of training but not for later days. Together these behavioral assays indicate there is a decrease of learning for spatial learning which requires cognitive flexibility, but not for other hippocampal dependent spatial tasks.

Discussion.

In this study we show that neurons in either proximal or distal MEC project to either proximal or distal compartments of several hippocampal subregions, that connectivity overlaps with expression gradients between Latrophilin-2 and Teneurin-3. Our results show MEC specific Lphn2 deletion causes deficits in normal axon targeting for ipsilateral pre-subiculum and contralateral MEC axons targeting the distal MEC where afferents of both regions are shifted more proximally. We then show Lphn2 deletion in distal MEC layer III neurons caused fewer post-synaptic spines in secondary apical shafts residing where these inputs fail to reach in layers I and III. For mice lacking Lphn2 expression in MEC layer III neurons we found that most behavior was unaffected except for the learning of sequential spatial tasks which are known to be dependent on MEC layer 3 pyramidal neurons (Suh et al. 2011). Overall, these data suggest that Lphn2 is a crucial regulator of

input specific connectivity in distal MEC neurons and has a role in particular aspects of cognition.

Our previous work showed multiple prominent inputs to the MEC were organized between discrete proximal and distal populations, whereas our current work shows that MEC layer III neurons outputs are largely organized in this same fashion. Combined with the fact that CA1 and subiculum contain these parallel networks controlled by Lphn2 and Tenm3 expression (Pederick et al. 2021), it appears that these parallel circuits exist across multiple nodes within the hippocampal network. We find that MEC specific Lphn2 deletion alters acquisition of cognitive flexibility learning tasks, in contrast to CA1 specific deletion that affects learning and recall of these tasks (Anderson et al. 2017). As mutations in Teneurins and Latrophilins have been associated with neurodevelopmental disease, it is crucial we understand the molecular mechanisms that underly this connectivity and what the deficits in connectivity mean for the circuit.

Latrophilins, Teneurins and FLRTs have been known to form trans-synaptic complexes, and differential binding between these molecules can promote excitatory or inhibitory synapse development (Li et al. 2020). Although these trans-synaptic interactions are known to occur, it is debated which proteins reside in pre- or post-synaptic compartments, or if they reside in both. In the case of Tenm3, some studies show pre- and post-synaptic deletions of this gene cause deficits in precise connectivity between SUB neurons and CA1 neurons (Berns et al. 2018). Whereas some studies show pre- but not post-synaptic Tenm3 expression is necessary for normal synaptic development in MEC layer III neurons projections to hippocampal SLM (Zhang et al. 2022). In terms of the opposing gene Lphn2, it is reported that upregulated expression of Lphn2 in presynaptic neurons of proximal CA1 causes robust difference in their axonal targeting to SUB

(Pederick et al. 2022). Another study showed deletion of Lphn2 in these pre-synaptic neurons causes subtle, but distinct differences in axonal targeting (Pederick et al. 2021). In line with these findings, our experiments show MEC Lphn2 deletion in both hemispheres contributes to abhorrent targeting of distal MEC neurons onto contralateral MEC neurons. Additionally, we find that ipsilateral Prs projections to distal MEC are altered from WT pre-synaptic neurons to Lphn2-KO post-synaptic neurons. Overall, we find that Lphn2 deletion in MEC layer III neurons does not affect the precise topology of many MEC projection targets in either a proximal-distal, or layer specific fashion. We also find that protein signal is decreased in post-synaptic areas of these neurons (MEC), but not where their axons target (hippocampal SLM) suggesting that protein is primarily localized in post-synaptic compartments. These results suggest that it may not be as simple as each molecule having a discrete pre- or post-synaptic function, but rather it may depend on where the neuron is located. Although the pre- or post-synaptic roles of these molecules can be debated, the role of these different molecular gradients and how they control circuit formation related to specific aspects of learning is an important but unanswered question.

In the MEC, Lphn2 protein is expressed in a gradient fashion from the dorsal to ventral axis (Donohue et al. 2021), which coincides with differences in function between dorsal and ventral MEC layer III neurons (Giocomo et al. 2014). Examples of functional classes of neurons include grid cells in the EC which fire in a topographically organized grid like fashion across space (Cells et al. 2015; Carpenter et al. 2015). Grid cells in the EC connect to hippocampal place cells that fire in discrete locations in space, which has led scientists to hypothesize this activity is crucial to perception of spatial maps. In CA1 there is a dorsal to ventral scale expansion of place fields (Jung, Wiener, and McNaughton 1994; Kjelstrup et al. 2008), whereas in MEC there is a dorsal to ventral expansion in size

of grid patterns (Stensola et al. 2012). MEC layer III cells have activity shown to be modulated by head direction of the animal(Giocomo et al. 2014; Robertson et al. 1999), which is more sharply tuned in dorsal neurons compared to ventral MEC layer III neurons in a gradient like fashion (Giocomo et al. 2014) and dependent on Pre-Subiculum input (Kononenko and Witter 2012). In humans, MRI data shows functional differences related to spatial processing across this axis as well (Evensmoen et al. 2015).

Although scientists have investigated differences in functional properties between dorsal and ventral neurons, studies have not investigated functional differences between proximal and distal compartments of MEC neurons using precise molecular markers. Our work and the work of others suggests that within this circuit these parallel pathways have distinct molecules controlling synapse development. There evidence that these proximal and distal populations of neurons have distinct differences in function, one study in mice shows that proximal CA1 is highly tuned to spatial information, whereas distal CA1 is sensitive to temporal information (Beer et al. 2018). This functional difference between proximal and distal CA1 neurons is mirrored in humans (Montchal, Reagh, and Yassa 2019). Does Teneurin-3 and Latrophilin-2 mediated synapse assembly in these discrete compartments control complementary aspects of cognition as shown to occur in CA1? Our current study does not address these questions, but future studies using cell-type specific genetic models combined with targeted deletion of these molecules in discrete regions of this circuit will help us understand how distinct proximal or distal neurons within this circuit comprise specific cognitive capabilities. If we can identify distinct aspects of learning and memory associated with spatially restricted neurons, we will be able to better understand how the brain works together to form new memories. Gaining insight into the molecular control of discrete aspects of learning and cognition, we may likely gain insight

into the neurological diseases associated with mutations in these genes giving us better tools to help treat these diseases.

Author Contributions.

Author Contributions: J.D.D. designed, performed, and analyzed most experiments; G.R.A. helped design experiments and quantification methods; E.D.L. and L.S. performed neuron reconstructions; W.Y. and R.K. performed behavioral analysis; J.D.D. and G.R.A. wrote the paper with input from all of the authors.

Acknowledgements. This paper was supported by a grant from the Whitehall Foundation (2018-08-01) and Initial Complement Funds from the University of California, Riverside to G.R.A.

Main Figures and Title Legends.

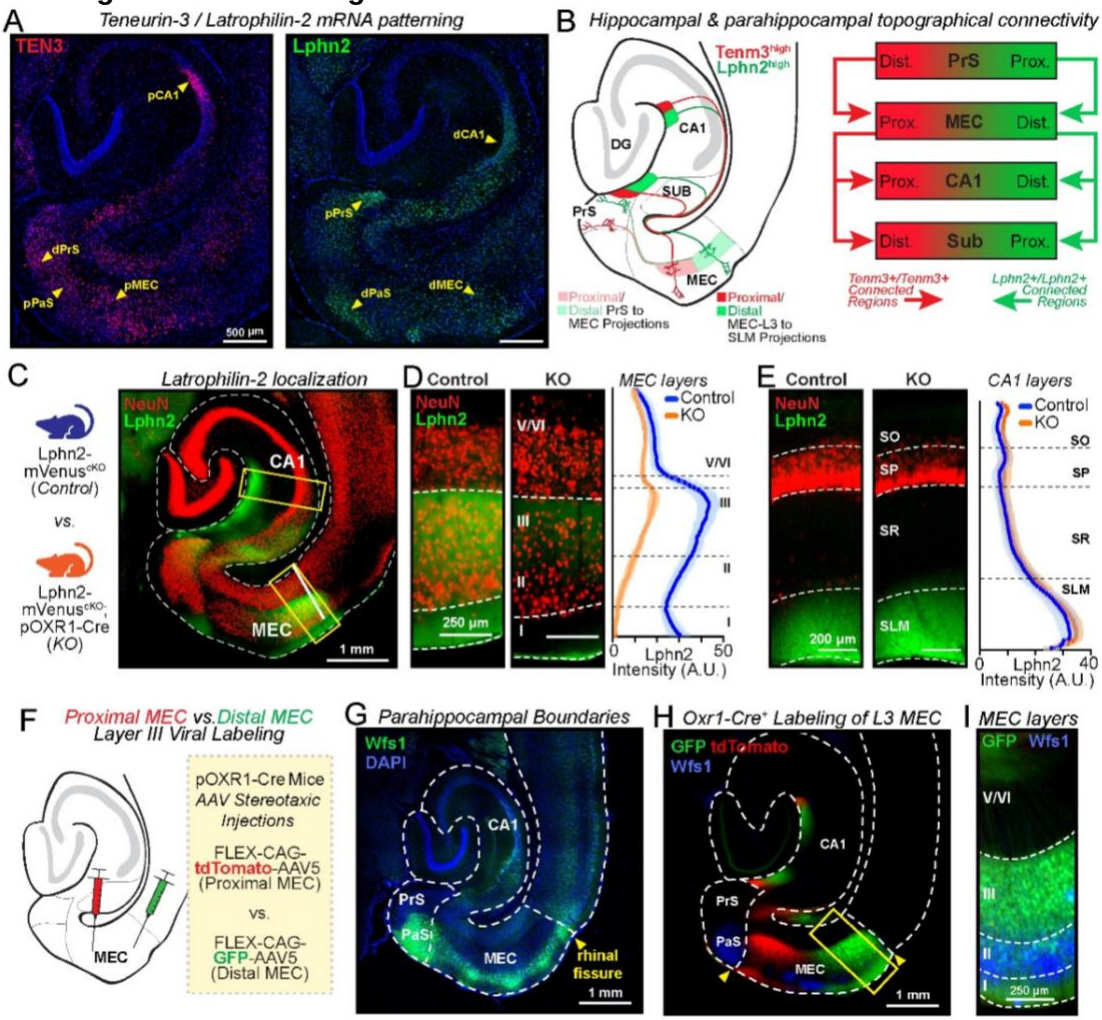

Figure 1. Teneurin-3 and Latrophilin-2 enriched neurons form non-overlapping parallel pathways

(A) (Left) TENM3 mRNA patterning in the hippocampal circuit. (Right) Lphn2 mRNA patterning in the hippocampal circuit (B) (Left) Topographical circuit diagram of known proximal-distal organized MEC inputs/outputs. (Right) circuit diagram with molecules known to control the specificity of these connections (C) (Left) Genotype description of mice used for experiment, (right) representative image of hippocampal circuit with labelled neurons (red, NeuN) and Lphn2 protein (green, Lphn2). (D) Representative images of control (left) and OXR1^{CRE} (middle) MEC layers. (Right) line scan of fluorescent intensity across MEC layers. (E) Representative images of control (left) and OXR1^{CRE} (middle) mice across CA1 layers. (Right) line scan of fluorescent intensity across CA1 layers. (F) AAV experimental schematic targeting MEC using FLEX-CAG-tdTomato-AAV5 and FLEX-CAG-GFP-AAV5 to label proximal and distal MEC OXR1+ neurons. (G) Hippocampal circuit with labelled Wfs1 protein illustrating pre-subiculum and para-subiculum borders alongside MEC border (rhinal fissure) where layer 2 Wfs1 labelling ends used to determine regional boundaries. (H) Representative hippocampal circuit image with labelled proximal/distal MEC neurons and their ipsilateral CA1 projections. (I) Representative image of distal MEC with GFP labelled neurons and Wfs1 staining illustrating how layers were determined for analysis.

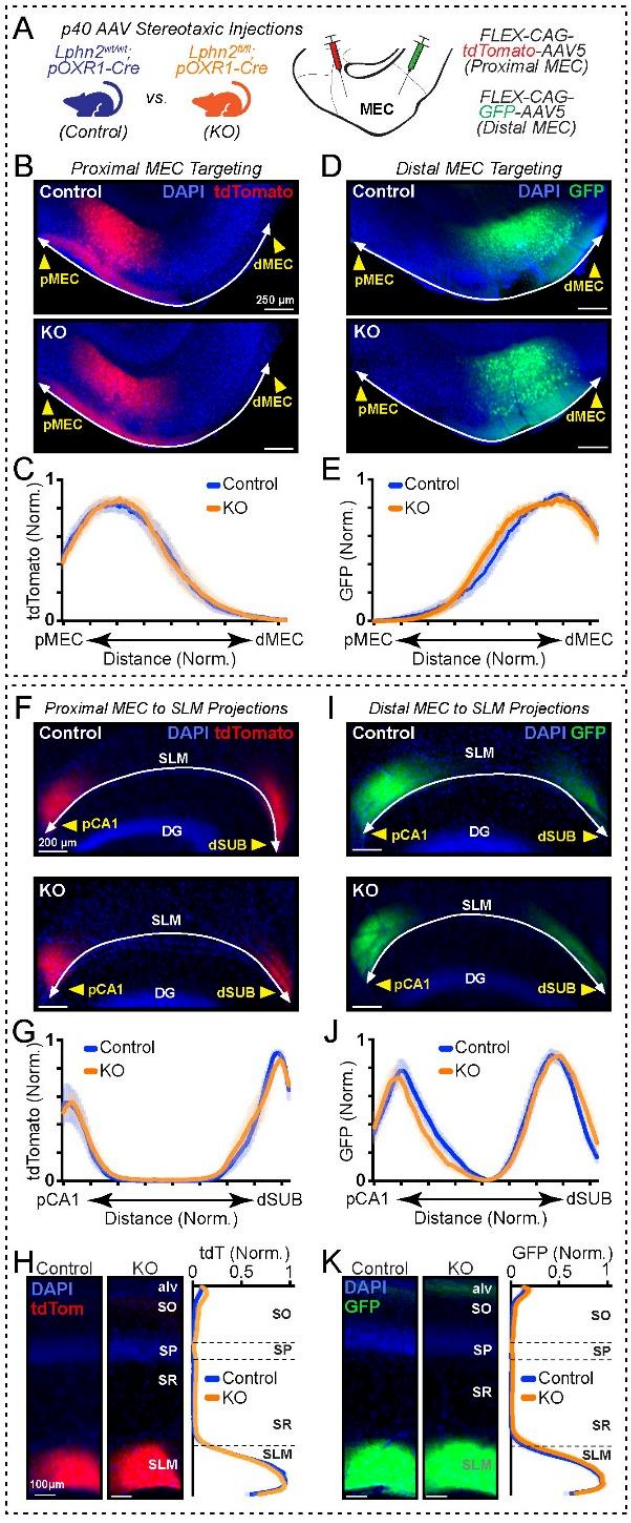

Figure 2. Lphn2 deletion in MEC layer III neurons does not affect hippocampal projection topology.
(A) Genotype description of mice used for the experiment alongside experimental schematic illustrating viruses used (B) Representative image of tdTomato labelled proximal MEC neurons for control (top) and KO (bottom) mice. (C) Line intensity scan measurement across proximal>distal MEC layer 3 comparing localization of injection for control and KO (n=6 pairs). (D) Representative image of tdTomato labelled proximal MEC axons in the SLM for control (top) and KO (bottom) mice. (E) Line intensity scan measurement across proximal CA1 > distal SUB in the SLM comparing localization of injection for control and KO. (F) (Left) Representative image of control and KO tdTomato labelled Axons in the SLM illustrating layer specific targeting. (Right) Line intensity scan measurement across CA1 layers comparing layer specific targeting of tdTomato axons for control and KO. (G) Representative image of GFP labelled distal MEC neurons for control (top) and KO (bottom) mice. (H) Line intensity scan measurement across proximal>distal MEC layer 3 comparing localization of injection for control and KO (n=6 pairs). (I) Representative image of GFP labelled distal MEC axons in the SLM for control (top) and KO (bottom) mice. (J) Line intensity scan measurement across proximal CA1 > distal SUB in the SLM comparing localization of injection for control and KO. (K) (Left) Representative image of control and KO GFP labelled Axons in the SLM illustrating layer specific targeting. (Right) Line intensity scan measurement across CA1 layers comparing layer specific targeting of GFP axons for control and KO.

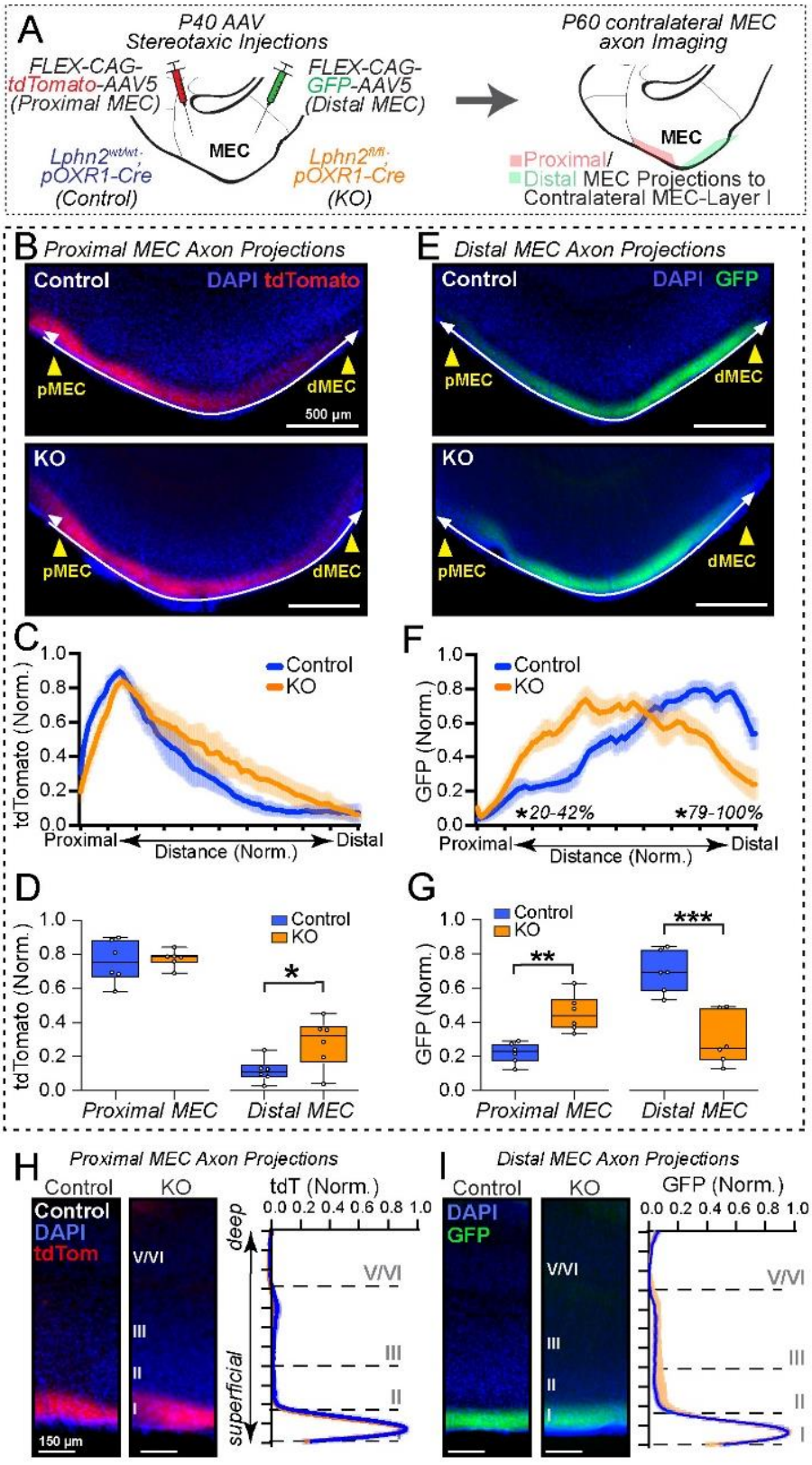
A
P40 AAV
Stereotaxic Injections
FLEX-CAG-
tdTomato-AAV5
(Proximal MEC)
FLEX-CAG-
GFP-AAV5
(Distal MEC)
MEC
Lphn2wt/wt;
pOXR1-Cre
(Control)
Lphn2fl/fl;
pOXR1-Cre
(KO)
P60 contralateral MEC
axon Imaging
MEC
Proximal/
Distal MEC Projections to
Contralateral MEC-Layer I
B Proximal MEC Axon Projections
Control
DAPI tdTomato
pMEC
dMEC
500 µm
KO
pMEC
dMEC
E Distal MEC Axon Projections
Control
DAPI GFP
pMEC
dMEC
KO
pMEC
dMEC
C
tdTomato (Norm.)
Control
KO
Proximal
Distance (Norm.)
Distal
F
GFP (Norm.)
Control
KO
*20-42%
*79-100%
Proximal
Distance (Norm.)
Distal
D
tdTomato (Norm.)
Control
KO
*
Proximal MEC
Distal MEC
G
GFP (Norm.)
Control
KO
**
***
Proximal MEC
Distal MEC
H
Proximal MEC Axon Projections
Control
KO
tdT (Norm.)
Control
DAPI
tdTom
V/VI
III
II
I
150 µm
deep
superficial
I
Distal MEC Axon Projections
Control
KO
GFP (Norm.)
DAPI
GFP
V/VI
III
II
I

Figure 3. Lphn2 deletion from MEC layer III neurons alters contralateral MEC input topology

(A) Genotype description of mice used for the experiment alongside experimental schematic illustrating viruses used (B) Representative image of tdTomato labelled proximal MEC axons in contralateral MEC for control (top) and KO (bottom) mice. (C) Line intensity scan measurement across proximal>distal MEC layer 1 comparing axon localization between control and KO (n=6). (D) Average fluorescence levels compared between control and KO between 0-50% (proximal) and 51-100% (distal). (E) Representative image of GFP labelled proximal MEC axons in contralateral MEC for control (top) and KO (bottom) mice. (F) Line intensity scan measurement across proximal>distal MEC layer 1 comparing axon localization between control and KO (n=6). (G) Average fluorescence levels compared between control and KO between 0-50% (proximal) and 51-100% (distal). (H) (Left) Representative image of control and KO tdTomato labelled Axons in the MEC layer I, illustrating layer specific targeting. (Right) Line intensity scan measurement across MEC layers comparing layer specific targeting of tdTomato axons for control and KO. (I) (Left) Representative image of control and KO GFP labelled Axons in the MEC layer I, illustrating layer specific targeting. (Right) Line intensity scan measurement across MEC layers comparing layer specific targeting of GFP axons for control and KO. Statistical analyses for E were conducted using multiple student's t-test's comparing fluorescent intensity divided into 100 equal units with multiple comparisons corrected using Holm-Sidak method (*$p < 0.05$). Statistical analyses for F were conducted using multiple student's t-test's comparing proximal or distal compartments across groups (**$p<0.01$, **$p<0.001$).

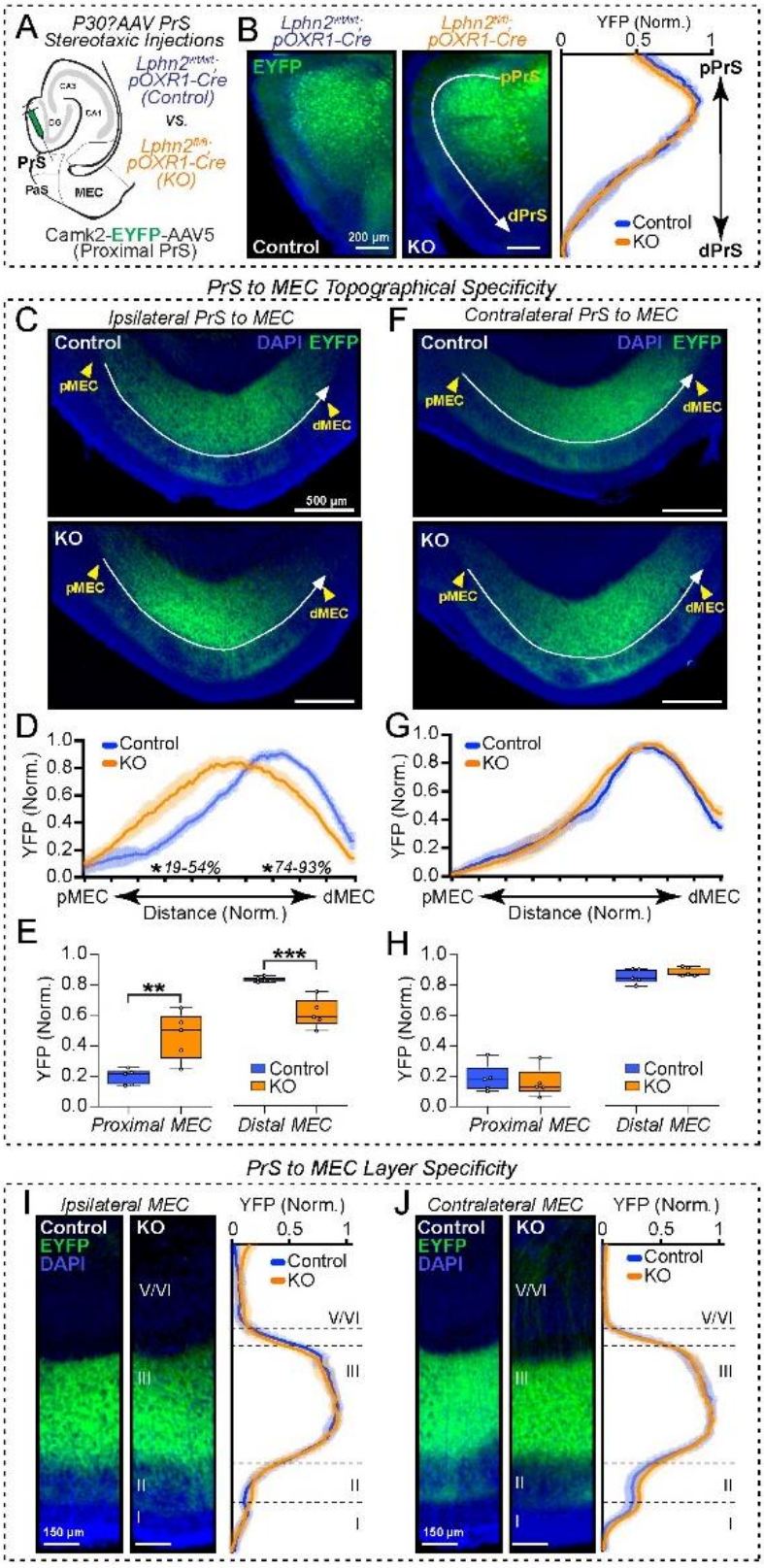
A
P30?AAV PrS Stereotaxic Injections
Lphn2 pOXR1-Cre (Control)
vs.
Lphn2 pOXR1-Cre (KO)
Camk2-EYFP-AAV5 (Proximal PrS)
PrS
PaS
MEC
B
Control
KO
EYFP
pPrS
dPrS
200 µm
YFP (Norm.)
Control
KO
PrS to MEC Topographical Specificity
C
Ipsilateral PrS to MEC
F
Contralateral PrS to MEC
DAPI EYFP
pMEC
dMEC
500 µm
D
G
YFP (Norm.)
*19-54%
*74-93%
Distance (Norm.)
E
H
**
***
Proximal MEC
Distal MEC
PrS to MEC Layer Specificity
I
Ipsilateral MEC
J
Contralateral MEC
EYFP
DAPI
V/VI
III
II
I
150 µm

Figure 4. Lphn2 deletion from MEC layer III neurons alters pre-subiculum input topology.
(A) AAV experimental schematic targeting MEC using CamK2-YFP-AAV5 to label proximal presubiculum neurons. (B) (Left) Representative image of YFP labelled proximal PrS neurons for control and KO mice. (Right) Line intensity scan measurement across proximal>distal PrS layer 3 comparing localization of injection for control and KO (n=5). (C) Representative image of YFP labelled PrS axons in ipsilateral MEC for control (top) and KO (bottom) mice. (D) Line intensity scan measurement across proximal>distal MEC layer III comparing axon localization between control and KO (n=5). (E) Average fluorescence levels compared between control and KO between 0-50% (proximal) and 51-100% (distal). (F) Representative image of YFP labelled PrS axons in contralateral MEC for control (top) and KO (bottom) mice. (G) Line intensity scan measurement across proximal>distal MEC layer III comparing axon localization between control and KO (n=6). (H) Average fluorescence levels compared between control and KO between 0-50% (proximal) and 51-100% (distal). (I) (Left) Representative image of control and KO YFP labelled Axons in the MEC layer III, illustrating layer specific targeting. (Right) Line intensity scan measurement across MEC layers comparing layer specific targeting of YFP axons for control and KO. (J) (Left) Representative image of control and KO YFP labelled Axons in the MEC layer III, illustrating layer specific targeting. (Right) Line intensity scan measurement across MEC layers comparing layer specific targeting of YFP axons for control and KO. Statistical analyses for D were conducted using multiple student's t-test's comparing fluorescent intensity divided into 100 equal units with multiple comparisons corrected using Holm-Sidak method (*$p < 0.05$). Statistical analyses for E were conducted using multiple student's t-test's comparing proximal or distal compartments across groups (**$p<0.01$, **$p<0.001$).

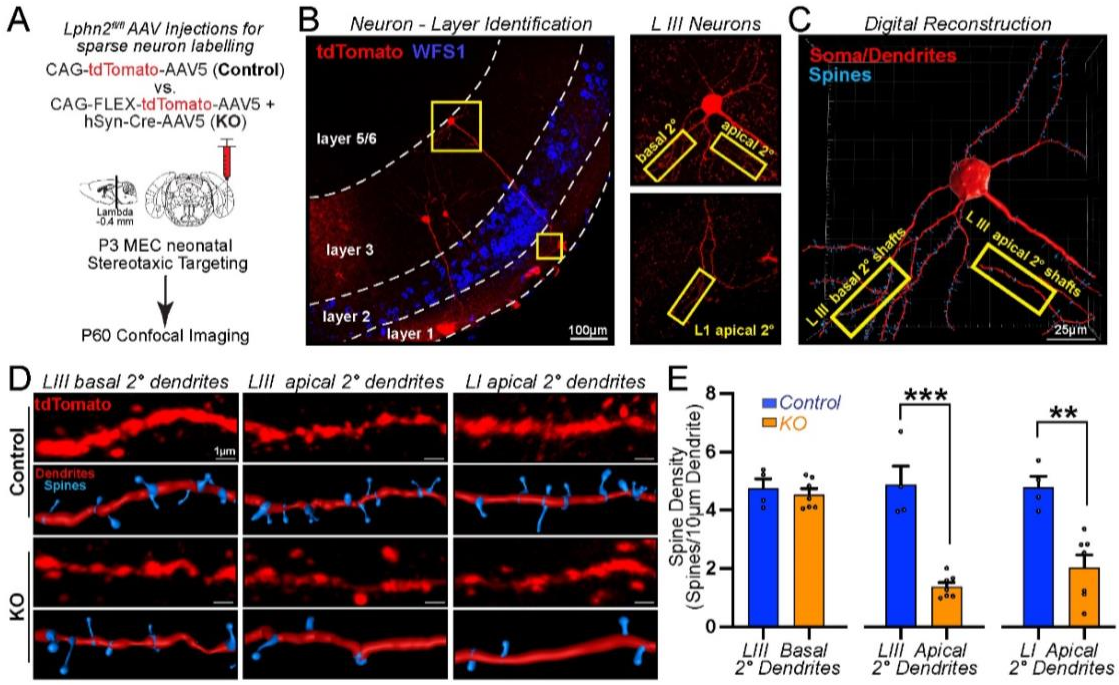

Figure 5. Lphn2 Deletion in MEC layer III neurons decrease spine density of secondary apical shafts

A) AAV viral experimental schematic. MEC was stereotactically targeted in P3 mice with AAVs expressing tdTomato (control) versus a cocktail of hSyn-Cre + FLEX-tdTomato expressing AAVs (Lphn2-KO) to achieve sparsely tdTomato-labeled neurons for visualization. Neurons in the distal MEC were confocal imaged after maturation (P60). (B) Representative confocal image of sparsely labeled superficial MEC neurons in deep layer III and superficial layer III. (C) (Left) Zoomed in confocal z-stack images of superficial and deep layer III neurons and their primary apical shafts in MEC layer I. (Right) representative reconstruction of pyramidal neuron with dendrites (red) analyzed for spine (blue) protrusions. (D) Representative confocal images and digital reconstructions of dendrites (red) and spines (blue) of layer III MEC pyramidal neurons from control (top) and Lphn2-KO neurons (bottom). Shown are basal dendrites (left), deep L III secondary apical dendrites (middle), and superficial L I secondary apical dendrites (right). (E) Summary graphs of spine densities in defined dendritic compartments of pyramidal neurons (control = 4 neurons, Lphn2-KO = 7 neurons; five littermate paired animals). Statistical analyses were conducted using student's t-test.

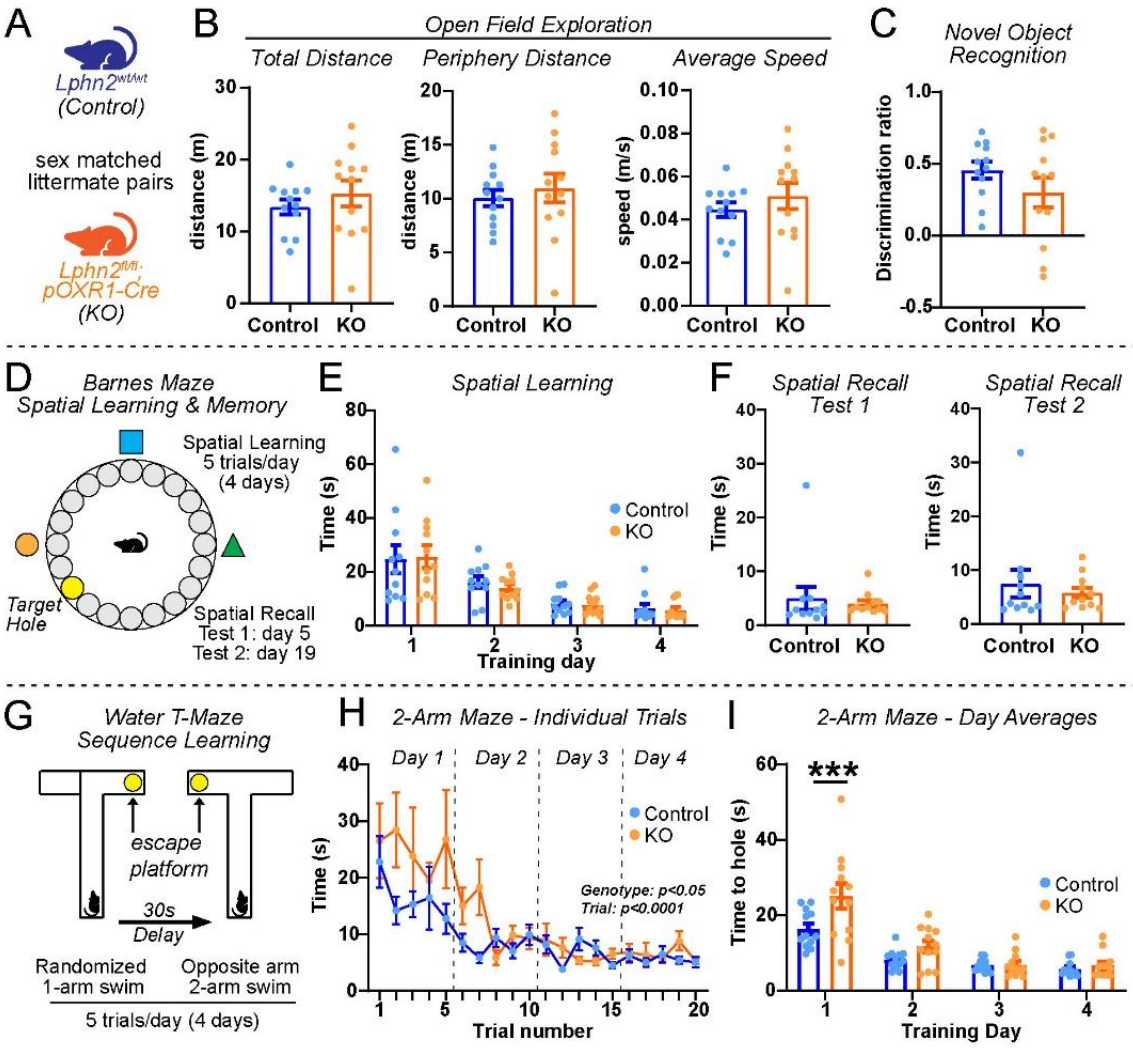

Figure 6. Lphn2 Deletion from MEC layer III neurons causes deficits in reversal spatial learning.

(A) Experimental schematic illustrating genotype description of mice used for behavior experiments (B) Summary Graphs illustrating results of the open field test (n=12 matched pairs). (Left) total distance traversed during the open field task, (middle) distance traversed in the periphery of the open field, (right) average speed across the open field task. (C) Summary graph of the novel object task. Discrimination ratio: $\frac{time\ interacting\ with\ novel\ obect - time\ interacting\ with\ familiar\ object}{time\ interacting\ with\ novel\ obect + time\ interacting\ with\ familiar\ object}$. (n=12) (D) Experimental schematic for the Barnes Maze. Mice were trained 5 times a day for 4 days with Test 1 the following day after training and Test 2 is 14 days after the final training. (E) Summary bar graphs of average time spent to find the target hole across trials for each day (n=11) (F) Time spent to find target hole on Test 1 (left) and Test 2 (right). (G) Experimental schematic of the alternating water T-maze cognitive flexibility task, mice were trained 5 trial pairs/day for 4 days and given 30s between individual trials. (H) Summary plots of time to platform during test trials (n=12) statistical analyses were conducted using multiple student's t-test's with multiple comparisons corrected using Holm-Sidak method, (*p < 0.05). (I) Summary graphs of average time to platform per day during test trials (n=12) statistical analyses were conducted using multiple student's t-test's with multiple comparisons corrected using Holm-Sidak method.

STAR Methods.

Key Resource Table.

REAGENT or RESOURCE	SOURCE	IDENTIFIER
Antibodies		
Mouse monoclonal anti-NeuN	Millipore	MAB377
Rabbit polyclonal anti-GFP	Invitrogen	A-11122
Rabbit polyclonal anti-Wfs1	Proteintech	26995-1-AP
Goat anti-rabbit Alexa 405	Thermo Fisher Scientific	A31556
Goat anti-rabbit Alexa 488+	Thermo Fisher Scientific	A32731
Goat anti-mouse Alexa 555+	Thermo Fisher Scientific	A32427
Bacterial and virus strains		
CAG-FLEX-tdTomato-AAV5	Nor.Carolina vector core	28306
CAG-FLEX-GFP-AAV5	Nor.Carolina vector core	28304
Camk2-EYFP-AAVrg	Nor.Carolina vector core	26969-AAV5
hSyn-CRE-AAV5	Addgene	105553-AAV5
smFISH probes		
Mm-Lphn2-C1	ACDBio	319341
Mm-Tenm3-C1	ACDBio	411951
smFISH fluorophores		
Opal 540	Akoya Biosciences	FP1494001KT
Transgenic mice lines		
Lphn2-mVenus^{cKO}	Anderson et al. 2017	JAX: 023401

Lphn2^{cKO}	Anderson et al. 2017	JAX: 023401
Oxr1^{CRE}	Suh et al. 2011	JAX: 030484
Analysis Software and Programs		
ImageJ	NIH	https://imagej.nih.gov/ij/
Imaris	Oxford Instruments	https://imaris.oxinst.com/
Zen Black	Zeiss	https://www.zeiss.com/microscopy/us/products/microscope-software/zen.html
BORIS 7	Friard and Gamba 2016	https://www.boris.unito.it/
Prism 7	Graphpad	https://www.graphpad.com/
Anymaze	Stoelting co	https://www.any-maze.com/
Other		
High Precision Microscopy slides	Thorlabs	MS10UW
HistoBond+M slides	VWR	16004-406
Precision slide covers	Thorlabs	CG15KH1

Resource Availability

Lead Contact

Further information and requests for resources and reagents should be directed to and will be fulfilled by the Lead Contact, G. R. Anderson (garreta@ucr.edu)

Materials availability

This study did not generate new unique reagents

Data and code availability

No datasets were generated during this study. The images used for analysis in this study are available from the lead contact upon request.

Experimental Model and Subject Details.

Transgenic mice: Lphn2-mVenus^{cKO} and Lphn2^{cKO} mice used in this study were described previously (Anderson et al., 2017). Oxr1^{CRE} mice used I this study were described previously (Suh et al, 2011). The original mouse lines (Lphn2^{KI+neo} allele, Oxr1^{CRE}) used for generation of these lines are available through Jackson Laboratory Mouse Repository for distribution. Lphn2-mVenus$^{FL/FL}$; Oxr1^{CRE+} mice were compared with Lphn2-mVenus$^{FL/FL}$: Oxr1^{WT} mice to validate CRE expression in MEC layer III neurons and measure differences in protein levels (figure 1C). Lphn2$^{FL/FL}$; Oxr1^{CRE+} mice were compared with Lphn2$^{FL/FL}$; Oxr1^{WT} mice in axon topology experiments testing proximal and distal MEC, alongside PrS axon projection topology (figure 1F - Figure 4). Lphn2$^{FL/FL}$; Oxr1^{CRE+} mice were compared with Lphn2$^{FL/FL}$; Oxr1^{WT} littermate pairs in behavioral experiments (figure 6A). Mice were weaned at 21 days of age and housed in groups of 2 to 5 on a 12-hour light/dark cycle with food and water ad libitum in the University of California, Riverside Animal Housing Facility. All procedures conformed to National Institutes of Health Guidelines for the Care and Use of Laboratory Mice and were approved by the University of California, Riverside Administrative Panel on Laboratory Animal Care, and Administrative Panel of Biosafety. Male and female mice were used for all experiments in sex-matched littermate pairs, no differences were noted due to sex.

Method Details.

Stereotaxic Viral Targeting.

For adult mice (P35), surgeries were performed with isoflurane anesthesia. Neonatal mice (P3) surgeries were performed with 5-minute ice anesthesia. Using a dual manipulator stereotaxic frame (Kopf), stereotaxic coordinates used were: Anterior/Posterior (AP) in relation to Lambda; Medial/Lateral (ML) in relation to midline; and Dorsal-Ventral (DV) in relation to dorsal brain surface. Coordinates used: Adult Proximal MEC targeting (Fig. 1F). Proximal MEC: AP +0.6 mm, ML: +3.2 mm, DV −2.2 mm. Adult Distal MEC targeting (Fig. 1F): AP +0.8 mm, ML +3.8 mm, DV −2.4 mm. Adult Proximal PrS targeting (Fig 4a): AP +0.15 mm, ML +2.4 mm, DV −1.8 mm. Neonatal P3 MEC targeting (Figure 5A): AP +0.2 mm; ML +2.1 mm; and DV −2.0 mm. Concentrated adeno-associated viruses (AAVs) were injected (0.2-0.25 µl) with a glass micropipette tip using a controlled rate (0.15 µl/min) with an infusion pump (Harvard Apparatus).

Immunohistochemistry (IHC).

Mice were anesthetized and perfused transcardially with 20 mL PBS and 10 mL freshly prepared 4% PFA. Brains were dissected and postfixed in 4% PFA overnight at 4°C. Brains were briefly rinsed in PBS, mounted in agarose and 100-µm horizontal serial sections were collected using a Vibratome VT100S (Leica Biosystems). For immunofluorescence staining, sections were then washed in PBS for 5 min under gentle agitation followed by incubation for 1 hour in a blocking solution containing 10% goat serum and 0.5% Triton X-100 in PBS. Subsequently, sections were transferred into PBS containing 1% goat serum, 0.01% Triton X-100, primary antibody, and incubated overnight (16-20 hours) at 4°C on a nutating mixer. Sections were washed three times with PBS for

5 min each, then incubated in a solution of 1% goat serum, 0.01% Triton X-100, and secondary antibodies for 4 hours at 4°C on a nutating mixer. Finally, sections were washed three times in PBS for 5 min each and mounted on microscope slides using Vectashield Plus Antifade mounting media.

Axon topology fluorescent imaging.

For each brain, horizontal sections 100 µm thick were prepared as above, and 6-7 sections (spanning 1.4 mm to 3.6 mm ventral to bregma) were stained for Alexa-405 (Ws1). Sections were selected that had the highest signal intensity for the injection site and axonal projection targets for later analysis. Sections were imaged using a Zeiss Axio Imager M2 fluorescence microscope and 2.5x air lens. Acquisition settings were optimized and held constant for each imaged hemisphere of a single brain (ipsilateral and contralateral to infection). Images from P60 animals had regional boundaries added using Wfs1 staining and the rhinal fissure (Figure 1G). Fluorescence intensity was subsequently analyzed in ImageJ software using a line intensity analysis.

Single molecule RNA fluorescent in-situ hybridization (smFISH).

P30 wild type mice were anesthetized with isoflurane and transcardially perfused with 20 mL ice-cold 0.1% DEPC treated and autoclaved PBS, followed by 10 mL 0.1% DEPC treated and autoclaved PFA. Brains were placed into a sterile solution of 4% PFA for 24 hours, followed by 10% sucrose overnight at 4º C. Brains were subsequently cryoprotected by stepwise immersion in sterile 10%, 20% and 30% sucrose, remaining in each solution until no longer floating. After 2-3 days in sucrose, brains were mounted on a drop of cryoprotectant and stored at -80º C until cryosectioning. Brains were cryo-

sectioned at 15 µm thickness and adhered to HistoBond+M adhesive microscope slides. After sectioning, tissue *in situ* hybridization was performed using RNAscope Multiplex Fluorescent RNA probes. Tissue was mounted using Vectashield Plus Antifade mounting media with DAPI and Precision Cover Glass Slips. For single molecule *in-situ* hybridization, probes used were: Latrophilin-2, Tenm3. Akoya fluorophores used for hybridization include Opal 540 (C1 channel [Lphn2], [Tenm3]). Imaging was performed on a Zeiss 880 confocal microscope with airyscan using a Plan Apochromat 10x/0.45 M27 air objective scanning in airy fast "Flex" mode (0.7x Nyquist) at 2.17 µs/pixel. DAPI was captured using a 405 nm laser and BP 420-480 + BP 495-550 emission filter with BP 420-460 + LP 500 secondary beam splitter. Lphn2/Tenm3 probes hybridized to Opal 540 and captured using a 488 nm laser with BP 420-480 + BP 495-550 emission filter and LP 525 secondary beam splitter.

Sparse fluorescent labeled neuron confocal imaging.

Five female pairs of mice were injected neonatally with MEC-targeted viruses, each pair consisting of one Lphn2 knockout and one control, and perfused/sectioned at P30 as described above. Prior to staining, to confirm accurate MEC targeting and adequate tdTomato infectivity, sections were briefly examined under a fluorescent microscope. Six sections (2.4 to 3.1 mm ventral to bregma) from each animal were selected, immunostained for Lphn2 and viewed under fluorescence. From these sections, 3 per animal were chosen for high-power imaging, with littermate sections matched based on similar peak MEC Lphn2 signal. Confocal imaging was performed on these sections with a Zeiss 880 microscope with airyscan in airy fast "optimal" mode, using a 561 nm laser with BP 570-620 + LP 645 emission filter and SP 615 secondary beam splitter. To

determine which neurons might be suitable for imaging, an initial reference image of the MEC was captured using a Plan Apochromat 10x/0.45 M27 air objective at 0.5x digital zoom. Neurons along the distal edge of the MEC (where Lphn2 signal is strongest) were subsequently chosen for high-power imaging, using a Plan Apochromat 40x oil objective at 1-1.5x digital zoom and 2.35 µs/pixel scan speed, with laser intensity/gain optimized and held constant within each matched pair of mice. Z-stacks starting >5 µm into the tissue and extending 30-40 µm deep (0.185 µm slice interval) were acquired to capture neurons and their local processes, with each stack focused around 1-2 neuronal cell bodies to ensure a high likelihood of imaging many complex dendrites. Layer II/III boundary neurons were defined as any neurons whose soma were within one imaging frame (approx. 300 µm, or 5-6 cell bodies) of layer I. Layer III neurons were defined as being deep in the highly enriched Lphn2 zone, whereas layer V neurons were directly adjacent to the peak Lphn2 enrichment zone at the layer III/IV transition.

Open Field basal locomotor activity.

P60-P90 mice were tested for differences in basal locomotor activity for 5 minutes in a 60 cm x 30 cm arena. Mice were placed in the center of the arena and allowed to freely explore for the duration while being recorded by an overhead camera. The mice were then removed and placed back in their home cage.

Novel Object Recognition task.

Mice were tested for recognition memory by placing them in a 60 cm x 30 cm arena with 2 identical objects in opposite corners of the arena (5 cm away from each wall). They are allowed to freely roam for 5 minutes and are record for later analysis. They are then

removed and placed back in their home cage for 1 hour. One of the objects is switched for a novel object and the mice are given another 5-minute trial (the position of the switched object is alternates each trial to account for any place preference). The mice are then removed from the cage and placed in their home cage.

Barnes Maze spatial memory task.

Mice were tested for spatial learning using a modified version of a Barnes maze protocol (Anderson, 2017). The mice are placed on a circular brightly lit platform (92 cm diameter) with 20 holes (diameter 5 cm) equally spaced around the periphery. Only one of the holes has an escape box (7 cm deep, 7 cm wide, 10cm long), where the other holes have false escape holes placed made of the same texture as the table. Visual cues were present around the outside of the maze to serve as reference to the position of the escape hole. Mice were placed in the center of the maze in a holding chamber for 10 seconds and then lifted so the mice can freely explore. They are assayed for their ability to spatially navigate the maze to the target hole, which they are naturally inclined to seek and avoid the brightly lit open arena. The mice are first given trials where they are guided to the hole until they willingly go in before 120 seconds have elapsed. They are trained on four consecutive days with five trials a day (20 trials). Mice are tested 1 day after training and 14 days after for latency to interact with the target hole during a single trial for both tests.

Water T-maze cognitive flexibility test.

The maze consists of a start zone: (30 cm length, 10 cm width) and an upper perpendicular zone: (70 cm length, 10 cm width) was constructed with black plastic and filled with 8 cm of water. A randomized T-maze arm was blocked off and a black escape

platform was placed on the end of the open arm. Mice were placed in the beginning of the start zone time was recorded to reach the escape platform, where they were placed in a dry holding chamber for 30 seconds while the other arm was opened in maze and the escape platform switched to the other side. Mice were then placed at the start to complete the second forced swim test, until they reached the second platform which concluded the second trial.

Quantification and Statistical Analysis.

Axon Topology.

Axon topology images were imported into ImageJ for analysis using 25-(layer I projections),100- (SLM projections) or 200-pixel (PrS/MEC layer III injection targeting) wide line ROIs. These ROIs traversed the proximal to distal axis across the middle of a given region/layer guided by Wfs1 staining to determine unclear regional boundaries. In the MEC, layers were defined as follows; layer I: begins in the end of tissue to where Wfs1 staining is observed. Layer II: rich with Wfs1 staining. Layer III: between the gap of cells which indicates layer IV in the MEC and Wfs1 staining in layer II. Measurements were normalized from 0-100% intensity by subtracting the minimum intensity and dividing by the maximum intensity to give a relative fluorescence value for each projection.

Neuron reconstructions.

Neuron reconstructions by double blinded undergraduates were completed in a similar fashion as (Donohue et al. 2021) with an emphasis on capturing the distal shafts of the neuron instead of the local ones. Using images of individual neurons and their dendrites in different layers, the soma residing in either deep or superficial layer III were

reconstructed first. Axons, dendrites and spines were then reconstructed semi-automatically using the filament creation wizard and “autopath” tool. Basal and Apical shafts were reconstructed, with a focus on the distal secondary shafts in deep layer III or superficial layer I of distal MEC where Lphn2 protein is most abundant (Donohue et al. 2021). Spine density was calculated by dividing number of spines by length of dendrite and compared across groups.

Open Field test.

Videos were analyzed for the first 5 minutes of recording after holding chamber was lifted using automated software (anymaze). Mice were compared for total distance moved, average speed and distance moved in the perimeter. To calculate perimeter distance, the arena was divided into 4 x 8 equal quadrants and automated software compared each given variable for the perimeter and middle compartments.

Novel Object Recognition.

Using Boris (Friard and Gamba 2016), two double blinded undergraduate students recorded time spent investigating either the familiar or novel object across the 5-minute test trial. To calculate the discrimination ratio used to compare preference, time spent with the familiar object is subtracted from time spent with the novel object, which is divided by time spent with both. This results in a number -1 to 1 which reflects time spent with either the novel or familiar object.

Barnes maze.

Using Boris, two double blinded undergraduate students recorded the latency for mice to reach the target hole and interact with it. Researchers recorded the time in which the mouse was released from their holding container, alongside the time in which the mouse first interacted (usually by sniffing) the target hole to determine the time it took the mouse to find the hole. Data was compared to confirm there were no large outliers, and scores were then averaged together for statistical analysis.

Water T-maze.

Using Boris, two double blinded undergraduate students recorded the latency for mice to reach the target platform. Researchers recorded the time in which the mouse touched the water, and the time in which they started to get on top of the target platform to determine the time it took the mouse to swim to the correct platform. Data was compared to confirm there were no large outliers, and scores were then averaged together.

Quantification and Statistical Analysis.

All statistical analysis was performed using Prism 7 software (GraphPad). Data are shown as mean ± SEM. Significance testing was performed using either one-way ANOVA with post-hoc tukey test for multiple comparisons, or via two-tailed Student's t-test, as appropriate. Statistically significant differences are indicated by asterisks (*$p<0.05$; **$p<0.01$; ***$p<0.001$). All relevant data presented in this study is available from the authors upon request.

Chapter 3 References

Anderson, Garret R., Stephan Maxeiner, Richard Sando, Theodoros Tsetsenis, Robert C. Malenka, and Thomas C. Südhof. 2017. “Postsynaptic Adhesion GPCR Latrophilin-2 Mediates Target Recognition in Entorhinal-Hippocampal Synapse Assembly.” *Journal of Cell Biology* 216 (11): 3831–46. https://doi.org/10.1083/jcb.201703042.

Arcos-Burgos, M., M. Jain, M. T. Acosta, S. Shively, H. Stanescu, D. Wallis, S. Domené, et al. 2010. “A Common Variant of the Latrophilin 3 Gene, LPHN3, Confers Susceptibility to ADHD and Predicts Effectiveness of Stimulant Medication.” *Molecular Psychiatry* 15 (11): 1053–66. https://doi.org/10.1038/mp.2010.6.

Beer, Zachery, Peter Vavra, Erika Atucha, Katja Rentzing, Hans Jochen Heinze, and Magdalena M. Sauvage. 2018. “The Memory for Time and Space Differentially Engages the Proximal and Distal Parts of the Hippocampal Subfields CA1 and CA3.” *PLoS Biology* 16 (8): 1–21. https://doi.org/10.1371/journal.pbio.2006100.

Berns, Dominic S., Laura A. DeNardo, Daniel T. Pederick, and Liqun Luo. 2018. “Teneurin-3 Controls Topographic Circuit Assembly in the Hippocampus.” *Nature* 554 (7692): 328–33. https://doi.org/10.1038/nature25463.

Burbach, Peter P.H., and Dimphna H. Meijer. 2019. “Latrophilin’s Social Protein Network.” *Frontiers in Neuroscience* 13 (JUN): 1–13. https://doi.org/10.3389/fnins.2019.00643.

Caballero-Bleda, Maria, and Menno P. Witter. 1993. “Regional and Laminar Organization of Projections from the Presubiculum and Parasubiculum to the Entorhinal Cortex: An Anterograde Tracing Study in the Rat.” *Journal of Comparative Neurology* 328 (1): 115–29. https://doi.org/10.1002/cne.903280109.

Carpenter, Francis, Daniel Manson, Kate Jeffery, Neil Burgess, and Caswell Barry. 2015. “Grid Cells Form a Global Representation of Connected Environments.” *Current Biology* 25 (9): 1176–82. https://doi.org/10.1016/j.cub.2015.02.037.

Cells, Place, Grid Cells, May-britt Moser, David C Rowland, and Edvard I Moser. 2015. “Place Cells, Grid Cells, and Memory,” 1–16.

Donohue, Jordan D., Ryan F. Amidon, Thomas R. Murphy, Anthony J. Wong, Elizabeth D. Liu, Lisette Saab, Alexander J. King, Haneal Pae, Moyinoluwa T. Ajayi, and Garret R. Anderson. 2021. “Parahippocampal Latrophilin-2 (ADGRL2) Expression Controls Topographical Presubiculum to Entorhinal Cortex Circuit Connectivity.” *Cell Reports* 37 (8). https://doi.org/10.1016/j.celrep.2021.110031.

Evensmoen, H. R., J. Ladstein, T. I. Hansen, J. A. Møller, M. P. Witter, L. Nadel, and A. K. Håberg. 2015. “From Details to Large Scale: The Representation of Environmental Positions Follows a Granularity Gradient along the Human

Hippocampal and Entorhinal Anterior–Posterior Axis." *Hippocampus* 25 (1): 119–35.

Friard, Olivier, and Marco Gamba. 2016. "BORIS: A Free, Versatile Open-Source Event-Logging Software for Video/Audio Coding and Live Observations." *Methods in Ecology and Evolution* 7 (11): 1325–30. https://doi.org/10.1111/2041-210X.12584.

Giocomo, Lisa M., Tor Stensola, Tora Bonnevie, Tiffany Van Cauter, May Britt Moser, and Edvard I. Moser. 2014. "Topography of Head Direction Cells in Medial Entorhinal Cortex." *Current Biology* 24 (3): 252–62. https://doi.org/10.1016/j.cub.2013.12.002.

Jung, Min W., Sidney I. Wiener, and Bruce L. McNaughton. 1994. "Comparison of Spatial Firing Characteristics of Units in Dorsal and Ventral Hippocampus of the Rat." *Journal of Neuroscience* 14 (12): 7347–56. https://doi.org/10.1523/jneurosci.14-12-07347.1994.

Kjelstrup, Kirsten Brun, Trygve Solstad, Vegard Heimly Brun, Torkel Hafting, Stefan Leutgeb, Menno P. Witter, Edvard I. Moser, and May Britt Moser. 2008. "Finite Scale of Spatial Representation in the Hippocampus." *Science* 321 (5885): 140–43. https://doi.org/10.1126/science.1157086.

Kononenko, Natalia L., and Menno P. Witter. 2012. "Presubiculum Layer III Conveys Retrosplenial Input to the Medial Entorhinal Cortex." *Hippocampus* 22 (4): 881–95. https://doi.org/10.1002/hipo.20949.

Leamey, Catherine A., Sam Merlin, Paul Lattouf, Atomu Sawatari, Xiaohong Zhou, Natasha Demel, Kelly A. Glendining, Toshitaka Oohashi, Mriganka Sur, and Reinhard Fässler. 2007. "Ten_m3 Regulates Eye-Specific Patterning in the Mammalian Visual Pathway and Is Required for Binocular Vision." *PLoS Biology* 5 (9): 2077–92. https://doi.org/10.1371/journal.pbio.0050241.

Lee, Heekyung, Douglas GoodSmith, and James J. Knierim. 2020. "Parallel Processing Streams in the Hippocampus." *Current Opinion in Neurobiology* 64: 127–34. https://doi.org/10.1016/j.conb.2020.03.004.

Li, Jingxian, Yuan Xie, Shaleeka Cornelius, Xian Jiang, Richard Sando, Szymon P Kordon, Man Pan, et al. 2020. "Alternative Splicing Controls Teneurin-Latrophilin Interaction and Synapse Specificity by a Shape-Shifting Mechanism." *Nature Communications* 11 (2140). https://doi.org/10.1038/s41467-020-16029-7.

Mercati, O., G. Huguet, A. Danckaert, G. André-Leroux, A. Maruani, M. Bellinzoni, T. Rolland, et al. 2017. "CNTN6 Mutations Are Risk Factors for Abnormal Auditory Sensory Perception in Autism Spectrum Disorders." *Molecular Psychiatry* 22 (4): 625–33. https://doi.org/10.1038/mp.2016.61.

Miraoui, Hichem, Andrew A. Dwyer, Gerasimos P. Sykiotis, Lacey Plummer, Wilson Chung, Bihua Feng, Andrew Beenken, et al. 2013. “Mutations in FGF17, IL17RD, DUSP6, SPRY4, and FLRT3 Are Identified in Individuals with Congenital Hypogonadotropic Hypogonadism.” *American Journal of Human Genetics* 92 (5): 725–43. https://doi.org/10.1016/j.ajhg.2013.04.008.

Montchal, Maria E., Zachariah M. Reagh, and Michael A. Yassa. 2019. “Precise Temporal Memories Are Supported by the Lateral Entorhinal Cortex in Humans.” *Nature Neuroscience* 22 (2): 284–88. https://doi.org/10.1038/s41593-018-0303-1.

Pederick, Daniel T., Jan H. Lui, Ellen C. Gingrich, Chuanyun Xu, Mark J. Wagner, Yuanyuan Liu, Zhigang He, Stephen R. Quake, and Liqun Luo. 2021. “Reciprocal Repulsions Instruct the Precise Assembly of Parallel Hippocampal Networks.” *Science* 372 (6546): 1068–73. https://doi.org/10.1126/science.abg1774.

Pederick, Daniel T, Nicole A Perry-hauser, Huyan Meng, Zhigang He, and Jonathan A Javitch. 2022. “Context-Dependent Requirement of G Protein Coupling for Latrophilin-2 in Target Selection of Hippocampal Axons.” *BioRx*, 1–52.

Robertson, Robert G., Edmund T. Rolls, Pierre Georges-François, and Stefano Panzeri. 1999. “Head Direction Cells in the Primate Pre-Subiculum.” *Hippocampus* 9 (3): 206–19. https://doi.org/10.1002/(SICI)1098-1063(1999)9:3<206::AID-HIPO2>3.0.CO;2-H.

Sando, Richard, Xian Jiang, and Thomas C. Südhof. 2019. “Latrophilin GPCRs Direct Synapse Specificity by Coincident Binding of FLRTs and Teneurins.” *Science* 363 (6429). https://doi.org/10.1126/science.aav7969.

Stensola, Hanne, Tor Stensola, Trygve Solstad, Kristian FrØland, May Britt Moser, and Edvard I. Moser. 2012. “The Entorhinal Grid Map Is Discretized.” *Nature* 492 (7427): 72–78. https://doi.org/10.1038/nature11649.

Suh, Junghyup, Alexander J. Rivest, Toshiaki Nakashiba, Takashi Tominaga, and Susumu Tonegawa. 2011. “Entorhinal Cortex Layer III Input to the Hippocampus Is Crucial for Temporal Association Memory.” *Science* 1415 (2011): 1415–21. https://doi.org/10.1126/science.1210125.

Sur, Mriganka & John L. R. Rubenstein. 2005. “Patterning and Plasticity of the Cerebral Cortex.” *Science* 310 (November): 805–10. https://doi.org/10.1016/B978-008045046-9.02027-1.

Wang, Quanxin, Enquan Gao, and Andreas Burkhalter. 2011. “Gateways of Ventral and Dorsal Streams in Mouse Visual Cortex.” *Journal of Neuroscience* 31 (5): 1905–18. https://doi.org/10.1523/JNEUROSCI.3488-10.2011.

Wilson, David I.G., Rosamund F. Langston, Magdalene I. Schlesiger, Monica Wagner, Sakurako Watanabe, and James A. Ainge. 2013. “Lateral Entorhinal Cortex Is Critical for Novel Object-Context Recognition.” *Hippocampus* 23 (5): 352–66. https://doi.org/10.1002/hipo.22095.

Yuen, Ryan K.C., Bhooma Thiruvahindrapuram, Daniele Merico, Susan Walker, Kristiina Tammimies, Ny Hoang, Christina Chrysler, et al. 2015. “Whole-Genome Sequencing of Quartet Families with Autism Spectrum Disorder.” *Nature Medicine* 21 (2): 185–91. https://doi.org/10.1038/nm.3792.

Zhang, Xuchen, Pei Yi Lin, Kif Liakath-Ali, and Thomas C. Südhof. 2022. “Teneurins Assemble into Presynaptic Nanoclusters That Promote Synapse Formation via Postsynaptic Non-Teneurin Ligands.” *Nature Communications* 13 (1). https://doi.org/10.1038/s41467-022-29751-1.

Chapter 4: Conclusions and future directions

Summary of findings

Across this body of work, we have interrogated the function of Latrophilin-2 in synapse assembly and maintenance of entorhinal neurons. First, we identified regional specificity of Lphn2 protein within the parahippocampal circuit and identified the MEC as a hotspot of protein localization. We then characterized Lphn2 expression across the main neuronal types in the MEC and found that pyramidal neurons in layers 2/3 were enriched for the distal but not proximal compartment of the region. We found that deletion of Lphn2 expression in the MEC causes loss of local protein, and synaptic spines on the secondary apical shafts for deep layer III neurons. We then utilized a dual retrograde labelling approach in which we found that proximal and distal compartments of MEC had distinct topology from their inputs. We then deleted Lphn2 expression from MEC neurons and found fewer labelled cells in the ipsilateral presubiculum, but similar numbers of labelled cells in other regions, suggesting input specific loss of connectivity due to Lphn2 deletion in the MEC. We followed these experiments by creating a transgenic mouse capable of specifically labelling MEC layer III outputs. We used this mouse to show that MEC outputs also are confined to a proximal/distal fashion and that these connections overlap with expression gradients of Lphn2 and another synaptic cell adhesion molecule, Tenm3. Labelling MEC layer III neurons, we found deficits in normal axon targeting for distal MEC neurons into the contralateral MEC layer I, although other outputs of these cells were intact. We found mis-localization of presubiculum axons in a similar manner shifted away from the normal zone of Lphn2 enrichment. To test the functional implications of these synaptic deficits we did behavioral testing where we found deficits in learning of sequential spatial tasks, but other behavioral measures were found to be similar. All together we were

able to robustly show that Lphn2 is intimately involved in assembly of synaptic connections for hippocampal circuitry and the behavior these neurons modulate is specifically affected.

Entorhinal circuitry reviewed highlighting MEC layer III pyramidal neurons

In previous chapters we went over the role of Lphn2 in connectivity of topographically distinct neurons between hippocampal regions. Here, we illustrate our findings in relation to topographically distinct proximal/distal MEC layer III populations of neurons (figure 1). We can see that distal MEC neurons preferentially project to other Lphn2 enriched neuronal populations, whereas proximal populations preferentially project to Tenm3 enriched populations of neurons (figure 1). Through our studies, we have been able to show that Lphn2 modulates connectivity between presubiculum afferents onto MEC neurons, and those inputs of contralateral MEC neurons are affected as well, with distal MEC neurons being more highly altered than proximal MEC projections. This data combined with previous knowledge that Lphn2 deletion in CA1 hippocampal neurons causes deficits in MEC>CA1 projections helps paint the picture in which Lphn2 is crucial for multiple interconnected hippocampal regions and the information they process along those distinct nodes. Although we clearly show Lphn2 is important for proper synapse assembly in MEC layer III neurons, what is the function of these synapses in relation to behavior?

Functional significance of Lphn2 dependent inputs/outputs

As previously discussed, MEC layer III neurons have been implicated in alternating spatial learning paradigms (Suh et al. 2011). We find that Lphn2 deletion in MEC neurons causes deficits in PrS projections to these cells. It is known that information pertinent to

navigation is relayed by these Prs>MEC connections (Kononenko and Witter 2012) which are crucial for head direction information in relation to spatial learning (Tang et al. 2015). It is curious that PrS inputs to MEC are shown to be preferentially modulated by head direction information and in our studies, we find that alternating spatial learning is affected in which mice are required to learn a new direction and utilize head direction information. Together this suggests that head direction information relayed by Prs Inputs to MEC may be controlled by Lphn2 expression in post-synaptic MEC neurons.

Functional gradients in hippocampal circuitry

It is well established that neurons function differently due to their anatomical location within the entorhinal cortex. For instance neurons in the dorsal entorhinal cortex that exhibit grid cell firing patterns have more precisely tuned spatial fields whereas neurons in the ventral portions have more loosely tuned fields (Witter and Moser 2006). Additionally, for MEC layer III neurons it is has been shown that they have firing patterns which correlate to the animals head direction (Giocomo et al. 2014) and that there is more precisely tuned accuracy in dorsal MEC neurons which coincides with high Lphn2 expression zones. When we evaluate this evidence together, it suggests that Lphn2 mediated control of synapse assembly may be involved with head direction information conveyed by PrS inputs. Although this is speculation, it may warrant future investigations. When we look to the hippocampus where neurons have firing patterns which are increased for a given place in their surroundings (known as place cells), we see a similar gradient in which more finely tuned place fields exist in the Lphn2 enriched dorsal hippocampus whereas larger more loosely tuned spatial fields are present in ventral CA1 (Jung, Wiener, and McNaughton 1994). As discussed in chapter 3, there is evidence which suggests that

proximal-distal compartments of CA1 process different aspects of spatial cognition where proximal neurons contain more spatially tuned information and distal neurons are more tuned to temporal information (Beer et al. 2018). Moving forward, we should interrogate the differences between proximal Tenm3 enriched CA1 neurons, intermediate Lphn2 enriched CA1 neurons that receive input from the MEC and distal CA1 Lphn2 enriched neurons that primarily receive input from the lateral entorhinal cortex. Using precisely defined regional boarders and in-vivo imaging together this information will help us understand how we the brain processes multiple streams of information into a single cognitive experience.

Future directions and concluding remarks

Moving forward we must first get a better understanding of connectivity patterns in the brain and if these connectivity gradients correspond with expression gradients in the brain as shown here. Our work has investigated a single protein, and we have discussed some related proteins which possess synaptic cell adhesion properties. There are many other molecules known to have synaptic cell adhesion properties involved with synaptogenesis and synaptic maintenance. Using cell-type specific assays for both connectivity and expression data will help us combine the information relating which cells connect and what genes they express. Armed with this knowledge, we will be able to make hypotheses regarding which molecules may be involved with specific connectivity of discrete circuits. This will help us understand the mechanisms of function for these circuits and will give us invaluable information pertaining to how pathology may arise from mutations in these genes. Although there is a clear path forward for this field of work, there are many unanswered questions including how alternative splicing of these genes

modulates binding affinity between synaptic cell adhesion molecules. I look forward to seeing the next generation of scientists tackle these questions and uncover worthwhile questions yet to be asked.

Main Figures and Title Legends.

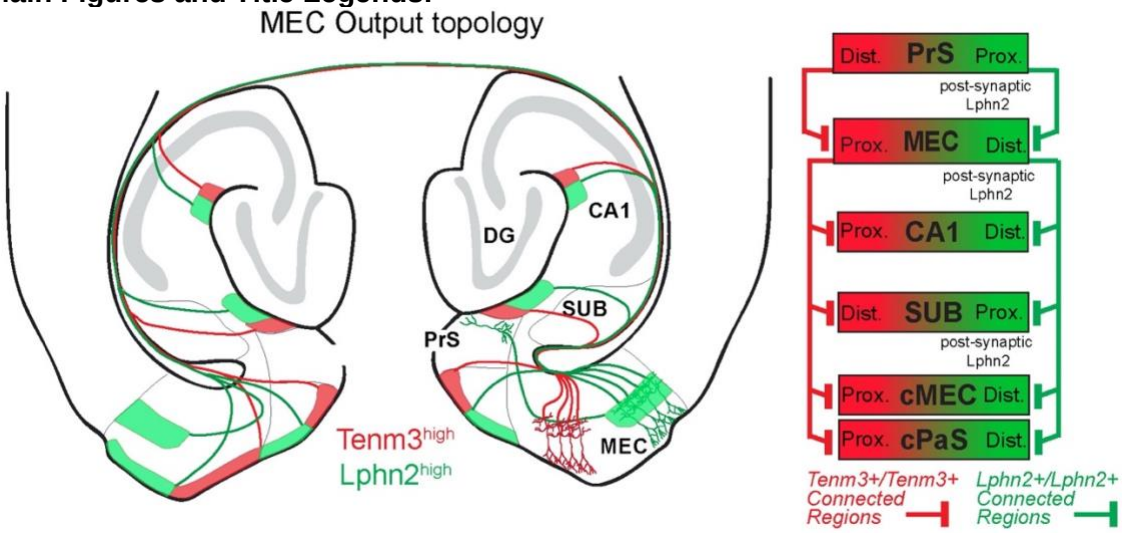

Figure 1. Relevant MEC layer III pyramidal neuron input/output circuitry
(Left) topographical diagram of known input/output projections for MEC layer III neurons shown in previous studies overlapping with expression gradients of Lphn2 & Tenm3. (Right) diagram of specific connectivity illustrating findings on Lphn2 and regions it is implicated in having a post-synaptic role for synapse assembly (PrS>MEC, MEC>CA1, MEC>cMEC).

Chapter 4 references:

Beer, Zachery, Peter Vavra, Erika Atucha, Katja Rentzing, Hans Jochen Heinze, and Magdalena M. Sauvage. 2018. “The Memory for Time and Space Differentially Engages the Proximal and Distal Parts of the Hippocampal Subfields CA1 and CA3.” *PLoS Biology* 16 (8): 1–21. https://doi.org/10.1371/journal.pbio.2006100.

Giocomo, Lisa M., Tor Stensola, Tora Bonnevie, Tiffany Van Cauter, May Britt Moser, and Edvard I. Moser. 2014. “Topography of Head Direction Cells in Medial Entorhinal Cortex.” *Current Biology* 24 (3): 252–62. https://doi.org/10.1016/j.cub.2013.12.002.

Jung, Min W., Sidney I. Wiener, and Bruce L. McNaughton. 1994. “Comparison of Spatial Firing Characteristics of Units in Dorsal and Ventral Hippocampus of the Rat.” *Journal of Neuroscience* 14 (12): 7347–56. https://doi.org/10.1523/jneurosci.14-12-07347.1994.

Kononenko, Natalia L., and Menno P. Witter. 2012. “Presubiculum Layer III Conveys Retrosplenial Input to the Medial Entorhinal Cortex.” *Hippocampus* 22 (4): 881–95. https://doi.org/10.1002/hipo.20949.

Suh, Junghyup, Alexander J. Rivest, Toshiaki Nakashiba, Takashi Tominaga, and Susumu Tonegawa. 2011. “Entorhinal Cortex Layer III Input to the Hippocampus Is Crucial for Temporal Association Memory.” *Science* 1415 (2011): 1415–21. https://doi.org/10.1126/science.1210125.

Tang, Qiusong, Christian Laut Ebbesen, Juan Ignacio Sanguinetti-Scheck, Patricia Preston-Ferrer, Anja Gundlfinger, Jochen Winterer, Prateep Beed, et al. 2015. “Anatomical Organization and Spatiotemporal Firing Patterns of Layer 3 Neurons in the Rat Medial Entorhinal Cortex.” *Journal of Neuroscience* 35 (36): 12346–54. https://doi.org/10.1523/JNEUROSCI.0696-15.2015.

Witter, Menno P., and Edvard I. Moser. 2006. “Spatial Representation and the Architecture of the Entorhinal Cortex.” *Trends in Neurosciences* 29 (12): 671–78. https://doi.org/10.1016/j.tins.2006.10.003.